Dosimetric Characterization of a Directional Low-Dose Rate Brachytherapy Planar Source Array

by

Manik Aima

A dissertation submitted in partial fulfillment of
the requirements for the degree of

Doctor of Philosophy

(Medical Physics)

at the

University of Wisconsin–Madison

2018

Date of final oral examination: 26th July, 2018

This dissertation is approved by the following members of the Final Oral Committee:
Wesley S. Culberson, Assistant Professor, Medical Physics
Larry A. DeWerd, Professor, Medical Physics
Bryan P. Bednarz, Associate Professor, Medical Physics
Douglass L. Henderson, Professor, Engineering Physics
Bruce R. Thomadsen, Professor, Medical Physics

To my parents, Indu and Ashok, ab imo pectore.

Abstract

A variety of low-dose rate (LDR) radioactive sources are used for a number of different cancer treatments. The conventional LDR brachytherapy sources are azimuthally-symmetric. If a directional LDR radioactive source could be used for such procedures, it could potentially lead to an improvement in the therapeutic ratio for these treatments by selectively targeting malignant tissue. The CivaSheet is one such novel device manufactured by CivaTech Oncology Inc. The CivaSheet is a planar array consisting of discrete directional ^{103}Pd elements called CivaDots. A gold shield is present in each CivaDot and imparts directionality to the radiation output of the device. Since the source geometry and design are considerably different than conventional LDR sources, a thorough investigation was required to ascertain the dosimetric characteristics of the device prior to its clinical implementation.

The primary aim of this work was to establish a source strength framework for this directional planar source array as well as determine its dosimetric characteristics. Existing dosimetric formalisms were adapted to accommodate a directional source, and other distinguishing characteristics including the presence of gold shield x-ray fluorescence present in the source energy spectrum were addressed in this work. Primary air-kerma strength measurements were performed, and the source energy spectrum as well as anisotropy distribution were investigated. The feasibility of transferring the primary measurement to a well-type ionization chamber for clinical use was also assessed. Various Monte Carlo simulations of the source were performed. Analogous TG-43 dosimetric parameters for the CivaDot were determined using dose distribution measurements and Monte Carlo methods.

The dose distribution of a CivaSheet was investigated and the impact of a curvature of the CivaSheet on the source dose distribution was also evaluated.

Up to this point, there were no traceable standards for a directional source. This work assisted in the establishment of a primary source strength standard for the directional CivaDot source in collaboration with the National Institute of Standards and Technology (NIST). Clinical physicists are not able to perform treatment planning tasks without appropriate measurements and associated dosimetric data provided in the literature. This work sought to add knowledge to the dosimetry of directional and planar low-dose rate brachytherapy source arrays and ultimately enable clinical physicists to verify their source strength with NIST-traceable calibrations, and look up the relevant dosimetric data in the literature. The investigations performed in this work have facilitated the ongoing clinical implementation of the CivaSheet device and represent a noteworthy advancement in the science of brachytherapy physics.

Acknowledgments

I am reminded of the African proverb – "It takes a village..." when I reflect upon my six-year long graduate school journey at the University of Wisconsin – Madison. It has been a profound experience from both a personal as well as a professional standpoint. This thesis work performed at the University of Wisconsin Medical Radiation Research Center (UWMRRC), is the culmination of about five years of research. The work was facilitated by the support and collaboration of various colleagues, guidance and teaching from the faculty, and encouragement from friends as well as family.

I would first like to thank my advisor, Professor Wesley Culberson, for giving me the opportunity to pursue doctoral research work under his supervision. He has been a great source of support and guidance involving all aspects of this work. His technical knowledge and clinical expertise have supplemented this body of work tremendously. Thank you to Professor Larry DeWerd for giving me the opportunity to perform research work at the UWMRRC. He has been a very kind and supportive mentor throughout the duration of this work. Drs. DeWerd and Culberson have tirelessly provided valuable scientific critique to my various manuscripts, abstracts and presentations over the years. The "Cal-Lab" is a unique workplace, and it's an institution in itself. The collaborative and supportive nature of the staff and fellow students provide an environment where graduate students can truly thrive. I believe that the lab's research ideology places paramount emphasis on

high-quality metrology, which has helped me grow into a strong and independent researcher. The collegial camaraderie of the Cal-Lab has helped me improve as an individual.

I want to thank my thesis defense committee members for their guidance and feedback regarding my proposed doctoral research. I've learnt a great deal from Professors Douglass Henderson, Bruce Thomadsen, and Bryan Bednarz. I've enjoyed multiple conversations with them over the years, from which I gained a lot of knowledge. I would specially like to thank Dr. Henderson, as he was my first graduate school advisor. My journey at UW-Madison began under his advisement in the Department of Nuclear Engineering and Engineering Physics, where I received my first Master's degree. He introduced me to the field of Medical Physics, about which I had previously known very little. I'm grateful to the Medical Physics faculty at UW-Madison, who all are stalwarts of their respective fields, and from whom I have acquired a lot of knowledge and good professional mannerisms. I would like to thank Dr. Jennifer Smilowitz and Mark Guerts for providing me with the opportunity to gain some clinical experience.

The staff at the UWMRRC are peerless. John Micka has provided invaluable support throughout this doctoral work, especially through his expertise on everything measurements and uncertainty related. As we all know at the Cal-lab, his political correctness is always a riot. Next, I would like to thank Cliff Hammer, who has been a huge contributor to this work. I've learnt a lot from him both personally and professionally. I think there hardly has been a week where we haven't discussed profoundly about a research topic or just life in general. I'm thankful to Keith Kunugi for his help with all administrative matters and general support. I would also like to thank Wendy Kenan for humorous conversations, and help with radiation safety. Thanks to Ben Palmer and Jennifer Hull for their support with everything involving mechanical engineering and design. Jennifer helped me immensely with the curved CivaSheet investigation. I'm grateful to Dan Anderson, Jeff Radtke, Louise DeWerd, Steve Bazan, John Haugen-Wente and Denise Faherty for their support.

Several former graduate students of our lab have helped with different aspects of this research work. First, I would like to thank my initial mentor, Dr. Joshua Reed for all his support and guidance. He is a great researcher, from whom there is always something new to learn. Thank you to Dr. Everardo Flores-Martinez for a plentitude of things. His mentorship, friendship and advice are very valuable to me. He has helped me navigate through multiple stages of graduate student life. I'm also thankful to Drs. Jessica Fagerstrom, Benjamin Rosen, and Samantha Simiele, all of whom were a great source of advice and support. I've enjoyed numerous conversations with them over the years about a variety of topics and scientific research.

Many of my peers at the Medical Physics Department and the lab who were in the same year or younger have been supportive throughout my graduate student life. In particular, I would like to thank Natalie Viscariello and Matthew Scarpelli. Natalie has been a bedrock for all things — personal and professional, and has always been a good outlet to discuss my various research quagmires. We have enjoyed countless sodas and reveled in infinite dairy delights together. I think we would make for great confectionery connoisseurs. Matt has been the ideal roommate, and an impeccable friend. We have navigated much of graduate school together rather smilingly through our sarcastic exchanges. I've always appreciated our long-winded research discussions. I would also like to thank Eric Simiele, Vimal Desai, Sameer Taneja and Jon Hansen for their support and peer-review over the years. Thank you to all my classmates throughout graduate school, both in Nuclear Engineering and Medical Physics. They were all delightful peers.

This work has been partially supported throughout by CivaTech Oncology Inc. with the help of National Institute of Health grants (HHSN261201200052C, 1R44CA210770-01). Drs. Kristy Perez and Jainil Shah have always been very supportive of this work, and have provided very helpful feedback as well as criticism. We have had multiple discussions about the various aspects of the research presented in this work. I would also like to

thank Dr. Michael Mitch for his participation in the NIST WAFAC and UW VAFAC inter-comparison investigation. He is a very supportive collaborator. I'm grateful to the customers of the UWADCL and UWRCL whose calibrations provide additional financial resources for research at the UWMRRC.

My initial experiences at various research laboratories during my undergraduate degree shaped my personality profoundly, and inspired me to pursue a doctoral degree. These experiences inculcated in me a sense of curiosity and love for problem-solving as well as research. To that end, I'm especially indebted to Drs. Anju Bhasin and Hans Muller, who were just exceptional mentors. A lot of my passion for scientific research stems from my interactions with Dr. Muller, meanwhile Dr. Bhasin has always been an unwavering source of encouragement and support. I have been privileged to work under many other wonderful research mentors, to whom I'm very thankful.

Lastly, I would like to acknowledge the contribution of my family, who have been staunch and dedicated supporters throughout my graduate school career. My mother, Indu and my father, Ashok, are an exceptional source of inspiration and motivation. They inspire me to strive to improve myself every day. The constant support they have provided has been paramount to all my successes. This acknowledgment would be amiss without thanking my grandparents. Their compassion and care during my formative years has had an immense influence on my life as a whole. My sister, Misha, and brother in-law Puneith, have been the backbone on which I have been able to survive graduate school. I'm grateful to them for their selfless love and resolute support which has always been a limitless source of motivation.

Contents

List of Figures

List of Tables

List of Abbreviations

AAPM	American Association of Physicists in Medicine
DRC	Dose-rate constant
LDR	Low-dose rate
MC	Monte Carlo
MCNP6	Monte Carlo N-Particle Radiation Transport Code 6
NIST	National Institute of Standards and Technology
OD	Optical Density
PDD	Percent depth dose
PMMA	Polymethyl Methacrylate
TG-43	American Assoication of Physicists in Medicine Task Group No. 43
TLD	Thermoluminescent dosimeter
UWADCL	University of Wisconsin Accredited Dosimetry Calibration Laboratory
UWMRRC	University of Wisconsin Medical Radiation Research Center
VAFAC	Variable-Aperture Free-Air Chamber
VW	Virtual Water
WAFAC	Wide-Angle Free-Air Chamber

Chapter 1

Introduction

1.1 Overview

Brachytherapy is an advanced radiotherapy modality that includes use of radioactive sources for cancer treatments. For low-dose rate (LDR) brachytherapy, numerous low-energy photon-emitting sources (commonly ^{125}I, ^{103}Pd or ^{131}Cs) have been used for treatment. The authors of the American Association of Physicists in Medicine (AAPM) Task Group No. 43 report (TG-43) and its associated updates (Nath et al. 1995, Rivard et al. 2004; 2007) recommended a formalism to characterize these sources, and described the relevant dosimetric parameters in detail. There have been advances in source geometry and design since the publication of the report (Reed et al. 2014b, Meigooni et al. 2004, Bernard and Vynckier 2005, Wang and Hertel 2005, Lin et al. 2008, Abboud et al. 2010) to improve upon the conformity of the delivered dosimetric distributions, such as the CivaString™, OptiSeed™, RadioCoil™ and SmartSeed™ brachytherapy sources.

A potential improvement in the dose distribution conformity of an LDR brachytherapy device can be realized by adapting the design of the source to provide directional radiation emission. Such a directional source design adaptation could potentially improve the therapeutic ratio for a given brachytherapy treatment when compared to conventional sources, by

selectively targeting diseased tissue and sparing the surrounding healthy structures. Based on this premise, a novel brachytherapy source has been developed by CivaTech Oncology, Inc (Durham, NC) called the CivaSheet^{TM} for potential use in LDR brachytherapy treatments. The CivaSheet is a planar source array consisting of discrete ^{103}Pd source elements called CivaDots. Each CivaDot consists of a polymer capsule with a gold shield present in close proximity to the active source region, imparting directionality to the radiation output of the device, and thus defining a hot and a cold side of the device.

Previous investigations (Lin et al. 2008, Chaswal et al. 2012) reported reduction in dose to normal tissue in breast and prostate cancer treatments when comparing directional to conventional interstitial sources. CivaTech Oncology, has been developing the device and investigating its efficacy for pancreatic, abdomino-pelvic, and colorectal cancer treatments (trials NCT03109041, NCT02843945, NCT02902107) amongst other sites. CivaTech Oncology has been awarded two National Institute of Health grants (HHSN261201200052C, 1R44CA210770-01) for this purpose.

The CivaSheet is unique in design and varies considerably from conventional LDR brachytherapy sources. When a novel source such as the CivaSheet is introduced commercially, a thorough investigation needs to be conducted to ascertain the source strength and the dosimetric characteristics of the source prior to its clinical implementation. For conventional LDR sources, guidelines and dosimetric formalisms have been recommended by the AAPM. (Rivard et al. 2004, Nath et al. 1997, Butler et al. 2008, DeWerd et al. 2006) There is currently no standard protocol for calibration or quality assurance of planar or directional LDR sources. The planar and directional nature of the CivaSheet device renders the direct application of the guidelines and formalisms as inappropriate. In addition to this, the presence of gold material in such close proximity to the active ^{103}Pd region causes the emitted photon energy spectrum to be significantly different than the energy spectra of seeds normally used in LDR brachytherapy treatments.

Thus, research needs to be performed to explore and to develop a clinically viable source strength metric and a dosimetric framework for the CivaSheet. The dose distribution of the directional CivaSheet array and the individual CivaDot sources need to be investigated in great detail. Various challenges such as the x-ray fluorescence from the gold shield and the planar as well as the directional nature of the device need to be addressed.

This work aims to determine a viable source-strength framework for the CivaSheet based on an individual CivaDot, which can be translated to the clinic. This involves establishment of primary source strength measurement methods for the CivaDot using an instrument such as a free-air ionization chamber. Additional investigations are required to determine the source energy spectrum, anisotropy distribution, and associated free-air chamber correction factors. A test of the applicability and robustness of transferring the primary calibration of a directional source to a well-type ionization chamber for potential future clinical use also needs to be performed. Finally, the establishment of a National Institute of Standards and Technology (NIST)-traceable primary standard for the CivaDot is required for the clinical implementation of the methods and results of this work. For this purpose, a collaborative investigation with NIST was performed to assist in the establishment of the CivaDot primary source strength standard. An inter-comparison of the primary air-kerma strength determined using different free-air chambers for multiple CivaDot sources was performed. The repeatability and the reproducibility of the source strength standard for the CivaDot were also assessed.

A formalism to translate the source strength of a single element (CivaDot) to the dose distribution of a CivaSheet (array of CivaDots) has to be established. This involves characterization of the dose-to-water distribution of an individual directional element and small-sized CivaSheets (nine-elements). Dose measurements with detectors such as thermoluminescent dosimeters and radiochromic film were performed in water-equivalent plastic phantoms using new techniques to ascertain CivaDot and CivaSheet dose distributions. Monte

Carlo simulations of the various measurement setups are required for associated dose-to-water correction factors, and also to provide calculated dose distributions as well as a basis for comparison of the measured results.

The current AAPM dosimetric protocols (such as TG-43) need to be adapted to accommodate planar-directional LDR brachytherapy source arrays. The feasibility of dosimetric superposition of CivaDot dose distribution to determine CivaSheet dose distribution should be investigated. The impact of a potential curvature in a CivaSheet clinical implant on the dose distributed needs to be studied to assess treatment planning considerations when implanting this device in a patient.

1.2 Description of upcoming chapters

Chapter 2 provides the pertinent background information for this work. It consists of an overview of the conventional LDR brachytherapy sources and arrays as well as directional LDR sources. The chapter also introduces the CivaSheet device and CivaDot sources. A discussion of the dosimetry and the AAPM Task Group No. 43 formalism (Nath et al. 1995, Rivard et al. 2004; 2007) used for conventional brachytherapy sources is included in this chapter. Limitations of the application of these methods to the CivaSheet-CivaDot dosimetric characterizations are discussed along with some proposed adaptations. An introduction to the source strength determination and dosimetric characterization methods used in this work are provided and the associated project goals are outlined.

The focus of Chapter 3 is the source strength determination of the CivaDot source. This includes the description of the free-air chamber measurements performed with multiple sources (sequentially) to establish a method to ascertain CivaDot air-kerma strength. The Monte Carlo simulations performed to determine correction factors for the measurements are also described. Measured and Monte Carlo calculated CivaDot energy spectrum as well as anisotropy distribution results are also provided in this chapter. The details of

the inter-comparison with NIST Wide-Angle Free-Air Chamber (WAFAC) measurements to assess the reproducibility and repeatability of these investigations are provided. The feasibility of the clinical transfer of the primary air-kerma strength measurements to a well-type ionization chamber are discussed. An investigation of the CivaDot variability was also reported along with some quality control procedures.

The dosimetric characterization of the CivaDot directional source is described in Chapter 4. The chapter outlines the CivaDot dose measurements performed in a custom water-equivalent plastic phantom using TLD microcubes and EBT3 radiochromic film. The details of the Monte Carlo simulations to calculate the CivaDot dose distribution are also provided. A comparison of the measured and calculated dose distribution for multiple CivaDot sources is included in this chapter. Required adaptations to the TG-43 formalism are discussed along with the determination of TG-43 analog dosimetric parameters for the CivaDot source.

Chapter 5 details the work performed for the dosimetric characterization of the CivaSheet array. This chapter includes the description of the water-equivalent plastic phantoms constructed to perform EBT3 film stack measurements of a CivaSheet array consisting of thirty-six CivaDots. The chapter outlines the results of the dose measurements performed for the device and the subsequent comparisons to Monte Carlo simulations of the CivaSheet. The impact of the curvature of a CivaSheet implant was also described comparing the flat CivaSheet configuration to the convex/concave curved CivaSheet configurations. The chapter also details the validity of dosimetric superposition of individual CivaDot dose distributions to calculate the dose distribution of a CivaSheet array.

Chapter 6 provides the conclusions that can be drawn from this body of work. It also outlines some recommendations for future research that can potentially be used in further improvements in the clinical implementation of directional LDR source arrays and their associated dosimetry.

Chapter 2

Background and motivation

2.1 Low-dose rate brachytherapy sources

Brachytherapy is a form of radiation-based cancer treatment that includes the use of devices containing radioactive material to target malignant tumors. The devices are placed in close proximity to the tumor. Based on the dose rate of the radioactive element used in the device, it is broadly classified into low-dose rate (LDR) and high-dose rate (HDR) brachytherapy. LDR brachytherapy is a treatment modality in which radioactive seeds are generally implanted within a patient. These seeds commonly use low-energy photon-emitting sources such as ^{125}I or ^{103}Pd radioisotopes for treatment. Figure 2.1 presents illustrations of two such sources containing the ^{103}Pd radioisotope. The AAPM TG-43 report and its associated updates (Nath et al. 1995, Rivard et al. 2004; 2007) recommend a protocol to characterize these sources, and described the relevant dosimetric parameters in great detail. Since the publication of the report, there have been various advances in the design and geometry of these devices. Examples of such devices include CivaString$^{\text{TM}}$, OptiSeed$^{\text{TM}}$, RadioCoil$^{\text{TM}}$ and SmartSeed$^{\text{TM}}$ all of which have tried to improve upon the dose distribution conformity for specific treatments. (Reed et al. 2014b, Meigooni et al. 2004, Bernard and Vynckier 2005, Wang and Hertel 2005, Abboud et al. 2010)

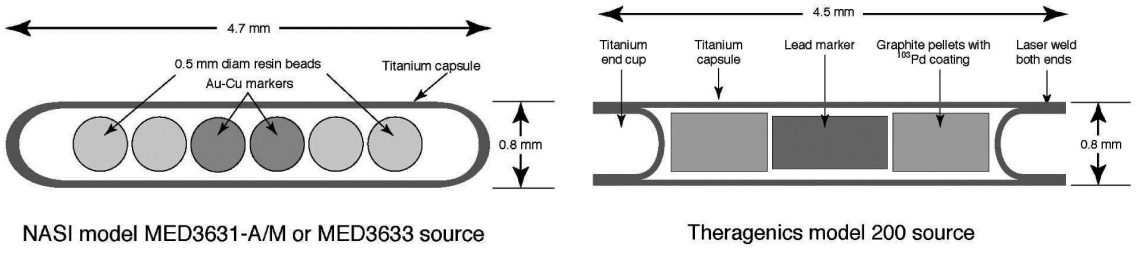

(a) (b)

Figure 2.1: Illustrations of two of the brachytherapy seeds containing Pd-103 isotope examined in the TG-43 report (Rivard et al. 2004) a. NASI model MED3631-A/M or MED3633 source, b. Theragenics Corp. model 200 source. Reproduced with permission from the Medical Physics journal.

2.1.1 Conventional LDR brachytherapy source arrays and directional LDR sources

For clinical interstitial implants, devices consisting of arrays of conventional cylindrically symmetric LDR brachytherapy sources such as ^{125}I seeds embedded into a vicryl mesh (Colonias et al. 2011) and ^{131}Cs BrachyMesh^{TM} commercially produced previously by IsoRay Medical, Inc. (Richland, WA) (Yang and Rivard 2011) have been used. The arrays have specifically been used for the treatment of non-small-cell lung cancer. (Johnson et al. 2007, Murphy et al. 2004) These have been shown to result in improvements in local recurrence. (Santos et al. 2003, Voynov et al. 2005) Figure 2.2 is an illustration of a BrachyMesh array which uses a conventional cylindrically-symmetric seed design.

Most brachytherapy seeds are cylindrically symmetric and have isotropic azimuthal radiation emission. If the source geometry and design could be modified such that the emission was more directional, then such an adaptation could potentially improve the therapeutic ratio for a given brachytherapy treatment when compared to conventional sources, by selectively targeting diseased tissue and sparing the surrounding healthy structures.

Lin et al. conceptualized a directional LDR brachytherapy source as shown in Fig 2.3. (Lin et al. 2008) It is comprised of gold material present inside a conventional I-125 seed

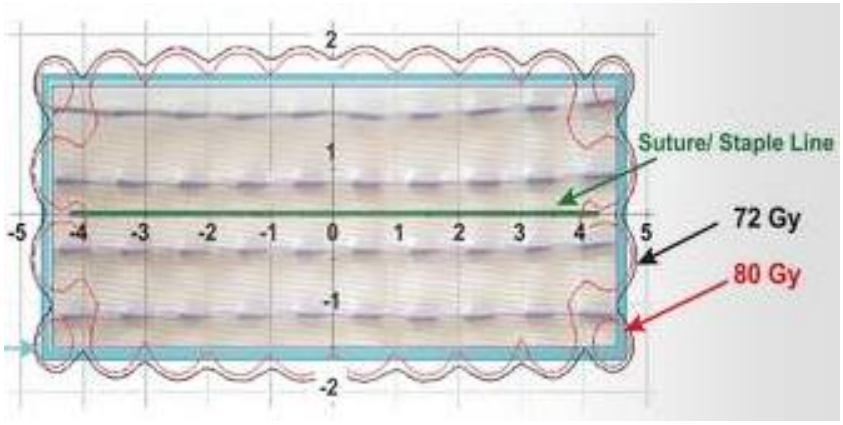

Figure 2.2: An illustration of the BrachyMesh™ (Image source: isoray.com)

design which attenuated radiation on one side of the device, hence providing directionality to the radiation output of the source. Lin et al. and Chaswal et al. investigated the implications of using such directional interstitial brachytherapy sources and found significant reduction in dose to normal tissue for breast and prostate cancer treatments, respectively using Monte Carlo methods. (Lin et al. 2008, Chaswal et al. 2012)

2.2 CivaSheet

CivaTech Oncology, Inc. (Durham, NC) has developed a novel directional ^{103}Pd planar source array called the CivaSheet for use in LDR brachytherapy cancer treatments. (Aima et al. 2015) In principle, the CivaSheet can be used for the treatment of various tumors, such as early stage non-small-cell lung cancer, head and neck cancer, colorectal cancer, ocular melanoma, soft tissue sarcoma, skin cancer among other sites. Currently, there are ongoing clinical trials for investigating its efficacy for pancreatic, abdomino-pelvic, and colorectal cancer treatments (trials NCT03109041, NCT02843945, NCT02902107)

The CivaSheet is an array of discrete ^{103}Pd source elements called CivaDots. Figure 2.4 is an illustration of a CivaSheet comprised of nine CivaDots. Fenestrations are manufactured in the bio-absorbable membrane material for surgical purposes. The CivaSheet is intended

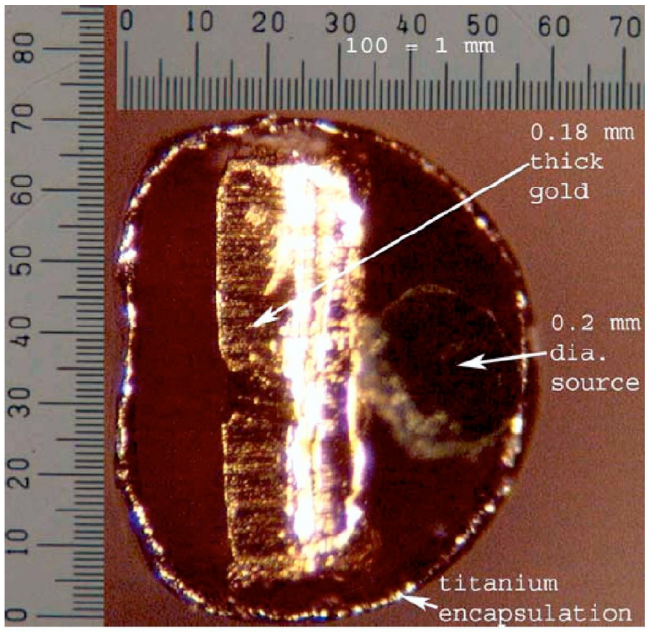

Figure 2.3: A transverse plane cross section image of a directional LDR source conceptualized by Lin et al. (Lin et al. 2008) Reproduced with permission from the Medical Physics journal.

to be scalable to the size of the treatment area and can thus contain a variable number of CivaDots in a customized array. The largest CivaSheet will be an array of 108 CivaDots placed in 18 rows of 6, yielding a CivaSheet area of 5×15 cm^2 with 8 mm spacing between the center of each CivaDot.

2.2.1 CivaDot

A CivaDot consists of a small cylindrical ^{103}Pd source held within an organic polymer capsule with epoxy sealing and a gold shield on one side. The capsule is encased in a bio-absorbable polymer. The gold shield helps define the "hot" and the "cold" side of the device. Figure 2.5 is an illustration of the CivaDot with its various constituents.

The details of the dimensions, material compositions, material densities, and distribution of radioactive ^{103}Pd material within the CivaDots were obtained from CivaTech Oncology, Inc. The CivaDots consist of a cylindrically-shaped region that contains ^{103}Pd, a low-Z

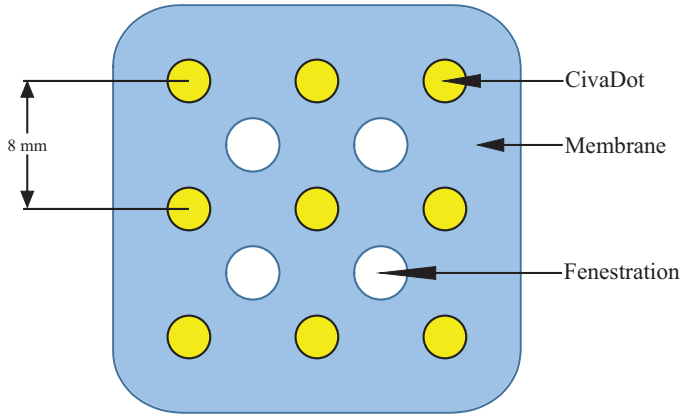

Figure 2.4: A schematic of a sample CivaSheet^{TM} array of nine CivaDots. The CivaDots are all oriented such that the gold shields are on the same side and are embedded in a flat bio-absorbable membrane. Fenestrations manufactured in the material are shown as white circles. Note that the illustration is not to scale. (Aima et al. 2015) Reproduced with permission from the Medical Physics journal.

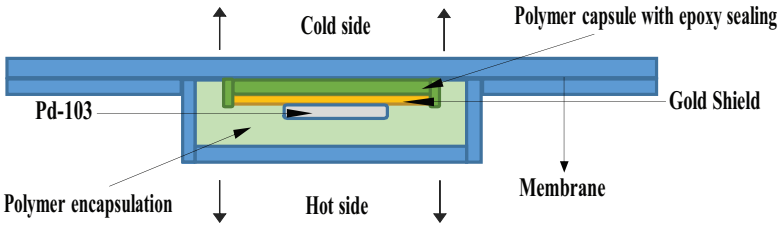

Figure 2.5: An illustration of the CivaDot with its components in a cross-sectional view. The schematic illustrates the region of ^{103}Pd and the gold layer for shielding. The cold direction corresponds to the side of the CivaDot with the gold shield. Please note that the illustration is not to scale. (Aima et al. 2015)

organic polymer encapsulation, a gold disc-shaped shield, and a bio-absorbable membrane encasing all of the sources in an array.

The cylindrical organic polymer capsule of the CivaDot has an outer radius of 1.265 mm and thickness of 0.490 mm. Centered in the capsule along the cylindrical axis is a thin ^{103}Pd region with a radius of 0.20 mm and a height of 0.080 mm. The bottom of this region is 0.365 mm from the hot side of the source (with the bio-absorbable membrane material present) and is defined as the reference plane (or zero distance) for measurements of S_{K}. The intersection of the cylindrical axis of the CivaDot and the reference plane is defined as the origin for the measurements and Monte Carlo simulations. Secured above the palladium region is a thin cylindrical layer of gold intended to attenuate the source on the cold side. This gold layer has an outer radius of 0.925 mm and a thickness of 0.050 mm and is centered on the cylindrical axis of the CivaDot at a distance of 0.1 mm from the reference plane. The entire CivaDot is enclosed between two bio-absorbable 0.125 mm uniformly thick membranes.

2.2.2 CivaDot ^{103}Pd loading

The CivaDots have an active palladium region which contains ^{103}Pd material of variable loading. The amount of ^{103}Pd that is loaded into a given CivaDot is based on the prescription dose and the specific activity of ^{103}Pd. With different ^{103}Pd loading schemes, the energy spectrum emerging from the source will change due to changes in the absorption of fluorescence L-shell x rays originating in the gold shield. This variation can potentially impact source strength determination and dose distribution characterization. This work takes into account the impact of this variation by estimating uncertainties around the 50% loading. The work assumed the ^{103}Pd region to be uniformly filled with 50% palladium material and 50% epoxy by mass, with the net density of $\rho = 1.9987\,\mathrm{g\,cm^{-3}}$ and then es-

timated uncertainties for 20% and 80% palladium loading configurations for all dosimetric parameters determined.

2.3 Conventional LDR brachytherapy source dosimetry

Nath et al. and Rivard et al. in their seminal publications established a formalism for the dosimetric characterization of conventional LDR brachytherapy sources. (Nath et al. 1995, Rivard et al. 2004; 2007) These traditional sources were cylindrically symmetric and have isotropic azimuthal emission. Figure 2.6 shows the coordinate system used for the dosimetry of these sources.

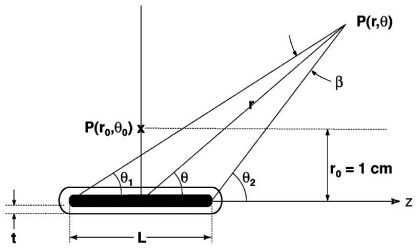

Figure 2.6: TG-43 coordinate system used for dosimetry of conventional LDR brachytherapy sources. (Rivard et al. 2004) Reproduced with permission from the Medical Physics journal.

2.3.1 AAPM TG-43 dosimetric formalism

The AAPM TG-43 proposed formalism is the standard system for the calculation of dose rate in water at different positions around a conventional brachytherapy seed. It uses a parameterized formalism which as seen in Figure 2.6 is based on a polar coordinate system. The authors of the TG-43 report proposed the following formalism:

$$\dot{D}(r,\theta) = S_{\mathrm{K}} \cdot \Lambda \cdot \frac{G_X(r,\theta)}{G_X(r_0,\theta_0)} \cdot g_X(r) \cdot F(r,\theta), \tag{2.1}$$

where $\dot{D}(r,\theta)$ is the absorbed dose-rate-to-water in water at distance r (in cm) and angle θ from the source, S_{K} is air-kerma strength of the source, measured as the averaged

source strength on the transverse axis of the source in vacuum at 1 meter, Λ is the dose-rate constant, defined as the ratio of absorbed dose-rate-to-water at 1 cm to the S_{K} on the transverse axis of the source, and $G_X(r,\theta)$, $g_X(r)$, $F(r,\theta)$ are the geometric, radial, and anisotropy functions, respectively.

2.3.2 Limitations of the TG-43 formalism

In the case of the CivaSheet, the directional as well as planar nature of the source array renders the direct application of the TG-43 protocol inappropriate. The dosimetric parameters as defined by Equation 1 are not directly applicable for a directional as well as a planar source array. The definitions of S_{K}, Λ, $G_X(r,\theta)$, $g_X(r)$, and $F(r,\theta)$ need to be adapted to accommodate this source. Also, S_{K} determination of an entire array of sources is not feasible, as such a measurement would require a free-air chamber with a very large aperture, which does not currently exist.

2.4 Source strength determination for planar-directional source arrays

The University of Wisconsin Variable-Aperture Free-Air Chamber (UW VAFAC) (Culberson et al. 2006) is a research instrument that can perform primary S_{K} measurements for low-energy LDR sources. It is a large-volume free-air chamber with five available aperture sizes. It is similar in design to the National Institute of Standards and Technology Wide-Angle Free-Air Chamber (NIST WAFAC) (Seltzer et al. 2003), which is the U.S. national primary standard for S_{K} determination of LDR sources (single fixed aperture). The UW VAFAC has been used for the primary S_{K} measurements of coiled ^{103}Pd sources (Paxton et al. 2008) and 1 cm long ^{103}Pd sources (Reed et al. 2014b) in addition to conventional ^{103}Pd, ^{125}I sources. (Culberson et al. 2006)

This work makes use of the UW VAFAC to perform primary S_K measurements of the CivaDot. The source strength determination of an entire CivaSheet is not feasible due to free-air chamber aperture size and volume limitations. This work uses an element-based approach, by first determining the source strength of the CivaDot experimentally and then using Monte Carlo methods for an array-based framework.

The air-kerma strength definition as recommended by the TG-43 protocol has to be adapted to accommodate directional sources. To realize the S_K of a CivaDot, several investigations have to be performed, which are listed as follows:

1. Spectral and anisotropy measurements: The energy spectrum and the anisotropy of a source impact the correction factors applied to the free-air chamber measurements to correct it to a corresponding vacuum measurement. The emitted energy spectrum and the anisotropy of the CivaDot thus need to be measured to estimate S_K accurately. These measurements are used to benchmark the Monte Carlo model of the source as well. This is an important investigation for this source due to the presence of a gold shield in the vicinity of the active ^{103}Pd volume, which not only provides directionality but also alters the source spectrum compared to conventional ^{103}Pd sources.

2. Monte Carlo simulations: A model of the CivaDot has to be developed for Monte Carlo simulations to provide a comparative reference for the source energy spectrum, source anisotropy, and the free-air chamber measurements. Once benchmarked, this model can be used to develop a CivaDot-CivaSheet source strength and dosimetric framework.

3. A number of correction factors are applied to the UW VAFAC measurements to realize S_K. Correction factors have to be determined for this source for the raw free-air chamber measurements based on Monte Carlo methods, spectral, and anisotropy mea-

surements. These corrections are calculated either analytically or with Monte Carlo techniques.

4. An investigation is also required to test the feasibility of transferring the primary S_K measurement to an instrument that can be used for clinical S_K verification. Consistency in the ratio of the S_K to well chamber response over multiple measurements needs to be tested for validating robustness of this transfer.

2.5 Dosimetry for planar-directional source arrays

2.5.1 Conventional LDR brachytherapy source arrays

The individual elements of traditional LDR ^{125}I and ^{131}Cs brachytherapy source arrays (Colonias et al. 2011, Yang and Rivard 2011) are calibrated according to the methods of the AAPM TG-43 report. (Nath et al. 1995, Rivard et al. 2004; 2007) The U.S. standard for determination of the S_K of low-energy LDR brachytherapy sources, i.e., the NIST WAFAC, is used for the determination of the source strength of an element of the traditional source arrays. The S_K is measured for each source individually using a well chamber (traceable to NIST WAFAC) and then dose to water calculations are performed by using published TG-43U1 tabulated data. Since multiple sources are sutured into an array, the superposition of all the elements of an array is calculated and tabulated in the form of a dose lookup table. (Johnson et al. 2007)

2.5.2 CivaSheet

This work proposes a similar element-based (CivaDot) approach for source strength determination for the CivaSheet array. However, in the case of the CivaSheet and more specifically the CivaDots, their directional nature precludes the direct application of the Task Group 43 protocol. The dosimetric characterization of a CivaDot needs to be performed, with

an investigation conducted to study the dose distribution of the source in phantom and to validate the Monte Carlo model. The TG-43 formalism needs to be adapted and dosimetric analog parameters for the CivaDot source need to be determined.

2.5.3 CivaDot dose distribution characterization

The dosimetric characterization of conventional brachytherapy LDR sources is usually performed in a water-equivalent plastic phantom using a detector such as the thermoluminscent dosimeter, and/or using Monte Carlo methods. (Reed et al. 2014b, Meigooni et al. 2004, Bernard and Vynckier 2005, Wang and Hertel 2005, Abboud et al. 2010) The dose distribution is measured around the sources at various locations and then the associated dosimetric parameters are calculated using Equation 1. For this purpose of this work, similar phantoms need to be fabricated but their design needs to be adapted to consider the directionality and the unique geometry of the CivaDot. A new coordinate system for source dosimetry is required. Materials such as polymethyl methacrylate (PMMA) and Virtual Water$^{\text{TM}}$ were considered for the phantom. Given the CivaDot design, a dosimeter such as radiochromic film, specifically EBT3 GafChromic Film manufactured by Ashland Inc. (Convington, KY), was investigated for its appropriateness for source dosimetric characterization. Such a two-dimensional dosimeter provides increased measurement resolution and conforms better to the planar design of the CivaSheet. To determine the CivaDot dose distribution using measurements, various correction factors need to be calculated or measured. These include correction for the presence of a plastic phantom and a dosimeter instead of a water medium. Monte Carlo simulations need to be performed consisting of the geometries modeling the source, measurement setup and the dosimeters used; these can provide a comparative reference for our measured dose distributions.

2.5.4 CivaSheet dose distributions

A dosimetric framework can be established for the CivaDot source strength to CivaSheet dose distribution conversion once the Monte Carlo simulations of the CivaDot dose distributions are validated using measurements. Measurements of smaller sized CivaSheets need to be performed to check the accuracy of the Monte Carlo framework and also to test the validity of dosimetric superposition of individual CivaDots to estimate the overall CivaSheet dose distributions. Formulation of a clinically viable dosimetric protocol can then be performed for the CivaSheet based on an adapted TG-43 formalism.

2.6 Project motivation and goals summary

The use of directional LDR radioactive sources can potentially lead to an improvement in the therapeutic ratio for brachytherapy treatments. The use of current dosimetric formalisms and guidelines (Rivard et al. 2004, Nath et al. 1997, Butler et al. 2008, DeWerd et al. 2006) established for conventional cylindrically symmetric and azimuthally isotropic seeds is precluded for directional and planar devices such as the CivaSheet. This work primarily aims to adapt current dosimetric formalisms and guidelines as well as present new methods to accommodate such sources. When a novel source such as the CivaSheet is introduced commercially, a thorough investigation needs to be conducted to ascertain the source strength and the dosimetric characteristics of the source. The work lays out the procedure for the complete dosimetric characterization of such novel sources. Specifically for the CivaSheet, the work first aimed to determine the source strength of an element of the CivaSheet array (CivaDot) using a primary measurement technique, and tested the feasibility of establishing a calibration coefficient for a clinical transfer to an instrument such as the well-type ionization chamber. This included complete characterization of the CivaDot using spectral and anisotropy measurements as well as Monte Carlo methods. Primary air-kerma strength measurement methods presented in this work assisted in the establishment of the primary

source strength standard for the CivaDot at NIST using the WAFAC. The next goal was to perform a dosimetric characterization of the CivaDot and establish an adapted dosimetric formalism for the CivaDot using measurements and Monte Carlo methods. Finally, the project aimed to establish the CivaDot-CivaSheet dosimetric framework, measure and predict CivaSheet dose-to-water distributions, and formulate a clinically viable dosimetric protocol for the CivaSheet based on an adapted TG-43 formalism.

Chapter 3

Source Strength Determination for a Directional Source

3.1 Primary source strength measurements

The authors of the American Association of Physicists in Medicine (AAPM) Task Group No. 43 report (Nath et al. 1995) and its associated Update of AAPM Task Group No. 43 Report (TG-43U1) (Rivard et al. 2004; 2007) proposed a formalism, which is the standard system for the dosimetric characterization of a brachytherapy sources. The formalism is:

$$\dot{D}(r,\theta) = S_{\mathrm{K}} \cdot \Lambda \cdot \frac{G_X(r,\theta)}{G_X(r_0,\theta_0)} \cdot g_X(r) \cdot F(r,\theta), \tag{3.1}$$

where $\dot{D}(r,\theta)$ is the absorbed dose-rate to water in water at distance, r (in cm), and angle θ from the source, S_{K} is air-kerma strength of the source, measured as the averaged source strength on the transverse axis of the source in vacuo at 1 meter, Λ is the dose-rate constant, defined as the ratio of absorbed dose-rate-to-water at 1 cm to the S_{K} on the transverse axis of the source, and $G_X(r,\theta)$, $g_X(r)$, $F(r,\theta)$ are the geometric, radial, and anisotropy functions, respectively.

The preferred metric for the source strength determination of a brachytherapy source was listed as air-kerma strength. This was defined by the report as:

$$S_{\mathrm{K}} = \dot{K}_{\delta} \cdot d^2 \tag{3.2}$$

where $\dot{K}_{\delta}$ is the air-kerma rate in vacuo due to photons of energy greater than δ, and d is the distance. The units of S_{K} are U, where 1 U = 1 μGy m^2 h^{-1} or 1 cGy cm^2 h^{-1}. The point of measurement for S_{K} is located on the transverse plane of the source. The distance of measurement for $\dot{K}_{\delta}$ was set at 1 m. To conform to the in-vacuo definition provided by TG-43, the free-air chamber measurements should be corrected for photon attenuation and scattering in air or from the instrument and surrounding media. The energy cutoff, δ, was set to 5 keV to exclude contaminant photons from titanium source cladding present in conventional brachytherapy sources.

Seltzer et al. provided a method to calibrate the source strength for low-energy photon-emitting LDR brachytherapy sources using S_{K} as the metric. (Seltzer et al. 2003) This publication outlined the establishment of the U.S. national standard for determination of the S_{K} of low-energy LDR photon-emitting brachytherapy sources, known as the National Institute of Standards and Technology Wide-Angle Free-Air Chamber (NIST WAFAC).

3.2 University of Wisconsin Variable-Aperture Free-Air Chamber

The University of Wisconsin Variable-Aperture Free-Air Chamber (UW VAFAC) is a large-volume free-air chamber much like the NIST WAFAC, but with five replaceable aperture sizes instead of a single fixed aperture. (Culberson et al. 2006) The UW VAFAC can be used for S_{K} measurements of brachytherapy sources with photon energies up to 70 keV. (Culberson et al. 2006, Paxton et al. 2008, Reed et al. 2014b, Aima et al. 2015) The UW

VAFAC has been used for the primary calibration of coiled ^{103}Pd sources (Paxton et al. 2008) and more recently for the calibration of a new 1 cm long ^{103}Pd source. (Reed et al. 2014b)

The sensitive collecting volume of the UW VAFAC is 40 cm in diameter and is positioned 20 cm downstream from the plane of the collimating aperture stand. The source to be measured is secured behind a shielded enclosure and the aperture stand is mounted at a fixed distance of 30 cm from the source. (Culberson et al. 2006) Figure 3.1 shows a schematic of the UW VAFAC, with the CivaDot in its measurement position. The VAFAC operates as an air ionization chamber and utilizes the change in the ionization current as a function of plate separation to determine the air kerma produced at a well-defined distance from the source.

The measurement procedure involves recording multiple ionization current measurements with electrode separations ranging from 5 cm to 15 cm, as described in detail by Culberson et al. and Paxton et al. (Culberson et al. 2006, Paxton et al. 2008) Linear regression techniques are used to fit the measurement data and determine a corrected ionization current per unit distance of electrode separation $d(kI)/ds$. This value is used to determine the S_{K} of the source as shown in Equation 3.3. For each source, the measurement is repeated without repositioning to calculate the measurement repeatability. An average S_{K} of all measurements is taken to be the final S_{K} of the source.

The UW VAFAC determines S_{K} by using the following equation (Culberson et al. 2006):

$$S_{\mathrm{K}} = (\overline{W}/e)_{\mathrm{air}} \frac{d^2}{\rho_{\mathrm{air}} A_{\mathrm{eff}} (1 - g_{\mathrm{air}})} \cdot \frac{d\,(kI)}{ds} \cdot \prod_i k_i, \tag{3.3}$$

where $(\overline{W}/e)_{\mathrm{air}} = 33.97\,\mathrm{eV}$ (Boutillon and Perroche-Roux 1987) is the mean energy required to produce an ion pair in dry air, $\rho_{\mathrm{air}} = 1.196\,\mathrm{kg\,m^{-3}}$ is the density of air in the chamber at 22 °C and 101.325 kPa, A_{eff} is the effective area of the beam collimating aperture, g_{air} is the fraction of the initial electron energy lost by radiative processes in air ($g_{\mathrm{air}} \approx 0$ for en-

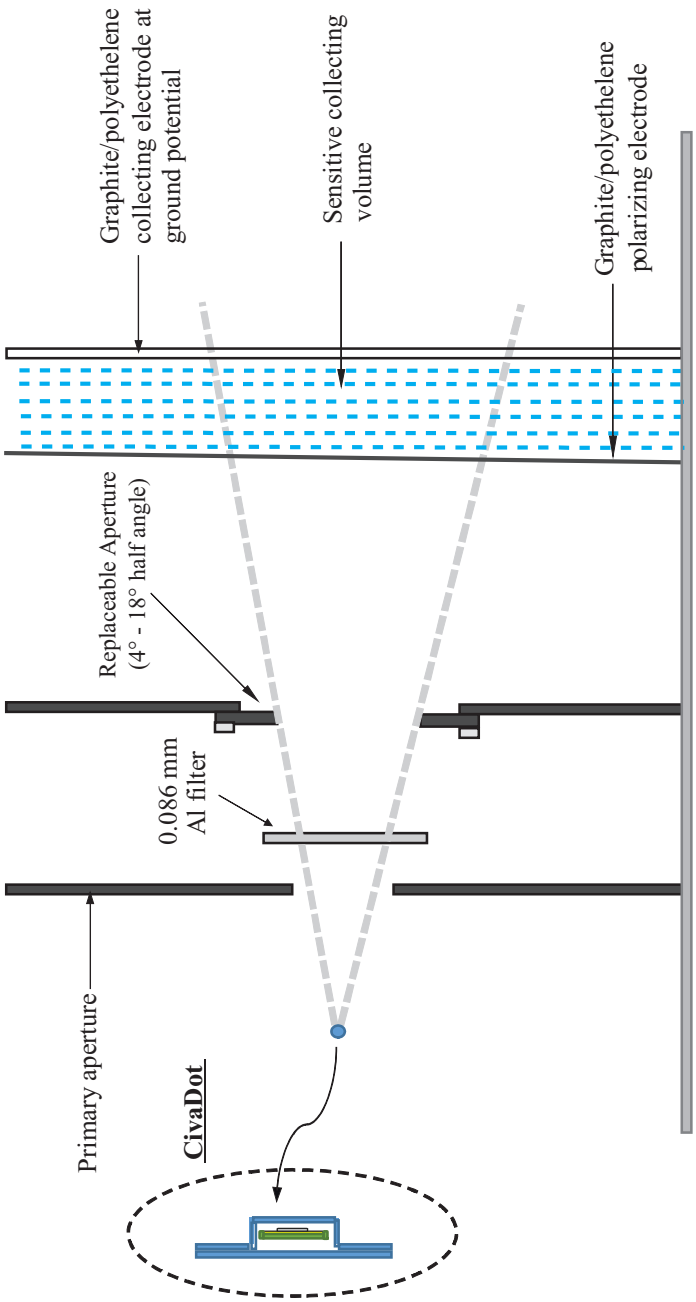

Figure 3.1: Schematic of the measurement setup with a CivaDot in its fixed measurement position with the UW VAFAC. Please note that the illustration is not to scale.

ergies less than 100 keV), $\frac{d(kI)}{ds}$ is the increment of corrected ionization current (background and leakage subtracted, corrected to reference temperature and pressure) per increment of the electrode separation (s), and k_i's are source-specific correction factors applied to the measured currents.

Since no primary measurement was previously performed on directional ^{103}Pd LDR brachytherapy sources, this investigation was focused on the determination of the S_{K} for individual CivaDots of a CivaSheet with the UW VAFAC. The definition of air-kerma strength was adapted to a static on-axis measurement, with the source held static during the measurements, to accommodate the planar and directional nature of the CivaDot. Given the the directional design, there is no need to average over the azimuthal anisotropy as with traditional LDR sources.

The air-kerma strength of a CivaDot can be determined using appropriately calculated correction factors for the source. The correction factors account for the materials present in the UW VAFAC setup and also the unique energy spectrum emitted from the CivaDots. The correction factors were calculated primarily by using Monte Carlo techniques. With the presence of gold in the vicinity of the active ^{103}Pd volume in a CivaDot, the source energy spectrum will be different than that of traditional sources due to the production of fluorescent x rays in the gold shield. To evaluate and benchmark the Monte Carlo calculated spectra, measurements were performed with a low-energy high-purity germanium (HPGe) detector and compared with the spectrum predicted by the Monte Carlo simulations.

The UW VAFAC has five sizes of interchangeable brass apertures, which are held in place 30 cm from the source. For all measurements in this work, either aperture No. 3 (VA3) or aperture No. 2 (VA2) was used. The aperture collimates the radiation emitted from the CivaDot into a cone with a half angle of 10.39° for VA3 and 7.6° for VA2. The NIST WAFAC aperture has a half angle of 7.6° and is thus similar to VA2 aperture. The aperture collimates the primary beam and penumbra of the source such that they are

completely contained within the sensitive collecting volume of the UW VAFAC. The use of VA3 for S_K measurements provides an improved signal-to-noise ratio (1.5 to 2 times) over VA2 for sources of lower strength. To be consistent with the TG-43U1(Rivard et al. 2007) definition of S_K, a high-purity 0.086 mm aluminum filter is positioned in the beam path to remove photons with energies less than 5 keV. This is similar to the NIST WAFAC measurement protocol, although it should be noted that the filter is not necessary for the CivaDot measurements since there is no titanium cladding around the source. (Seltzer et al. 2003)

3.2.1 CivaDot measurement setup

To accommodate the unique CivaDot design, a new source holder was developed to secure a CivaDot during measurements. The source needed to be secured while minimizing the surrounding scatter media. It was also important for the cylindrical axis of the CivaDot to be aligned with the cylindrical axis of the UW VAFAC. To this end, a window-frame-shaped PMMA holder with an outer width of 8.5 cm and an inner width of 5 cm in the horizontal direction was used to suspend the CivaDot in air. An image of the custom holder fabricated for the CivaDot measurements is shown in Figure 3.2. Four plastic screws were used to secure the source within the holder.

A schematic of a CivaDot in place for measurements is shown in Figure 3.3. Regarding CivaDot orientation, the hot side was always set to face the collecting volume and the front face of the outer bio-absorbable membrane was used for initial alignment. A side laser was used to align the front face of the membrane 30 cm from the plane of the defining aperture. An offset of 0.365 mm was then introduced by a precision translation stage so as to place the source origin in the same location as the VAFAC origin. The CivaDot source origin was set as the intersection of cylindrical axis of the CivaDot with the bottom of the palladium

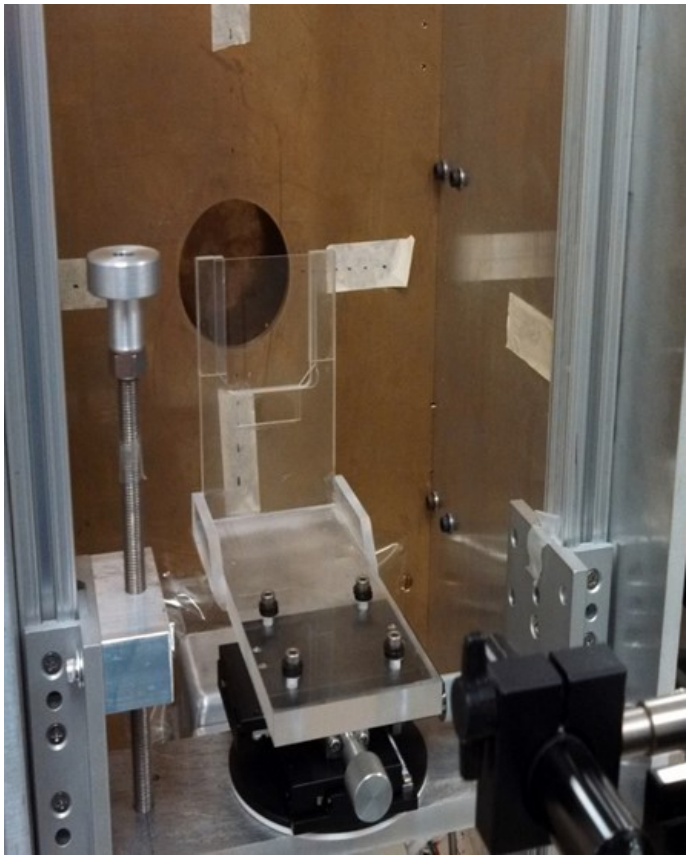

Figure 3.2: A photograph of the custom CivaDot holder in its measurement position with the UW VAFAC. The PMMA holder is screwed onto an adjustable base, and the hot side of the source faces the brass aperture.

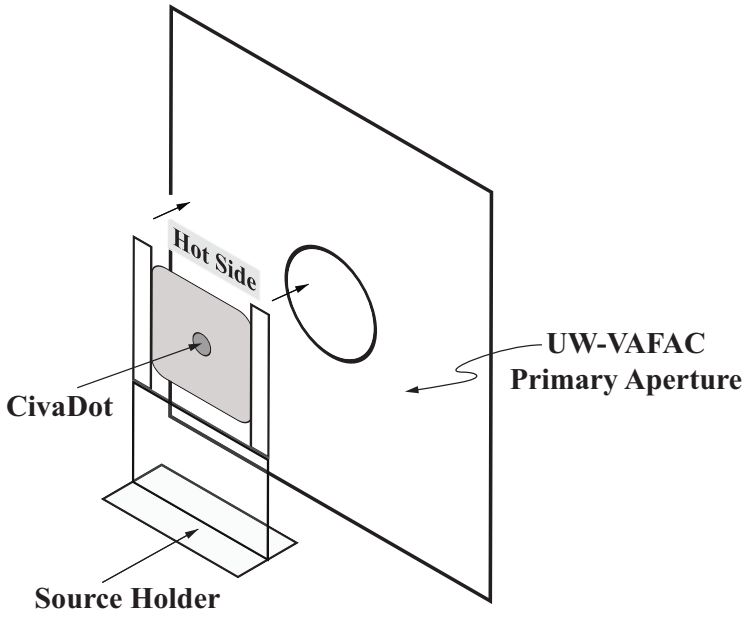

Figure 3.3: Schematic of a CivaDot in its PMMA window-frame holder for UW VAFAC measurements. Note that the illustration is not to scale.

region. As the definition of air-kerma strength was adapted to a static on-axis measurement, the source was held static during the measurements.

3.2.1.1 CivaDot ^{103}Pd loading

As described in Chapter 2, the CivaDots have an active palladium region which contains ^{103}Pd material of variable loading. The amount of ^{103}Pd that is loaded into a given CivaDot is based on the prescription dose and the specific activity of ^{103}Pd. With different ^{103}Pd loading schemes, the energy spectrum emerging from the source will change due to changes in the absorption of fluorescence L-shell x rays originating in the gold shield. This variation is small, but requires attention with regard to the correction factors for S_{K} measurements. In this work, all the Monte Carlo simulations assumed the ^{103}Pd region to be uniformly filled with 50% palladium material and 50% epoxy by mass, with the net density of $\rho = 1.9987\,\mathrm{g\,cm^{-3}}$.

3.2.2 CivaDot energy spectrum study

The existence of the gold shield in such close proximity to the ^{103}Pd region creates a spectrum that is different than that of traditional LDR ^{103}Pd brachytherapy seeds. This spectrum can be calculated with Monte Carlo methods using appropriate cross-section libraries. For this study, a Canberra Industries Inc. (Meriden, CT) low-energy high-purity germanium (HPGe) spectrometer was used to verify the calculated spectrum by measuring the pulse height distribution with the CivaDot secured in air with the same holder that was used for UW VAFAC measurements. The HPGe detector was positioned on the CivaDot cylindrical axis to capture the spectrum in the same emission direction as the UW VAFAC. At the beginning of the measurement session, a detector energy calibration was performed using ^{109}Cd, ^{55}Fe, and ^{241}Am sources, all of which have photon emissions in the $< 60\,\text{keV}$ energy range.

To clearly identify the spectral effects of the gold shield, a custom unshielded CivaDot was manufactured by CivaTech Oncology, Inc. and used to compare with a shielded CivaDot. The spectra of the shielded and the unshielded CivaDot were measured with the HPGe detector system sequentially in the same measurement session, thus having the same detector energy calibration. Pulse-height distributions with acquisition times $>20\,\text{hours}$ were recorded for both the CivaDot with gold shield and CivaDot without gold shield. The difference spectrum was used to analyze the spectral effects introduced by the gold shield by using a subtractive technique. This technique was performed by calculating the difference between the normalized spectra of the shielded and the unshielded CivaDot for each channel.

3.2.2.1 CivaDot energy spectrum results

The pure ^{103}Pd source spectrum is assumed to be accurate since it is based on the well-established NUDAT 2.6 database. (Brookhaven National Laboratory) Therefore, the focus

of this spectral study was on the gold fluorescent x-ray radiation due to the presence of the gold shield. The results of the CivaDot spectral measurements and calculations are plotted in Figures 3.4 and 3.5. Figure 3.4 shows two measured spectra, one from a specially constructed CivaDot without the gold shield and one from a typical CivaDot. The spectra were both normalized to peak heights of the most abundant 20.2 keV ^{103}Pd emission line. Figure 3.5 shows the difference of the two spectra to highlight the impact of the gold shield. One can see the difference in the spectra in the range of (8 keV to 15 keV) where the CivaDot without gold does not emit L-shell fluorescence x rays. In addition to the difference spectrum shown in black, the MCNP6 Monte Carlo-predicted difference spectrum is shown in gray. It is clear that the measured difference spectrum is consistent with the calculated difference spectrum in the area of interest (8 keV to 15 keV). This agreement is important since spectra calculated with previous versions of MCNP (version 5) had a mismatch with the measured spectra in this energy range. The results of this investigation verify the adequate simulation of the discrete L-shell gold fluorescent x rays originating in the gold shield using MCNP6 with the updated photon cross section library (.12p). It should be noted that the measured data was not corrected with a detailed detector response function.

3.2.3 CivaDot Anisotropy

Since the conventional definition of S_K was adapted to an on-axis static measurement for this work, it is important that the source emission is uniform within the free-air chamber measurement aperture. To determine the S_K of a source with the UW VAFAC, a relatively large aperture (half angle of 10.39°) may be used. Although not all traditional sources emit uniformly within the aperture used by the NIST WAFAC, it is a desirable feature to enable future comparisons with multiple large-volume free-air chambers.

To quantify the anisotropy of the CivaDot within the UW VAFAC measurement aperture, a sodium-iodide (NaI) detector manufactured by Ludlum Measurement, Inc. (Sweet-

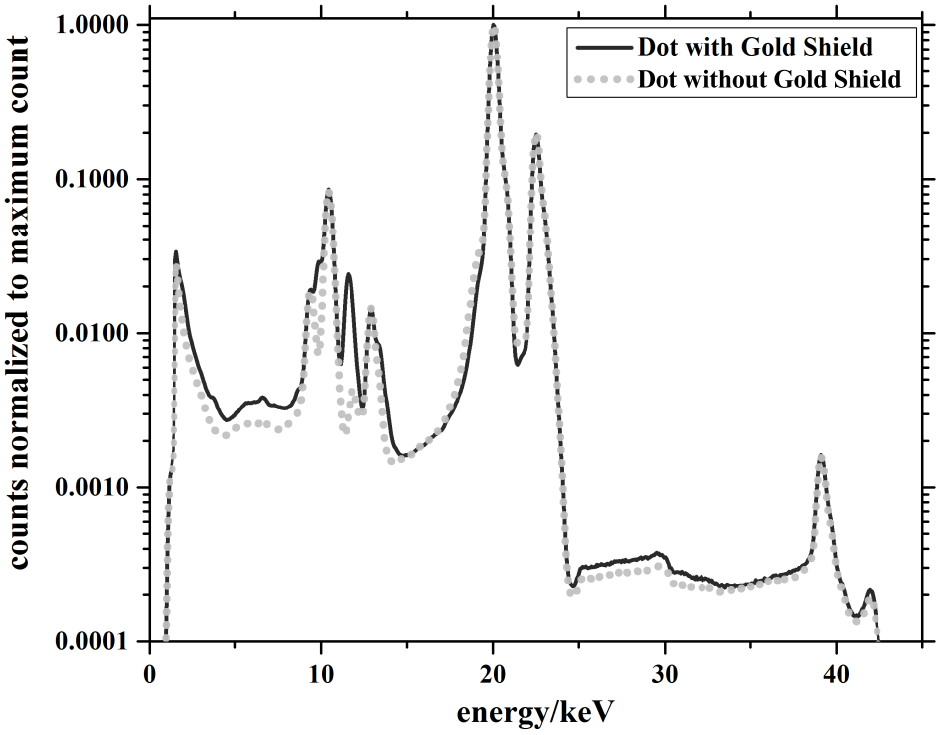

Figure 3.4: Results of the HPGe spectra measurements of a typical CivaDot (shown in black) and a specially constructed CivaDot without the gold shield (shown in gray) normalized to maximum count.

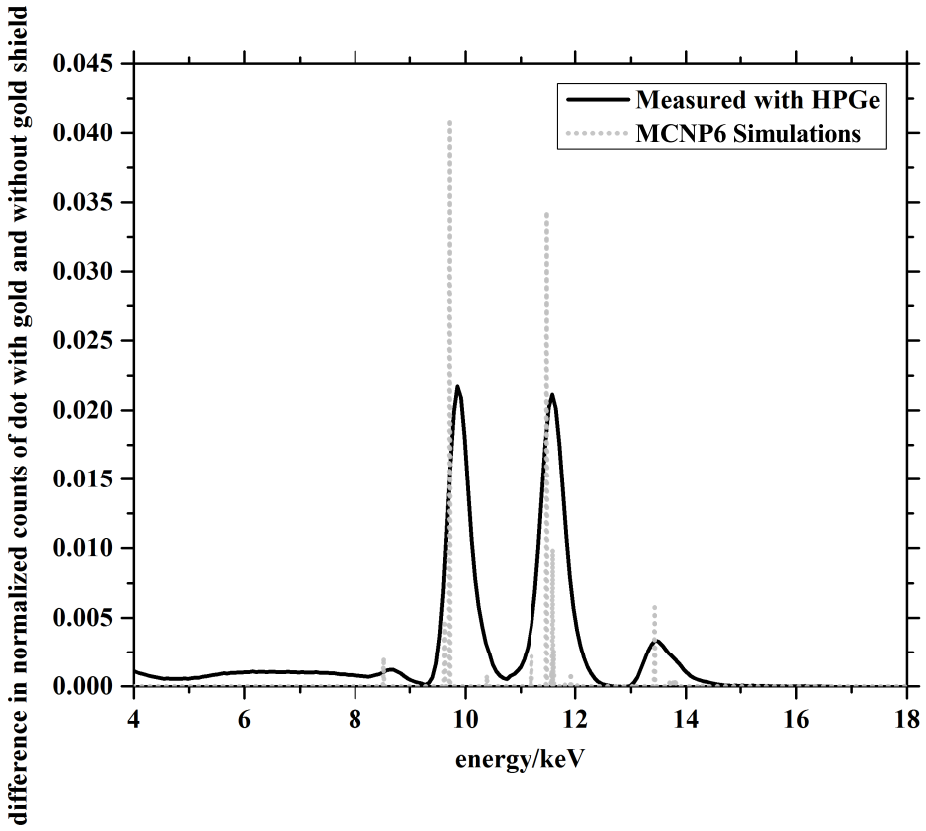

Figure 3.5: The results of the HPGe differential measurements for a typical CivaDot and a special CivaDot without the gold shield. Also shown is the MCNP6 Monte Carlo calculated difference spectrum for the CivaDots.

water, TX) was used. This NaI detector was mounted at a distance of 95 cm from the source and the CivaDot was rotated in discrete steps while acquiring counts with the NaI detector. Measurements with an acquisition time of 60 s were performed at each angle in 1° increments. A Monte Carlo simulation of the measurement setup was performed for comparison. An analysis was performed in the central measurement region for estimating any azimuthal anisotropy due to source construction.

Figure 3.6 shows the measured angular fluence distribution measured with a NaI detector and predicted with MCNP6 Monte Carlo simulations around a CivaDot for two UW VAFAC apertures (Aperture No. 2 and No. 3). The zero degree angle is defined with the CivaDot in its S_{K} measurement position (cylindrical axis of the CivaDot in alignment with the cylindrical axis of the UW VAFAC) for both the measurements and Monte Carlo simulations. The impact of the gold shield on the CivaDot anisotropy distribution is noticeable, with very few counts on the cold side of the source compared to the hot side of the source, hence demonstrating the directional nature of the source. Statistical uncertainties at individual measurement points were generally 1% or less. There is also a noticeable dip in the fluence around 90° and 270° due to attenuation in the bio-absorbable membranes.

In the angle defined by the UW VAFAC aperture No. 3 (half angle of 10.39°) and No. 2 (half angle of 7.6°), the measured and simulated fluence at each discrete angle (intervals of 1°) is equal to the distribution on the central axis to within the uncertainty in both the measured and predicted results. This means that a comparison can be made with other apertures smaller than UW VAFAC aperture No. 3 without having to correct for any anisotropy within the aperture-defined collecting volume. This result also implies that positioning sensitivity of the CivaDot while performing an S_{K} measurement with either of the two apertures is not a major concern and is not a source of large uncertainty.

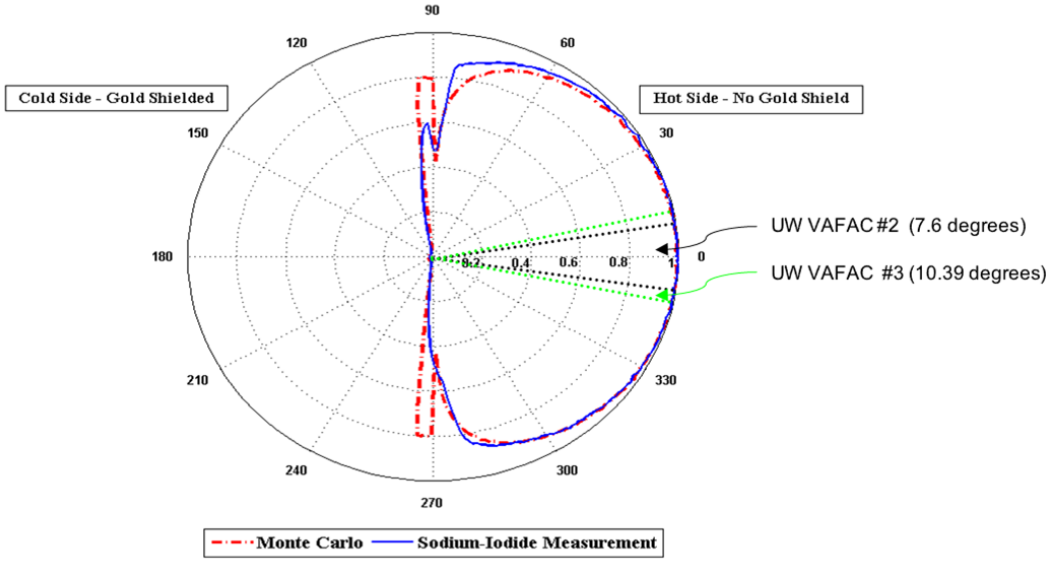

Figure 3.6: In-air fluence data from a CivaDot measured with a NaI detector is plotted in blue. The MCNP6-predicted fluence distribution is plotted in red. Notice the significant asymmetry due to the presence of the gold shield.

3.2.4 CivaDot source-specific UW VAFAC corrections factors

A number of correction factors are applied to the UW VAFAC measurements to determine S_K as seen in Equation 3.3. These corrections were calculated either analytically or with Monte Carlo techniques. The transport code MCNP6 (Goorley) with the updated photon cross-section library mcplib12 was used to model the CivaDots. The mcplib12 (Goorley) cross-section library contains updated atomic cross-sections for low-energy photons, important for this work since the presence of the gold shield results in the generation of L-shell fluorescence x rays. Previous cross-section libraries combined L-shell interactions into a single x-ray energy, so the mcplib12 cross-section library and MCNP6 Monte Carlo code is an ideal choice for this application.

The CivaDot geometry was modeled according to design information provided by CivaTech Oncology, Inc. The ^{103}Pd source spectrum used in this work was obtained from the National Nuclear Data Center online NUDAT 2.6 database. (Brookhaven National Labo-

ratory) A detailed description of the correction factors was given by Seltzer et al. and Culberson et al. (Seltzer et al. 2003, Culberson et al. 2006) For this study, the correction factors were calculated using MCNP6 following the same methodology as applied to ^{103}Pd coiled sources by Paxton et al. (Paxton et al. 2008) CivaDot correction factors are similar to conventional ^{103}Pd sources for the geometric-based and reference condition-based factors such as the corrections for decay, temperature, pressure, humidity, and ion recombination. However, the rest of the factors are dependent on the energy spectrum and were recalculated for this work. A complete MCNP6 model of the UW VAFAC was used to determine each of the correction factors that required Monte Carlo simulations. The statistical standard deviation of the simulations for all the corrections was less than 0.1% (1σ).

3.2.4.1 UW VAFAC correction factor results

The correction factors for a CivaDot using the UW VAFAC Aperture No. 3 are presented in Table 3.1. It is apparent that the corrections for attenuation between the source and the free-air chamber including k_{fil}, $k_{\text{att-el}}$, $k_{\text{att-SA}}$, $k_{\text{att-VAFAC}}$ are all different for a CivaDot than that for a pure ^{103}Pd source. This is due to the lower average energy of the emitted spectrum which includes the gold fluorescence x-rays. Specifically, the correction for the aluminum filter attenuation, k_{fil}, is 1.1404 for the CivaDot and only 1.0773 for a pure ^{103}Pd source. A larger correction in itself is not a source of additional uncertainty as long as the spectrum used for the calculation is constant and well known. To account for the potential variability in ^{103}Pd loading and the possible effects on k_{fil}, an additional uncertainty has been added, and will be detailed further in section 3.2.7.

3.2.5 CivaDot $S_{\mathbf{K}}$ measurement results

Air-kerma strength measurements determined with the UW VAFAC for a batch of four CivaDots are given in Table 3.2. Also shown are the reproducibility values (The Type A

Table 3.1: Correction factors used for UW VAFAC measurements of a CivaDot with a 30 cm source-to-aperture distance and UW aperture No. 3. Original correction factors were calculated by Culberson et al. (Culberson et al. 2006)

Correction Factor	Description	Original ^{103}Pd	CivaDot
k_{dec}	Correction to the reference date, $T_{1/2}(d)$	$T_{1/2} = 16.99\,\text{d}$	
k_{TP}	Air temperature and pressure correction	$[(273.15+T)/(273.15+T_{\text{ref}})] \cdot [P_{\text{ref}}/P]$ [a]	
k_{sat}	Ion-recombination correction	1.000	
k_{hum}	Humidity correction	0.998	
k_{stem}	Source-holder correction	1.000	1.000
k_{pen}	Aperture-penetration correction	1.000	0.999
k_{fil}	Attenuation in aluminum filter	1.077	1.140
$k_{\text{att-el}}$	Attenuation through the entrance electrode	1.002	1.003
$k_{\text{att-VAFAC}}$	Attenuation in air from the aperture to the VAFAC	1.018	1.023
$k_{\text{att-SA}}$	Attenuation in air from the source to the aperture	1.027	1.039
$k_{\text{int-sca}}$	Internal photon scatter correction	0.991	0.992
$k_{\text{ext-sca}}$	External photon scatter correction	0.991	0.993
k_{invsq}	Inverse-square correction for aperture	1.017	1.017
$\prod k_{\text{corr}}$	Product of correction factors	$1.124(k_{\text{dec}}.k_{\text{TP}})$	$1.214(k_{\text{dec}}.k_{\text{TP}})$

[a] T_{ref} =22 °C and P_{ref} =101.33 kPa

Table 3.2: Air-kerma strength results for four CivaDots from a single batch. Measurements were performed with the UW VAFAC aperture No. 3, which corresponds to a half angle of of 10.39°. The relative standard uncertainty (k=1) takes into account the repeatability as well as generalized Type A and Type B uncertainties of the VAFAC.

Source ID	UW VAFAC S_{K} (U)	Reproducibility (%)	Relative standard uncertainty (%)
1	2.28	0.23	1.80
2	2.33	0.17	1.79
3	2.29	0.08	1.79
4	2.27	0.25	1.80

component of the uncertainty analysis) for each measurement as well as the relative combined standard uncertainty. Reproducibility is defined as the standard deviation of the mean of the determined S_{K} values from each measurement. Since the source orientation was not changed between measurements, reproducibility is effectively equal to the repeatability of the measurement and is an indicator of measurement precision. The measurement precision (<0.3%) is more than acceptable for a primary measurement of LDR brachytherapy source strength since it is lower than the 0.75% stated uncertainty of the UW VAFAC with a coverage factor of k=1. (Culberson et al. 2006) In addition to individual CivaDot measurement precision, the similarity in S_{K} as shown in the second column of Table 3.2 demonstrates a consistent value of S_{K} within a batch with a deviation from the average of less than 1.5%.

3.2.6 Uncertainty

The combined (Types A and B) relative standard uncertainty associated with UW VAFAC measurements of ^{103}Pd sources is given by Culberson et al. to be $\sqrt{\sigma_{\mathrm{rep}}^2 + 0.75^2}$ where σ_{rep} is the reproducibility of the measurement. (Culberson et al. 2006) A coverage factor of 2 ($k = 2$) is then applied to this value to arrive at the relative expanded uncertainty.

Unique to this work is the uncertainty due to the variation in palladium loading within the CivaDot. This uncertainty affects the correction factors since the energy spectrum is

subject to slight variations with changes in palladium loading. To capture this uncertainty, the approach taken for this work was to calculate the correction factors for both a 20% ^{103}Pd loading and an 80% ^{103}Pd loading by mass. This corresponds to physically possible values (since there must be some amount of palladium in the region and it cannot be fully loaded), and represents a range of correction factor values that could be expected.

CivaDot spectra with 20% and 80% palladium loading were both simulated separately using MCNP6 with the UW VAFAC setup. Correction factors were then calculated for both the cases using the same methodology as applied for the calculation of correction factors shown in Table I (50% palladium loading). When all correction factors are multiplied together, a net correction factor is used to predict the variation as a function of palladium loading. The change in net correction factor between 20% and 50% loading is +2.38% and between 80% and 50% loading is −2.81%. Using a conservative approach and assuming a rectangular/uniform distribution for palladium loading with bounds of ±2.81%, the estimated Type B (Taylor and Kuyatt 1994) uncertainty associated with CivaDot S_{K} correction factors is 1.62%, and can be added in quadrature to yield a relative standard uncertainty for the UW-VAFAC with CivaDots to be $\sqrt{\sigma_{\mathrm{rep}}^2 + 0.75^2 + 1.62^2}$%. For example, if we consider the maximum value of σ_{rep} from Table 3.2, then the relative standard uncertainty for that measurement is 1.80%.

3.2.7 Discussion

The UW VAFAC was successfully used to measure the S_{K} of multiple CivaDot sources. Instead of rotating the source, the CivaDots were fixed in a PMMA holder. Precise alignment to the CivaDot origin was achieved by using a side laser and indexing from the front face of the bio-absorbable membrane with a precision translation stage. The setup is robust and minimizes scatter (compared to a solid-backed holder) by suspending the CivaDot in air at the UW VAFAC origin. The precision of the measurements performed in this work was

high, yielding low overall uncertainties for the determination of S_K. The emitted energy spectrum was measured and compared with Monte Carlo simulations. Both results show a significant presence of low-energy L-shell fluorescent x-ray radiation originating in the gold shield within the CivaDot. By using the updated photon cross-section database, individual L-shell lines were accurately predicted and simulated.

3.2.8 Comparison of different UW VAFAC apertures

Air-kerma strength measurements of three CivaDot sources were performed using two different UW VAFAC apertures (#2 and #3).

3.2.8.1 Reference Conditions

1. Batch ID: NIST 15-0267 A,B,C
2. Aperture Size: UW VAFAC Aperture #2 – 8.008 cm inner diameter, 7.6° half angle and Aperture #3 – 11.00 cm inner diameter, 10.39° half angle
3. Reference Date and Time: 9/11/2015, 10:00:00 AM
4. Holder Type: PMMA window style (no backscatter), no rotation.

3.2.8.2 Results

Tables 3.3, 3.4 and 3.5 present the results of the CivaDot S_K determined with the three aperture and filter configurations.

The table 3.6 summarizes the ratio of average measured corrected reading (M_c) observed (not corrected for source specific correction factors) and Monte Carlo predicted ratio of source specific correction factors for the three different UW VAFAC measurement setups. When comparing two aperture configurations, the following equations should hold:

$$(S_K)_{Setup1} = (S_K)_{Setup2}$$

Table 3.3: S_K determined for three CivaDot sources using UW VAFAC aperture #2 with the aluminum filter in place. The relative standard uncertainty (u) is provided (k=1).

Aperture #2 (with Al filter)				
Source ID #	No. of Measurements #	Average S_K (U)	Reproducibility (%)	u (%)
A	4	2.19	0.33	1.82
B	4	2.21	0.14	1.80
C	4	2.15	0.32	1.82

Table 3.4: S_K determined for three CivaDot sources using UW VAFAC aperture #3 with the aluminum filter in place. The relative standard uncertainty (u) is provided (k=1).

Aperture #3 (with Al filter)				
Source ID #	No. of Measurements #	Average S_K (U)	Reproducibility (%)	u (%)
A	6	2.21	0.14	1.79
B	6	2.21	0.36	1.82
C	6	2.15	0.39	1.83

Table 3.5: S_K determined for three CivaDot sources using UW VAFAC aperture #3 without the aluminum filter in place. The relative standard uncertainty (u) is provided (k=1).

Aperture #3 (without Al filter)				
Source ID #	No. of Measurements #	Average S_K (U)	Reproducibility (%)	u (%)
A	6	2.19	0.26	1.05
B	6	2.19	0.38	1.08
C	6	2.14	0.28	1.05

$\Longrightarrow (M_c \cdot k_{\text{CivaDot-MC}})_{\text{Setup1}} = (M_c \cdot k_{\text{CivaDot-MC}})_{\text{Setup2}}$

$\Longrightarrow \frac{(M_c)_{\text{Setup1}}}{(M_c)_{\text{Setup2}}} = \frac{(k_{\text{CivaDot-MC}})_{\text{Setup2}}}{(k_{CivaDot-MC})_{\text{Setup1}}}$ where (S_{K} is the air-kerma strength, M is the free-air chamber reading not corrected for source-specific correction factors, and $k_{\text{CivaDot-MC}}$ is the product of source-specific correction factors for a free-air chamber when using the CivaDot source.

The comparison of the measured ratios to the Monte Carlo predicted ratios is shown in column 5 of table 3.6. The differences between the measured and the calculated ratios of the inter-comparison between the different setups are within the uncertainties. This provides an indication of the goodness of the Monte Carlo simulations and the associated correction factors calculated for the CivaDot.

3.3 UW VAFAC and NIST WAFAC – CivaDot primary S_{K} measurement inter-comparison

3.3.1 Introduction

When a brachytherapy source is used for patient treatment, a national source strength standard must be established for clinical use. An investigation was conducted to assist in the establishment of the primary source strength standard for the CivaDot. An inter-comparison of the CivaDot primary S_{K} determination was performed using two free-air chambers for eight CivaDot sources. The free-air chambers used in this study were the UW VAFAC, and the NIST WAFAC. This inter-comparison provides us with an estimation of the repeatability and reproducibility of the CivaDot S_{K} measurements with two different measurement devices. The UW VAFAC has five interchangeable brass aperture sizes. This investigation used the UW VAFAC Aperture No. 2 which collimates the radiation emitted from the source into a cone with a half angle of 7.6°. The aperture has the same collimating

Table 3.6: Comparison of S_K determined for three CivaDot sources using the different UW VAFAC aperture and filter configurations.

Comparison	Average measured corrected reading ratio	σ (%)	MCNP6 predicted ratio	σ (%)	Difference (%)
Aperture #2 (with Al filter) and Aperture #3 (with Al filter)	0.9904	0.24	0.9888	0.01	-0.16 ± 0.24
Aperture #2 (with Al filter) and Aperture #3 (no Al filter)	1.1093	0.27	1.1165	0.97	0.65 ± 1.00
Aperture #3 (with Al filter) and Aperture #3 (no Al filter)	1.1200	0.23	1.1291	0.96	0.81 ± 0.98

solid angle as the NIST WAFAC aperture. Both free-air chamber measurements were performed with the CivaDot held in a static holder and the source cylindrical axis transverse to the aperture plane (hot side of the source facing the primary aperture).

3.3.1.1 CivaDot energy spectrum comparison

The presence of a gold shield (in close proximity to the radioactive part of the source) alters the energy spectrum of the CivaDot in comparison to conventional LDR ^{103}Pd brachytherapy sources as seen in previous sections of this chapter. For the purpose of S_K determination, NIST measures the source energy spectrum using a high-purity germanium detector with appropriate detector response correction factors. This measured spectrum was compared to UW calculated CivaDot energy spectrum using MCNP6 simulations assuming a palladium loading of 50%. Since the Monte Carlo resolution is higher than the detector resolution, the MC predicted spectrum was consolidated into energy bins corresponding to the NIST measured spectrum. A comparison of the spectra was performed and the presence of the gold fluorescence was investigated.

3.3.1.2 CivaDot source-specific correction factors for free-air chamber measurements

The CivaDot source-specific correction factors were also compared for the two free-air chambers. A detailed description of the correction factors that need to be determined for the free-air chambers was given by Seltzer et al. and Culberson et al. (Seltzer et al. 2003, Culberson et al. 2006) NIST determines the correction factors for the WAFAC using a combination of empirical, analytical and MC methods as described by Seltzer et al. (Seltzer et al. 2003) For the UW VAFAC, the correction factors were calculated for Aperture No. 2 using Monte Carlo methods (MCNP6 code) as outlined by Culberson et al. and Aima et al. (Culberson et al. 2006, Aima et al. 2015) Though these are two different free-air chambers,

the comparison provides a good accuracy check for the corrections as the methods used are completely different and are both sensitive to low-energy gold fluorescence observed in the CivaDot energy spectrum.

3.3.1.3 Primary S_K measurements performed without the presence of an aluminum filter

The use of an aluminum filter when performing a primary S_K measurement was recommended by the TG-43 report (Rivard et al. 2004) to exclude the titanium fluorescence present in conventional LDR sources. However, the CivaDot does not contain a titanium encapsulation and the magnitude of the correction for the aluminum filter attenuation, k_{foil}, is sensitive to the the low-energy photons which includes the fluorescence observed from the gold shield. An additional investigation was performed with the UW VAFAC to study the impact of the aluminum filter on the CivaDot S_K determination. The aluminum filter was removed from the UW VAFAC, and CivaDot S_K measurements were performed. These measurements were compared to NIST-determined S_K values for the same sources using the WAFAC with the presence of an aluminum filter.

3.3.2 Inter-comparison results

3.3.2.1 CivaDot energy spectrum comparison

Table 3.7 shows the results of the comparison of the CivaDot measured energy spectrum as provided by NIST using a HPGe detector to the energy spectrum calculated for this investigation using MCNP6 simulations of the CivaDot. The measured and the predicted spectrum were normalized to the net counts, yielding relative intensities. Three additional photopeaks were observed in both the measured and the predicted CivaDot energy spectrum when compared to a conventional ^{103}Pd seed spectrum. These spectral peaks (9.7 keV, 11.4 keV, 11.7 keV) correspond to the gold shield fluorescence observed in the source spectrum.

All seven photo-peaks for the measured and the predicted spectra agreed to within 1.8%. Good agreement was observed in the spectral comparison ($\leq$1.8%), especially considering the fact the Monte Carlo simulations assume a fixed palladium loading. This comparison also validates previous findings published by Aima et al. (Aima et al. 2015) Gold fluorescence was observed in both the spectra which contributes significantly to the S_{K} measurement of a CivaDot.

3.3.2.2 UW VAFAC correction factors

Source-specific correction factors for the CivaDot measurement using the UW VAFAC Aperture No. 2 were calculated for this investigation. These factors were calculated using Monte Carlo as outlined in previous publications. (Culberson et al. 2006, Paxton et al. 2008, Aima et al. 2015) NIST determined the source-specific correction factors for the WAFAC CivaDot measurements by applying a combination of empirical, analytical and MC methods as outlined by Seltzer et al. (Seltzer et al. 2003) Table 3.8 provides the results of the comparison. The free-air chamber source-specific correction factors for the CivaDot for the two instruments were comparable. The CivaDot net correction factor for the two free-air chambers using the two methods was in good agreement (0.7%) as seen in Table 3.8, considering the fact that these are two different free-air chambers. It is also a validation of determining the correction factors using two distinct methodologies. NIST utilizes a combination of empirical, analytical and MC methods approach whereas UW calculates the factors using Monte Carlo methods.

3.3.2.3 CivaDot S_{K} measurements

The CivaDot S_{K} determined for eight sources using the two free-air chambers was compared, as shown in Table 3.9. The S_{K} measured using the UW VAFAC was within 1.1% of the NIST WAFAC values for all eight CivaDot sources with comparable uncertainties, and an

Table 3.7: A comparative analysis of the CivaDot energy spectrum measured by NIST using a HPGe detector and the spectrum calculated using MCNP6 Monte Carlo simulations for this investigation.

Spectral Peak	Energy	NIST-Measured Spectrum Relative Intensity	UW-MCNP6 Predicted Spectrum Relative Intensity	Difference
	(keV)	(%)	(%)	(%)
Au L_α	9.7	2.05%	1.67%	0.4%
Au L_β	11.4	1.91%	1.44%	0.5%
Au L_β	11.7	0.59%	0.50%	0.1%
Rh K_α	20.1	78.92%	80.73%	-1.8%
Rh K_β	22.7	13.93%	13.22%	0.7%
Rh K_β	23.1	2.50%	2.09%	0.4%
γ	39.7	0.09%	0.09%	0.0%

Table 3.8: Source-specific correction factors determined for UW VAFAC aperture No. 2 measurements of a CivaDot using MC simulations and NIST WAFAC using a combination of empirical, analytical and MC methods methods.

Source-Specific Correction Factor	Description	NIST WAFAC CivaDot	UW VAFAC CivaDot
k_{sat}	Ion-recombination correction	1.000	1.000
k_{hum}	Humidity correction	0.997	0.998
k_{stem}	Source-holder correction	1.000	1.000
k_{pen}	Aperture-penetration correction	1.000	0.999
k_{foil}	Attenuation in aluminum filter	1.149	1.140
$k_{\text{att-el}}$	Attenuation through the entrance electrode	1.000	1.003
$k_{\text{att-FAC}}$	Attenuation in air from the aperture to the FAC	1.013	1.018
$k_{\text{att-SA}}$	Attenuation in air from the source to the aperture	1.041	1.038
$k_{\text{int-sca}}$	Internal photon scatter correction	0.996	0.992
$k_{\text{ext-sca}}$	External photon scatter correction	0.995	0.991
k_{invsq}	Inverse-square correction for aperture	1.009	1.009
$\prod k_{\text{corr}}$	Product of correction factors	1.209	1.200

average difference of 0.3%. These results illustrate the good repeatability of the UW VAFAC and NIST WAFAC results and comparable reproducibility of the UW VAFAC measurement to the U.S. national standard.

3.3.2.4 Impact of the aluminum filter on the CivaDot S_K measurements

It is apparent that the aluminum filter correction (about 15%) is the largest contributor to the overall correction to the free-air chamber measurements for both instruments. The aluminum filter attenuates the gold fluorescence present in the CivaDot energy spectrum considerably for both free-air chambers. The use of an aluminum filter for S_K measurement was recommended by the TG-43 report (Rivard et al. 2004) for the exclusion of titanium fluorescence present in conventional LDR sources. However, the CivaDot does not contain a titanium encapsulation and the correction for the aluminum filter attenuation, k_{foil}, is about 1.14 to 1.15 for the CivaDot compared to about 1.08 for a conventional ^{103}Pd brachytherapy source. Although a larger correction does not lead to inaccurate results, the UW VAFAC uncertainty for the measurements takes into account the palladium loading impact (source self-shielding). The intensity of the gold fluorescence changes with the amount of palladium loading. This impacts the k_{foil} factor and once the aluminum filter is removed, this source of uncertainty is mitigated.

The impact of the aluminum filter on the UW VAFAC determined CivaDot S_K is shown in Table 3.10. The CivaDot S_K determined using the UW VAFAC without the aluminum filter when compared to WAFAC determined values with the presence of an aluminum filter resulted in an agreement to within 0.5% for all three sources measured. There was a noticeable difference in the uncertainty associated with the measurements. The UW VAFAC uncertainty reduced from 1.8% to 1.1% as the effect of palladium loading on correction factor uncertainty diminishes.

Table 3.9: The air-kerma strength inter-comparison results for eights CivaDots using NIST WAFAC and UW VAFAC. The standard uncertainty ('u') for the UW VAFAC was calculated as outlined by Aima et al., and for the NIST WAFAC by Seltzer et al. (Aima et al. 2015, Seltzer et al. 2003)

NIST Source ID #	UW VAFAC S_K (U)	u (%)	NIST WAFAC S_K (U)	u (%)	Difference (%)
005 A	5.27	1.82	5.27	1.74	-0.1%
005 B	5.30	1.80	5.28	1.78	0.4%
005 C	5.17	1.82	5.16	1.79	0.2%
CSH-010-1	4.22	1.80	4.20	1.69	0.4%
CSH-010-5	4.21	1.82	4.16	1.76	1.1%
CSH-010-7	4.21	1.79	4.20	1.80	0.3%
CSH-010-13	4.13	1.80	4.13	1.75	0.0%
CSH-010-14	4.16	1.80	4.15	1.86	0.2%

Table 3.10: A comparison of the air-kerma strength of three CivaDots determined using the NIST WAFAC with the aluminum filter and the UW VAFAC without the aluminum filter. The relative standard uncertainty (u) is provided (k=1).

NIST Source ID #	UW VAFAC without Al filter S_K (U)	u (%)	NIST WAFAC with Al filter S_K (U)	u (%)	Difference (%)
005 A	5.25	1.05	5.27	1.74	-0.5%
005 B	5.26	1.08	5.28	1.78	-0.5%
005 C	5.14	1.05	5.16	1.79	-0.5%

3.4 Clinical transfer of primary CivaDot $S_{\mathbf{K}}$ measurement

Air-kerma strength is typically measured by clinical users via a well-type ionization chamber with a calibration coefficient from an Accredited Dosimtery Calibration Laboratory (ADCL). These chambers are cylindrically symmetric and hold the source along the cylindrical axis during a measurement. With a directional source such as a CivaDot, the transfer of any source strength metric requires a feasibility investigation. This section details the various measurements performed to evaluate the appropriateness of the transfer of the primary air-kerma strength measurements of the CivaDot to a well-type ionization chamber.

3.4.1 Well-type ionization chamber setup

A Standard Imaging, Inc. (Middleton, WI) HDR1000 Plus well-type ionization chamber was used for measuring CivaDot sources. Figure 3.7 is an image of the instrument used. When measuring a source, a well chamber should have a uniform response regardless of source orientation. To verify this, a custom source holder was manufactured in collaboration with Standard Imaging, Inc. (Middleton, WI) to hold a single CivaDot.

A hinged polymethyl methacrylate (PMMA) frame-style holder was designed to suspend the CivaDot in air along the cylindrical axis of a well chamber at the axial point of maximum response. The frame is snapped shut to hold the CivaDot by securing the bio-absorbable membrane at the ends. The insert was designed to fit in a commercially-available Standard Imaging HDR1000 Plus well-type ionization chamber. To test the response of the system, a series of measurements were made with different source holder rotations and compared to a measurement at a reference position. A schematic of the custom designed source holder is shown in Figure 3.8.

Figure 3.7: An image of the HDR1000 Plus well chamber manufactured by Standard Imaging. [Image reproduced from: https://www.standardimaging.com/]

3.4.2 Well-type ionization chamber system symmetry

Measurements of ionization current were performed with the custom-made CivaDot holder inside a Standard Imaging HDR1000 Plus well-type ionization chamber at four cardinal rotational angles. Ideally, the well chambers are cylindrically symmetric and should provide a uniform response regardless of the source orientation. Variations in the well chamber angular response can be due to either the well chamber or the source holder asymmetry. To test the chamber angular response, multiple measurements were performed with the source holder at the four cardinal angles within the well chamber.

The results of the well-type ionization chamber measurements of four CivaDot sources using a HDR1000 Plus chamber (A011927) are plotted in Figure 3.9. A variation in response of the chamber of <1.5% for all four sources in the batch at all four cardinal angles was observed. The results were normalized to an average of the four readings (excluding the first) for each CivaDot and indexed with a permanent mark on the holder and chamber.

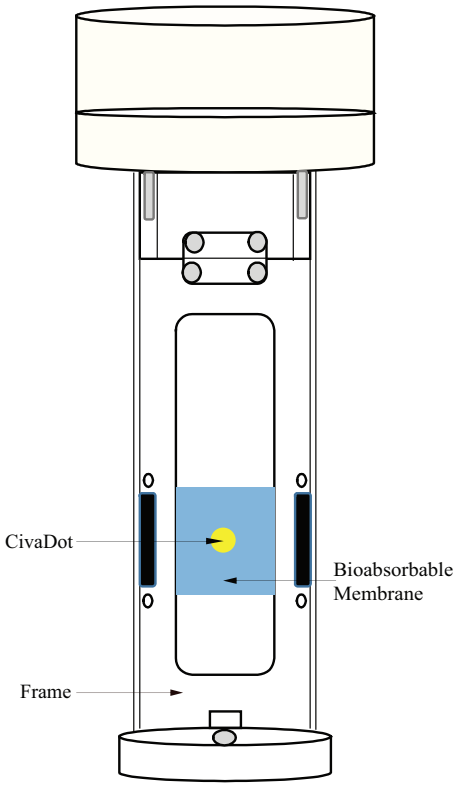

Figure 3.8: Diagram of the CivaDot holder for use with a Standard Imaging HDR1000 Plus well-type ionization chamber. The CivaDot is shown in yellow and is held by securing the surrounding bio-absorbable membrane (blue) in a hinged frame holder. Please note that the illustration is not to scale.

The results indicate that the chamber and holder system exhibit a variation in response with angle consistent from CivaDot to CivaDot within a batch, indicating a small amount of cylindrical asymmetry. This variation could be from the chamber or the source holder. For implementation of the well chamber as the presumed best method to disseminate S_K to clinical users, an average of readings at multiple holder rotations should be used to avoid introducing a systematic bias at a single angle. Even if the source of asymmetry were to be identified and remedied, making four measurements at the cardinal angles is a reasonable expectation for any Accredited Dosimetry Calibration Laboratory (ADCL) or clinical user.

Figure 3.10 shows the variation of the well chamber response for two CivaDot normalized to the average as a function of source holder orientation for two different vintages of the HDR1000 Plus well chamber (A080852 – 2008 and A011927 – 2001). The results of the A011927 presented in this figure are consistent with the results presented in Figure 3.9, with variation of <1.5% for both sources. The variation for the A080852 well chamber is much less (<0.5%) for both sources, which may be attributed to a design change by the manufacturer from 2001 to 2008 vintage of the instrument leading to more uniform response for the 2008 vintage.

3.4.3 Well chamber calibration coefficient consistency

In addition to the variation in response with angle, the ratio of S_K to well-chamber ionization current, S_K/I (also known as the well chamber calibration coefficient, N_{S_K}) was investigated. This coefficient was determined for several batches of CivaDots using primary S_K values determined with the UW VAFAC and the well chamber ionization current reading over multiple years. The individual S_K/I for a given CivaDot source was compared to the overall mean for the given well chamber. For an S_K calibration to effectively be transferred to a well-type ionization chamber, the S_K/I should remain consistent from source to source as expected for traditional LDR brachytherapy sources.

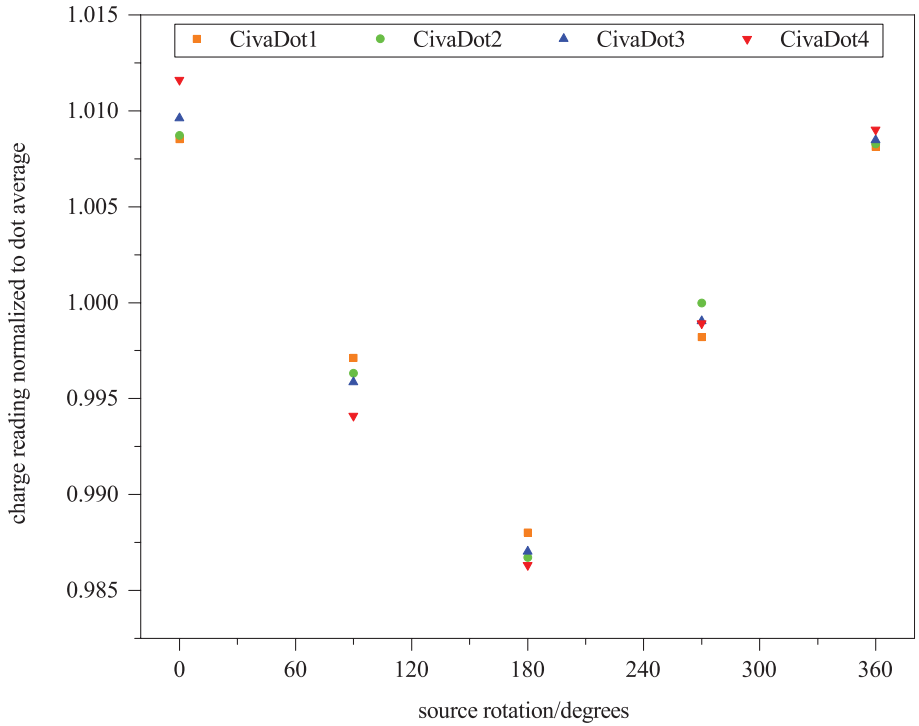

Figure 3.9: Results of the change in ionization current with a CivaDot secured in a custom holder within a Standard Imaging HDR1000 Plus well-type ionization chamber (A011927) as a function of angle. The values for a given CivaDot are normalized to the average of the five readings for each CivaDot. The fifth reading was acquired at the initial zero degree orientation to evaluate repeatability.

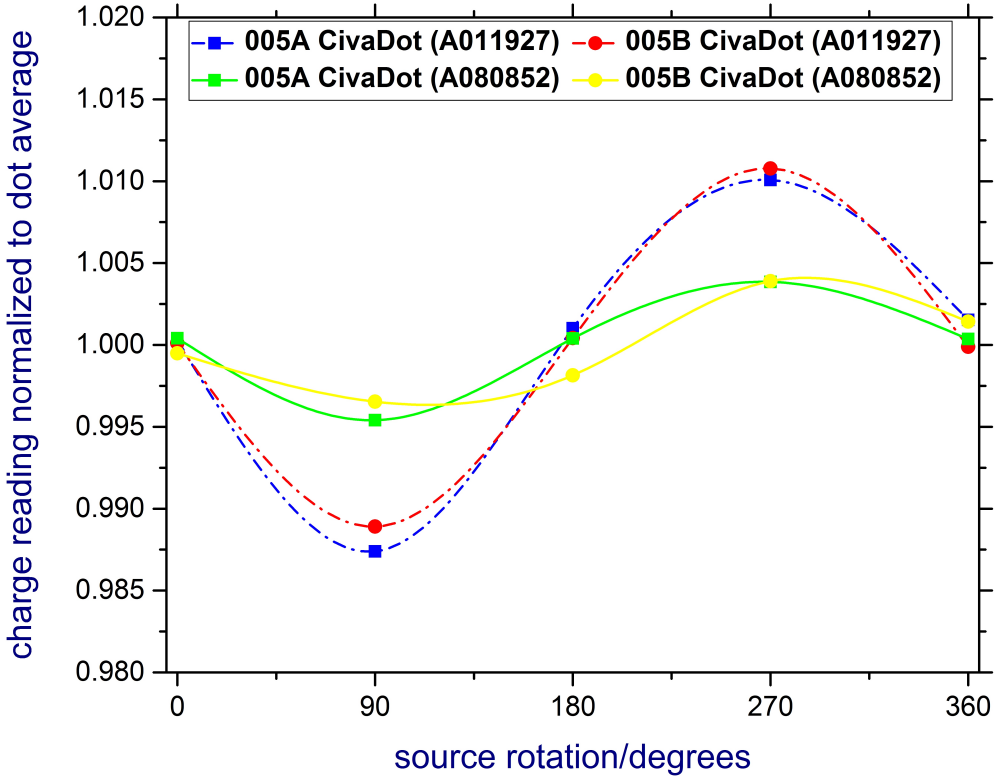

Figure 3.10: The CivaDot charge readings measured with two Standard Imaging HDR1000 Plus well-type ionization chambers (2001 and 2008 vintages) as a function of well chamber cardinal angles. The charge readings have been normalized to the overall average for the source.

The results of consistency of the calibration coefficient using two different HDR1000 Plus models (vintage 2001 and 2008) is shown in Table 3.11, including the difference of a given calibration coefficient from the average calibration coefficient for that well chamber. All CivaDot S_K values used for this table were determined by performing measurements with the UW VAFAC. For all eighteen sources measured over a period of one year, the maximum difference observed was 2.6% with most sources within 1.5%. This demonstrates sufficiently low variation for the eventual transfer of S_K to a clinical user, given the overall uncertainty (k= 2) reported by the UWADCL for calibrations of conventional seeds using the HDR1000 Plus well chamber is about 2.4%. The value of the CivaDot well chamber calibration coefficient was determined to be 0.78±0.02 U/pA for the HDR1000 Plus well chambers used for this work.

3.4.4 CivaDot altitude correction factor

When a photon-emitting low-energy brachytherapy source like the CivaDot is measured with an air-communicating well chamber like the HDR1000 Plus, a correction factor for the air density has to applied to the measurement to correct it back to reference conditions. Griffin et al. provided the empirical form for this correction factor and the associated coefficients for conventional Pd-103 seeds based on measurements. (Griffin et al. 2005) Since the CivaDot energy spectrum is significantly different than a conventional Pd-103 source, a Monte Carlo investigation was performed to test the applicability of these coefficients for a CivaDot. The CivaDot model geometry was simulated in a Monte Carlo model of the HDR1000 Plus based on the specifications provided by Standard Imaging Inc. Two sets of simulations were performed using MCNP6 code, one with the normal CivaDot source and the other with no gold shield present in the CivaDot model. For each set, the air density was varied to mimic air pressure variations between 540 and 760 torr. Without the gold shield, a fair comparison between the altitude correction factor calculated for Pd-103 seeds using

Batch	Source ID (#)	HDR1000 Plus (A011927) Calibration Coefficient Difference from Average (%)	HDR1000 Plus (A080852) Calibration Coefficient Difference from Average (%)
Dec-14	CSH-1214-01	0.5%	-
	CSH-1214-02	2.0%	-
	CSH-1214-03	1.1%	-
	CSH-1214-04	-1.0%	-
Sep-15	005 A	-1.0%	-0.8%
	005 B	0.6%	0.8%
	005 C	-2.6%	-2.4%
Dec-15	CSH-010-1	-0.1%	0.2%
	CSH-010-5	1.0%	0.9%
	CSH-010-7	0.3%	0.3%
	CSH-010-13	-0.7%	-0.5%
	CSH-010-14	-0.3%	-0.5%
Dec-15	CSH-1215-01	1.9%	2.2%
	CSH-1215-02	-0.9%	-0.4%
	CSH-1215-03	0.0%	0.8%
	CSH-1215-04	-2.5%	-2.4%
	CSH-1215-05	1.6%	1.6%

Figure 3.11: Results of the consistency of the well chamber calibration coefficient for two HDR1000 Plus chambers measured over several CivaDot batches.

Griffin et al.'s method and the altitude correction factor calculated using Monte Carlo can be performed. As seen in Table 3.11, the difference between the altitude correction factors calculated for the Pd-103 seeds and CivaDot – No Gold Shield configuration was within 2.5%, which is on the order of the overall uncertainty for LDR well chamber measurements of the UW ADCL (about 3%). More importantly, the difference in the altitude correction factor between the CivaDot – No Gold Shield and CivaDot – Gold Shield is within 0.2%, which implies that the spectral effects of the gold shield don't have an effect on the altitude correction factor determination for the CivaDot source.

3.4.5 UW ADCL suggested measurement protocol

In collaboration with the UW ADCL and CivaTech Oncology, a well chamber measurement protocol for clinical users was developed for the CivaDot measurements performed using the custom source holder with the HDR1000 Plus well chamber. Instructions were listed as follows:

1. Assemble the correct equipment required to perform measurements of the CivaDot source. See notes below

2. Obtain the calibration coefficients from the instrument calibration reports from the ADCL.

3. Follow the directions for using the LDR well chamber and electrometer system to ensure they are powered on and properly equilibrated. (Please see note about acceptable LDR measurement systems.)

4. Place CivaDot Calibration Source in the specially designed source holder with the gold marker facing away from the hinged cover. The purple radioactive side of the CivaDot will be facing towards the hinged cover.

Table 3.11: Results of the altitude correction factor determined for Pd-103 conventional seeds using Griffin et al. (Griffin et al. 2005), CivaDot source with no gold shield present, CivaDot source with the gold shield present.

Pressure (torr)	^{103}Pd - Griffin et al. (Griffin et al. 2005) ACF	CivaDot No Gold MCNP6 ACF	Difference–Pd and CivaDot No Gold (%)	CivaDot Gold MCNP6 ACF	Difference–CivaDot Gold and CivaDot No Gold (%)
540	0.827	0.849	-2.5%	0.850	0.2%
570	0.853	0.871	-2.0%	0.872	0.2%
600	0.878	0.892	-1.6%	0.894	0.2%
630	0.902	0.913	-1.2%	0.914	0.2%
660	0.926	0.933	-0.8%	0.935	0.2%
690	0.949	0.953	-0.4%	0.954	0.2%
720	0.972	0.972	0.0%	0.974	0.1%
760	1.002	0.997	0.5%	0.999	0.1%

5. Place the source holder containing the sample into the well chamber and align the black line on the top of the source holder with the dot on the top of the well chamber. This will be considered the index location for the measurement protocol described below.

6. After the ionization current has stabilized, collect a 30-second charge measurement using the built-in timer on the electrometer.

7. Rotate the source holder clockwise 90 degrees, wait for the current to stabilize (approximately 5 to 10 seconds), and repeat the measurement.

8. Repeat step 5 for each of the 4 cardinal directions, repeating the initial measurement at the end. A total of 5 30-second charge measurements should be collected.

9. Average the the last four measurements (to avoid including additional bias from both initial and final index measurements) to determine the average collected charge over the 4 cardinal directions.

10. Correct these measurements as appropriate for temperature, pressure, altitude, and geometric influences. Please refer to the Appendix included with your ADCL report for proper use of the calibration coefficient.

3.4.5.1 Notes about acceptable systems

The electrometer used to make these measurements must be compatible with low dose rate (LDR) sources. The dynamic range of the measurement scale must be able to detect pA current levels. Some high dose rate (HDR) and external beam electrometers designed for higher signal strength may not be suitable for measuring LDR sources. It has been noted that sources less than 1 U/CivaDot have low signal to noise ratios and may have higher variability in measurements. The source holder should place CivaDot calibration sources at the optimal position within the well chamber to make these measurements. It

is very important to note the the CivaDot source holder is serialized, and specific to the well chamber it was calibrated with at the ADCL. Modification of this holder or use of any other fixture to position the CivaDot during measurement will invalidate the calibration and traceability to NIST air kerma strength standards. At this time, NIST traceable calibrations are provided for Standard Imaging HDR1000 Plus well chambers only. Due to the presence of the gold shield, the CivaDot yields a lower ionization current reading in a well chamber than an unshielded conventional LDR source of the same source strength.

3.5 Cropped CivaDot sources

In September 2016, three CivaDots were investigated with less bio-absorbable membrane around the diagonal of the CivaDot source. This investigated was focused on studying the impact of the bio-absorbable membrane length in CivaDots which are being used for assaying/clinical verification. Primary air-kerma strength measurements of all three cropped CivaDot sources were performed with the UW VAFAC. Measurements of the sources were also performed using the UWADCL NIST-traceable Standard Imaging HDR1000 Plus well-type ionization chamber (A080852) in two orientations, by placing the source on the right and the left diagonal of the source holder with the CivaDot hot side facing the hinged cover of the holder. Ionization current readings were acquired at the four cardinal angles of the well chamber for both orientations. S_{K} was determined for the three sources using the well chamber calibration coefficient.

Table 3.12 presents the results of the S_{K} determined for the three sources using the UW VAFAC compared to the standard well chamber determined value with the NIST-traceable calibration coefficient. Table 3.12 Column 2 and 3 show the difference of a given orientation from the average of the two. These differences are less than 0.2% which demonstrates good positioning repeatability. Table 3.12 Column 4 presents the observed difference of the UW VAFAC determined air-kerma strength value from the standard well chamber value. All

Table 3.12: Results of the comparison of the UW VAFAC and well chamber determined air-kerma strengths for the cropped CivaDot sources.

Source ID #	WC Lt Diagonal Diff from Av. (%)	WC Rt Diagonal Diff from Av. (%)	UW VAFAC S_K Diff from WC (%)	UW VAFAC uncertainty (%)
CSH-032-1	0.1	-0.1	3.7	1.9
CSH-032-2	-0.1	0.1	2.2	1.8
CSH-032-3	-0.1	0.1	3.6	1.8

three sources had lower measurement results using the well chamber when compared to the VAFAC. Measurements of CivaDots over several batches have generally resulted in an agreement of the well chamber determined air-kerma strength to the UW VAFAC value to less than 4%.

An additional investigation of the cropped CivaDot source anisotropy was performed in air with a sodium-iodide detector. Figure 3.12 presents the results of the measured anisotropy distribution of a cropped CivaDot source compared to two normal CivaDot sources measured earlier with the complete bio-absorbable membrane present. All three distributions looked similar.

Table 3.13 presents the results of the average integrated detector counts for the in-air anisotropy for the measured cropped CivaDot source anisotropy distribution compared to two other CivaDot sources with the complete bio-absorbable membrane present. A small difference is observed between the weighted integrated detector count value for the cropped source as compared to the other two sources, which is within the expected uncertainty. A Monte Carlo simulation of the cropped CivaDot source and a normal CivaDot source was performed. The difference in the average integrated anisotropy distribution of the two sources was calculated to be 0.5%.

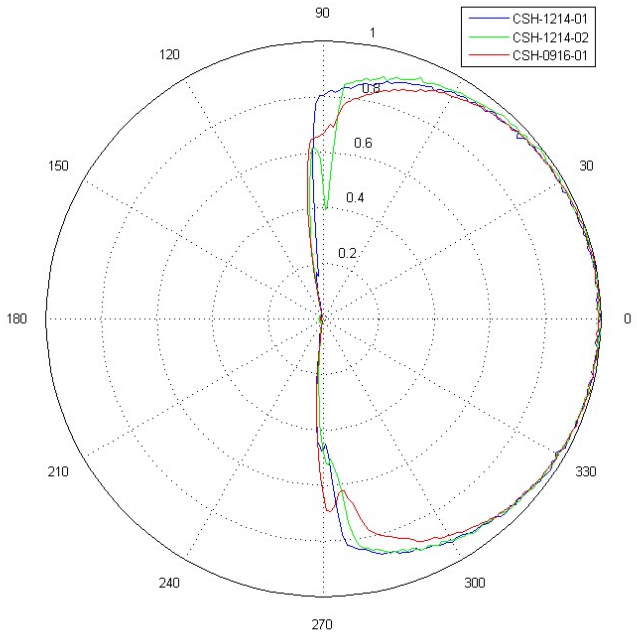

Figure 3.12: In-air anisotropy measurement of the cropped CivaDot (in red, CSH-0916-01) using a sodium-iodide detector compared to two previously measured CivaDot sources with the complete bio-absorbable membrane (in blue and green, CSH-1214-01,02) present.

Table 3.13: Comparison of the average integrated detector counts for the in-air anisotropy for the measured cropped CivaDot source anisotropy distribution to two other CivaDot sources with the complete bio-absorbable membrane present.

Source ID #	Weighted Integrated NaI Counts	Difference (%))
CSH-1214-01	0.4949	1.3%
CSH-1214-02	0.4921	0.7%
Cropped Source CSH-0916-01	0.4885	–

3.6 An investigation of the CivaDot variability

In February 2016, a CivaDot source (Feb 2016 – CSH-011) was calibrated using a NIST-traceable well chamber. The CivaDot source was measured initially in the HDR1000 Plus well chamber (A080852). The CivaDot S_K was determined using the well chamber calibration coefficient for the chamber. A primary S_K measurement of this source was performed using the UW VAFAC for comparison. The well chamber calibration coefficient was found to be -9.7% different than the average coefficient of the previous 13 CivaDot sources measured in this well chamber.

To ascertain the cause of this discrepancy and to explore a method for CivaDot consistency verification, an investigation was performed. The anisotropy distribution of the CivaDot source was measured in-air using a sodium-iodide scintillation detector. Figure 3.13 shows the results of the measured anisotropy distribution of the CivaDot, and a comparison to two other CivaDot sources (calibration coefficient within uncertainty from batch average) whose anisotropy distributions were measured earlier in 2014.

Table 3.14 shows the results of the calculated weighted sum of the measured anisotropy distributions of individual CivaDot sources measured using the sodium-iodide detector previously in December 2014, and a comparison with the Feb 2016 – CSH-011 source. The weighted sum of the Feb 2016 – CSH-011 source is clearly greater than the other two CivaDot sources. The anisotropy distribution of the Feb 2016 – CSH-011 CivaDot as reported in Figure 3.13 reflects this difference, as there is increased leakage present on the cold side of the source for this source compared to the other two CivaDot sources.

A Monte Carlo study was performed to investigate a potential reason for the difference in the anisotropy distribution measured for this source compared to the other two CivaDot sources. The anisotropy distribution of a normal CivaDot was compared to a CivaDot with the gold shield shifted 100 micro-meter upstream on the cold side of the source. The results

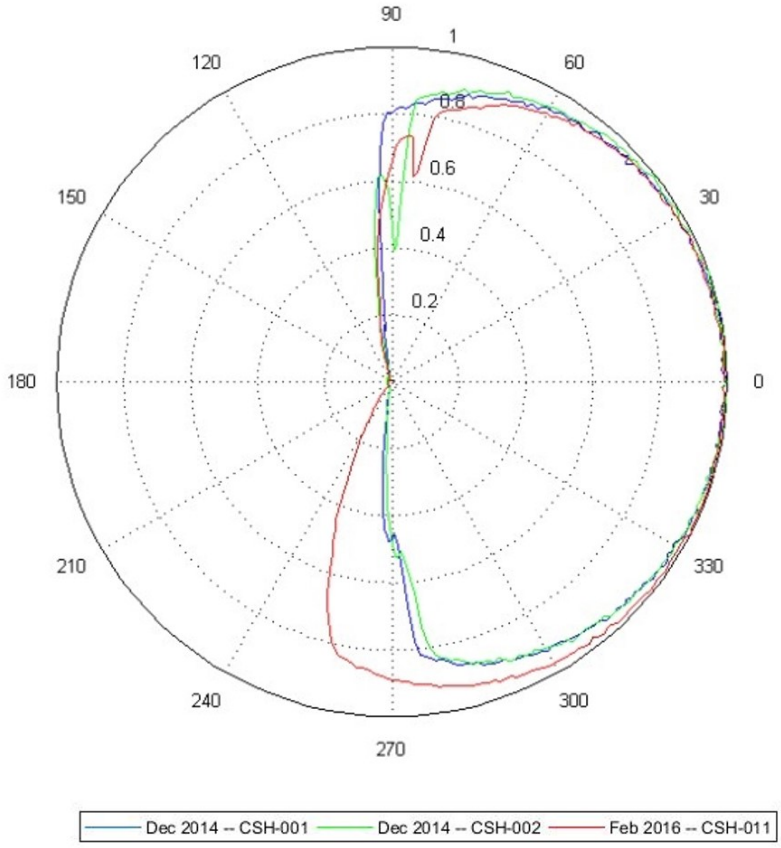

Figure 3.13: Anisotropy of two CivaDot sources measured in December 2014 compared to the CivaDot source measured in February 2016. All measurements were performed in air at 95 cm using a sodium-iodide detector. All plotted values have been normalized to the maximum value in their dataset.

Table 3.14: Comparison of the weighted sum of the CivaDot measured anisotropy distribution of a few previous CivaDot sources and Feb 2016 – CSH-011 CivaDot source

Source ID #	Weighted Integrated NaI Counts	Difference from Source 1 (%)
Sep 2014 – CSH-001	0.501	–
Sep 2014 – CSH-002	0.502	0.3%
Dec 2014 – CSH-001	0.495	-1.1%
Dec 2014 – CSH-002	0.492	-1.7%
Feb 2016 – CSH-011	0.548	9.4%

Table 3.15: MCNP6 simulated anisotropy distribution comparison of a normal CivaDot and a CivaDot with the gold shield shifted 100 microns upstream on the cold side of the source.

Source #	CivaDot Monte Carlo simulations Weighted Sum	Difference (%)
CivaDot - Normal	0.474	–
CivaDot – Gold Shield shifted 100 microns (upstream cold side)	0.500	5.61%

of this comparison are presented in Figure 3.14. There is increased leakage on the cold side of the source as seen in the figure, due to the shift in the gold shield.

Table 3.15 shows the results of the calculated weighted sum of the MC predicted anisotropy distributions of a normal CivaDot source and a CivaDot source with the gold shield shifted 100 micro-meter upstream on the cold side of the source. The 100 micro-meter gold shield shift causes the weighted sum to increase when compared to a normal source. This was attributed as a probable reason for the variability of the Feb 2016 – CSH-011 CivaDot source.

Based on the results of this investigation, CivaTech initiated a quality assurance mechanism for assessing the appropriateness of the gold shield placement within the CivaDot. CivaTech performed a scan of the gold shield shielded side of the CivaDots in a CivaSheet using a digital radiograph and assessed whether the gold shield placement is within tolerance. Figure 3.15 presents the digital radiograph of a CivaSheet scanned by CivaTech. CivaDots 10, 11 and 18 in this figure have the inappropriate gold placement as seen in this investigation. There can be additional gold shielding misplacement problems such as gold shielding that is not centered properly or shielding that is not flat. This can be detected with the use of the digital radiograph.

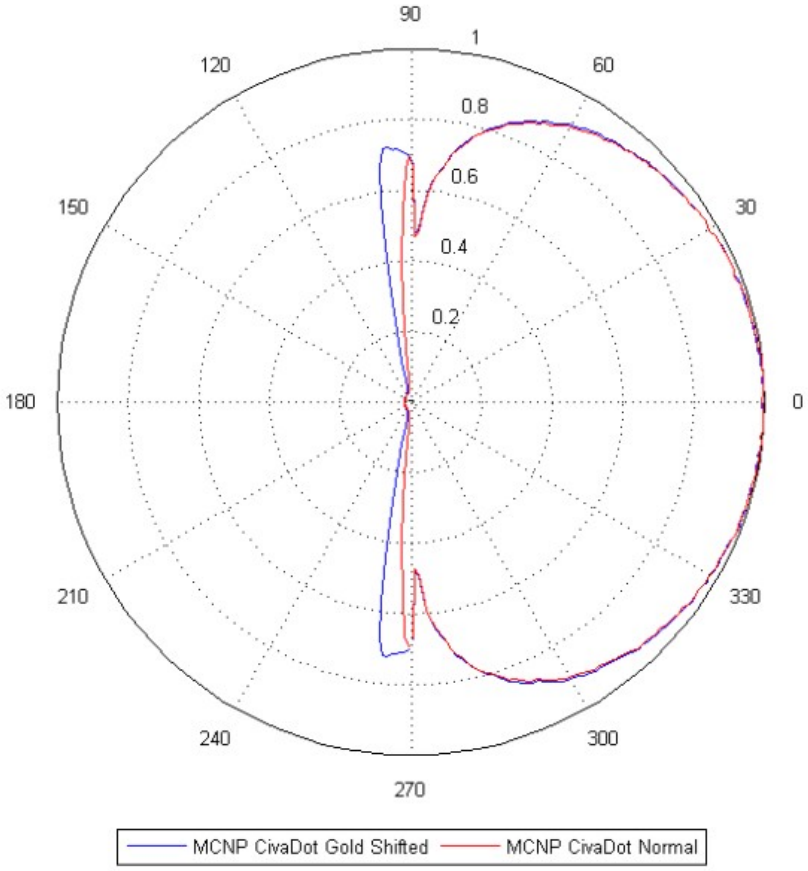

Figure 3.14: Anisotropy of CivaDot sources simulated using MCNP6. The red plot shows the simulation results of a normal CivaDot geometry whereas the blue plot shows the MC simulation results of a CivaDot with the gold shield shifted 100 microns upstream on the cold side of the source. All plotted values have been normalized to the maximum value in their dataset.

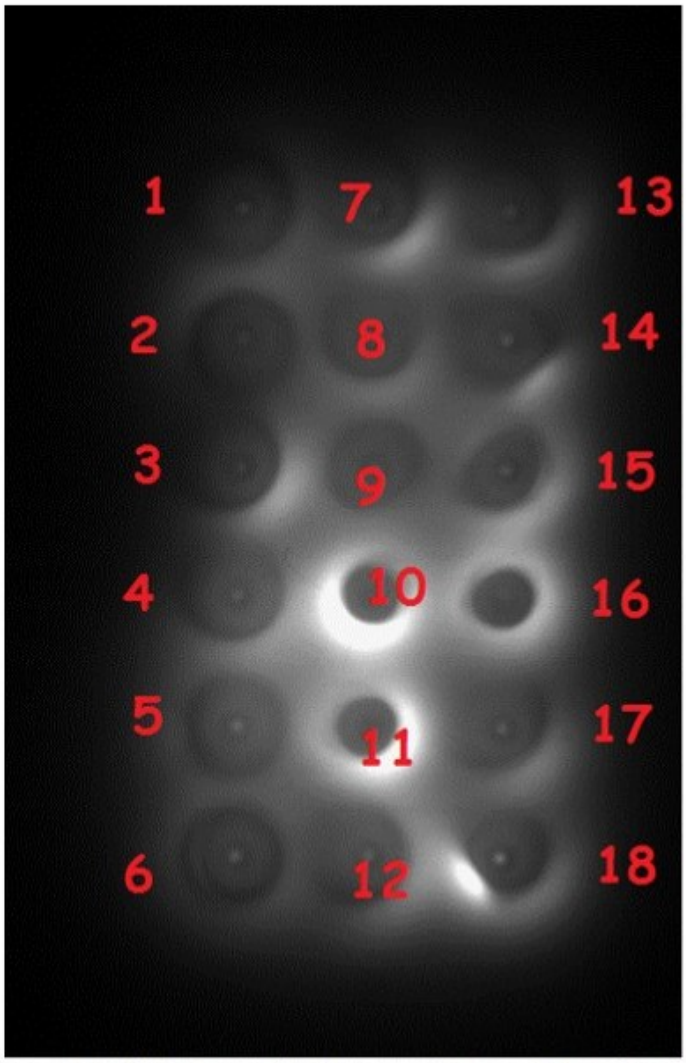

Figure 3.15: Digital radiograph from x-ray emission on gold shielded side of CivaDots with and without acceptable gold shielding placement. CivaDots 10, 11 and 18 have the gold placement problem detected by UWMRRC. [Imaged reproduced from personal communication, CivaTech Oncology Inc.]

3.7 Conclusions

Preliminary S_K measurements of CivaDots indicated that air-kerma strength is a good source strength metric to use with an adapted AAPM TG-43U1 (Rivard et al. 2004) protocol. Repeated measurements with the UW VAFAC indicated that a NIST WAFAC-based standard would be both feasible and practical as a source strength metric for a CivaDot. UW VAFAC source-specific correction factors for the CivaDot were recalculated due to the difference in energy spectra between the CivaDot and the bare ^{103}Pd sources used for current correction factor calculations. The corrections are larger since the energy spectrum contains more low-energy emission lines from the presence of the gold shield in near proximity to the ^{103}Pd region.

Primary S_K measurements of the CivaDot were successfully performed using two different free-air chambers, namely, the UW VAFAC and the NIST VAFAC for an intercomparison. The investigation assisted in the establishment of a primary source strength standard for the CivaDot. Good repeatability and reproducibility of the CivaDot primary air-strength measurements using the UW VAFAC were observed when comparing the results to the CivaDot S_K determined using the NIST WAFAC for multiple sources.

Chapter 4

Dosimetric characterization of an element of a directional brachytherapy source array

4.1 An adapted dosimetric formalism

This chapter focuses on the dosimetric characterization of an element of the CivaSheet, the CivaDot. Nath et al. and Rivard et al. established a formalism for the dosimetric characterization of conventional LDR brachytherapy sources. (Nath et al. 1995, Rivard et al. 2004; 2007) These traditional sources were cylindrically symmetric and had isotropic azimuthal emission. Equation 3.1 outlines the formalism proposed by the authors of the TG-43 report.

In the case of the CivaDot, the directional as well as planar nature of the source array renders the direct application of the TG-43 protocol inappropriate. In the previous chapter, the adapted definition of S_{K} (static on-axis measurement) was mentioned. Λ, $G_X(r,\theta)$, $g_X(r)$, and $F(r,\theta)$ were also adapted to accommodate this source, and analogous dosimetric

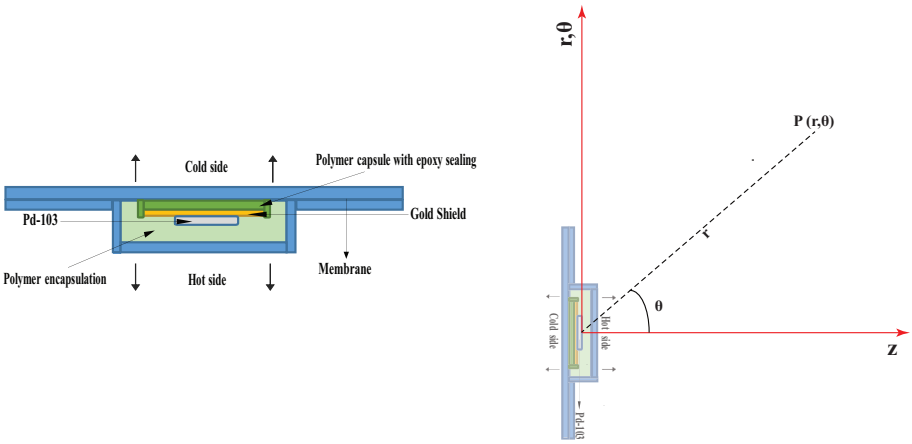

(a) (b)

Figure 4.1: a. An illustration of the CivaDot with its components in a cross-sectional view. b. An illustration of the coordinate system for CivaDot dosimetry. Note that the figures are not to scale.

parameters were defined for the source. Λ analog, $G_X(r,\theta)$ analog, $g_X(r)$ analog, and $F(r,\theta)$ analog were all defined on the source cylindrical axis considering the directionality of the CivaDot. A point source was assumed for the geometry function.

Figure 4.1 is an illustration of the CivaDot along with the proposed coordinate system for CivaDot dosimetry used in this work. The reference plane was defined as the bottom of the palladium region in the device and the origin was defined as the intersection of the reference plane and the cylindrical axis of the CivaDot.

4.2 Monte Carlo simulations

A Monte Carlo model of the CivaDot was created based on the specifications provided by CivaTech Oncology, Inc. The details of the CivaDot geometry are described in Chapter 2. MCNP6 radiation transport code v1.0 was used for all Monte Carlo calculations. Measured dose distributions of a source can be compared to Monte Carlo calculations. To establish

a basis for the relevant comparisons, an equivalence between the Monte Carlo calculations and the measured quantities was formulated.

4.2.1 Monte Carlo and Measurement Units Equivalence

The tally used for dose calculations for this work was the *f4 tally provided by the MCNP6 code. (Goorley) The *f4 tally estimates the energy fluence expected in a given volume of interest (cell) normalized to a starting particle.

$$*f4\ tally \rightarrow \frac{\text{MeV/cm}^2}{\text{photon}}$$

The tally when modified using the mass energy-absorption cross sections (μ_{en}/ρ) of the material constituting the volume of interest, provides a MCNP modified output as a collision kerma tally and can be used as an approximation for the absorbed dose. (Rivard et al. 2004)

$$\frac{\text{MeV/cm}^2}{\text{photon}} \times \frac{\text{cm}^2}{\text{g}} = \frac{\text{MeV/g}}{\text{photon}}$$

Assuming MCNP6 code provides a tally estimate of **'X'** for a given simulation using the modified *f4 tally. The quantity X has units MeV/g/photon. To convert X MeV/g/photon into the more familiar unit of Gray (J/kg), one can use the conversion factor as:

$$\mathbf{X}\ \frac{\text{MeV/g}}{\text{photon}} = \mathbf{X}\ (\frac{\text{MeV/g}}{\text{photon}}) \times \frac{1.602 \times 10^{-13}\ \text{J}}{1\ \text{MeV}} \times \frac{1000\ \text{g}}{1\ \text{kg}} = 1.602 \times 10^{-10}\ \ \mathbf{(X)}\ \ \frac{\text{Gy}}{\text{photon}}$$

4.2.1.1 Dose per activity (Gy/mCi) conversion

Using the conversion of 1 mCi into disintegrations per second and the branching ratio for ^{103}Pd (0.7714 photons per disintegration), the above result can be equated to instantaneous dose rate per unit activity:

$$1\ \text{mCi} = 3.7 \times 10^7\ \ \frac{\text{disintegrations}}{\text{second}}\ \ \textit{and}\ \ \frac{\dot{D}_o}{A}\ \rightarrow\ \ \frac{\text{Gy/s}}{\text{mCi}}$$

where $\dot{D}_o$ is the instantaneous dose-rate and A is the radionuclide activity.

$$\rightarrow 1\ \text{mCi}\ of\ ^{103}Pd = 3.7{\times}10^7\ \ \frac{\text{disintegrations}}{\text{second}}{\times}0.7714\ \ \frac{\text{photons}}{\text{disintegration}} = 2.8542{\times}10^7 \frac{\text{photons}}{\text{s}}$$

$$\rightarrow \frac{\dot{D}_o}{A} = (1.602{\times}10^{-10}\mathbf{X}\ \ \frac{\text{Gy}}{\text{photon}}){\times}\frac{2.8542 \times 10^7 \frac{\text{photons}}{\text{s}}}{1\ \text{mCi}}\ = 4.5724{\times}10^{-3}\ \ \mathbf{X}\ \ (\frac{\text{Gy/s}}{\text{mCi}})\ \ (4.1)$$

Dose varies with time as:

$$\frac{d\ \ (Dose)}{dt} =\ \ \dot{D}_o e^{-\lambda\ t}$$

where λ is the decay constant and t is time. The integrated dose from time, t=t_1 to t=t_2 is thus:

$$Dose =\ \ \dot{D}_o \int_{t_1}^{t_2} e^{-\lambda\ t}\ dt$$

Accounting for infinite decay, i.e., setting $t_2 = \infty$ and t_1 =0, the relation simplifies to:

$$Dose =\ \ \frac{\dot{D}_o}{\lambda} \rightarrow \frac{Dose}{Activity} = \frac{D}{A}\ \ =\ \ \frac{\dot{D}_o}{\lambda\ A}$$

The value of the ^{103}Pd decay constant λ is 4.7216×10^{-7} s^{-1}. Therefore,

$$\frac{Dose}{Activity} = 4.5724 \times 10^{-3}\ \ \mathbf{X}\ \ (\frac{\text{Gy/s}}{\text{mCi}}) \times (\frac{1}{4.7216 \times 10^{-7}}\text{s}) = 9.684 \times 10^3\ \ \mathbf{(X)}\ \ \frac{\text{Gy}}{\text{mCi}}\ \ (4.2)$$

Thus, a value of **X** MeV/g/photon from modified MCNP6 *f4 tally output for a given simulation can be equated to the dose per activity (Gy/mCi) by using a multiplication factor of $9.684{\times}10^3$ assuming infinite source decay for a ^{103}Pd source.

4.2.1.2 Air kerma strength per activity (U/mCi) conversion

Assuming the MCNP6 tally output to be **Y** MeV/g/photon in this case, then using equation 4.2 and air-kerma rate ($\dot{K}_\delta$) instead of dose:

$$\frac{\dot{K}_\delta}{A} = 4.5724 \times 10^{-3} \;\; (\mathbf{Y}) \;\; (\frac{\text{Gy/s}}{\text{mCi}})$$

Using TG-43 formalism (Nath et al. 1995, Rivard et al. 2004; 2007):

$$S_K = \;\dot{K}_\delta \times (d)^2 \quad \frac{\text{cGy-cm}^2}{\text{h}}$$

where S_K is the air-kerma strength, and d is the distance of measurement, set as 30 cm for all simulations.

$$\rightarrow \quad \frac{\textit{Air Kerma Strength}}{\textit{Activity}} \;\; = \;\; \frac{S_K}{A} = \;\; 4.5724 \times 10^{-3} (\frac{\text{Gy/s}}{\text{mCi}}) \times (30\text{cm})^2 \times \frac{100\text{cGy}}{1\text{Gy}} \times \frac{3600\text{s}}{1\text{hr}}$$

$$\rightarrow \quad \frac{S_K}{A} \;\; = \; 1.4814 \times 10^6 \;\; \mathbf{(Y)} \;\; \frac{\text{U}}{\text{mCi}} \tag{4.3}$$

4.2.1.3 Note

The units conversion is provided here for completion. The use of activity as a measure of source strength for clinical use is not recommended.

4.2.1.4 Dose-rate constant analog

The dose-rate constant is an important dosimetric parameter for any brachytherapy source. It is a measure of the dose delivered per unit source strength for the device. Using the

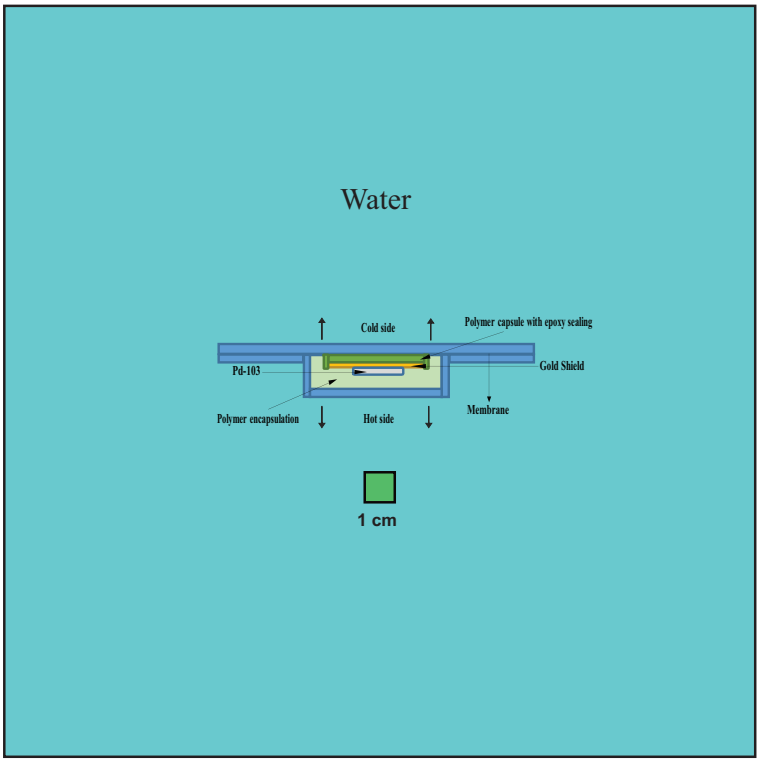

Figure 4.2: Illustration of the Monte Carlo simulation setup for the dose to water determination for the CivaDot.

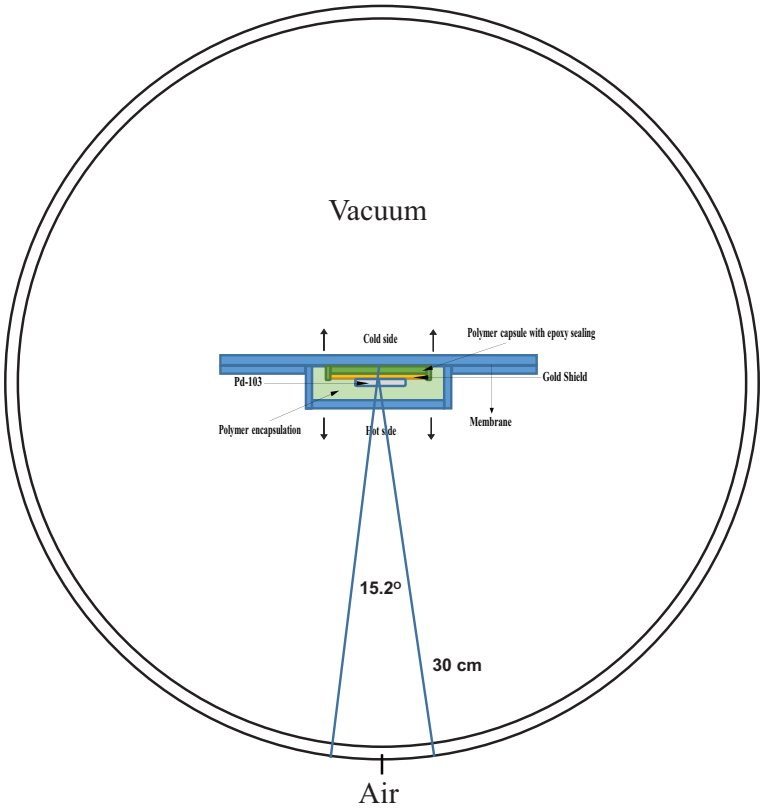

Figure 4.3: Illustration of the Monte Carlo simulation setup for the air-kerma strength determination for the CivaDot.

definition of dose-rate constant from TG-43 (Nath et al. 1995, Rivard et al. 2004; 2007):

$$\Lambda \ \ (\text{cGy h}^{-1}\ \text{U}^{-1}) = \frac{\dot{D}}{S_K}$$

where $\dot{D}_o$ is the absorbed dose rate to water at a distance of 1 cm in a volume of water, and S_K is the air-kerma strength in a volume of air in a 30 cm sphere in vacuum at an angle of 15.2 degrees.

Figure 4.2 is an illustration of the Monte Carlo simulation setup for the calculation of dose from a CivaDot source and Figure 4.3 is an illustration of the Monte Carlo simulation setup for the air-kerma strength determination for the CivaDot.

From Equation 4.2 and 4.4,

$$\frac{\dot{D}}{A} \;=\; 4.5724 \times 10^{-3}(\frac{\frac{\text{Gy}}{\text{s}}}{\text{mCi}}) = 1.646 \times 10^{3} \times \mathbf{(X)}\ \text{cGy h}^{-1}\text{mCi}^{-1}$$

and

$$\frac{S_K}{A} = 1.4814 \times 10^{6}\mathbf{(Y)}\frac{\text{U}}{\text{mCi}}$$

where X and Y are the *f4 tally results for dose to water and air-kerma simulations.

Therefore, using MCNP6, the dose-rate constant for a source can be calculated as:

$$\rightarrow \Lambda = \frac{\frac{\dot{D}_o}{A}}{\frac{S_K}{A}} = \frac{1.646 \times 10^{3} \times \mathbf{X}}{1.4814 \times 10^{6} \times \mathbf{Y}} = \frac{\mathbf{X}}{900 \times \mathbf{Y}}\ \ \text{cGy h}^{-1}\text{U}^{-1} \tag{4.4}$$

4.2.2 MC simulation details

The updated low-energy photon cross section data library (mcplib12) was used for the simulations. The ^{103}Pd photon spectrum from the National Nuclear Data Center online NUDAT 2.6 database (Brookhaven National Laboratory) was used. A *f4 tally was used for absorbed-dose calculations, with energy fluence modified by μ_{en}/ρ values. A minimum of 10^9 histories were used for each simulation. Photon mass-energy absorption cross-sections of various materials were used from the NIST XCOM database. (Berger et al. 2005) The photon transport cut off was set to 100 eV. No electron transport was simulated. All Monte Carlo simulations for this work assumed a palladium loading of 50%, i.e. the ^{103}Pd region is uniformly filled with 50% palladium material and 50% epoxy by mass, with a net density of $\rho = 1.9987\,\text{g}\,\text{cm}^{-3}$.

The CivaDot was modeled using MCNP6 and the source was simulated in various geometries replicating the various CivaDot measurement setups:

1. A full UW VAFAC model with the CivaDot in its measurement position

2. CivaDot air-kerma strength simulation

3. The source in a PMMA phantom with (a) TLD microcubes, (b) EBT3 film

4. The source in a PMMA phantom with an EBT3 filmstack phantom

5. The source in a water phantom

4.2.3 Monte Carlo modeling baseline verification

The dose-rate constant analog determined for the CivaDot source using MCNP6 was 0.558 cGy U^{-1} h^{-1}. When compared to the dose-rate constant reported by TG-43 (Rivard et al. 2004) for conventional ^{103}Pd sources such as Theragenics 200 (0.686 cGy U^{-1} h^{-1}) and NASI MED 3633 (0.688 cGy U^{-1} h^{-1}), it is about 23% lower. The difference between the dose rate constants can be attributed to the impact of the gold shield present in the CivaDot on the source dose distribution. To verify this, an additional Monte Carlo simulation was performed. The gold shield of the CivaDot was replaced by the outside bio-absorbable material of equal thickness in the simulation. This change makes the CivaDot emit radiation symmetrically in the azimuthal direction, similar to the conventional ^{103}Pd sources. The resulting dose-rate constant value was found to be within 1% of the reported values for Theragenics 200 and NASI MED 3633 sources, which shows a good proof of principle for our Monte Carlo MCNP6 simulations cross referenced to a published dose-rate constant for conventional Pd-103 sources.

4.3 CivaDot dosimetric parameters determination

4.3.1 Thermoluminescent dosimeter measurements

A polymethyl methacrylate (PMMA) phantom was designed to perform dose-to-water measurements of the CivaDot using thermoluminescent dosimeter microcubes (TLDs). Figure 4.4 is an illustration of the PMMA phantom design for measuring the dose-rate constant (DRC) analog for the CivaDot using TLDs. The PMMA phantom dimensions were

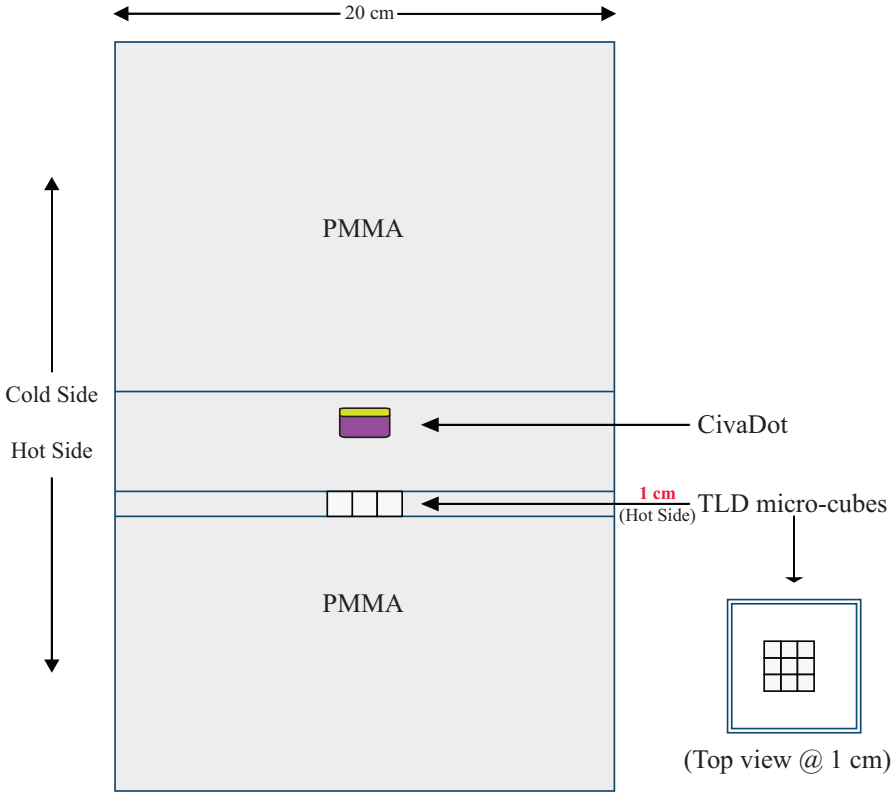

Figure 4.4: Illustrations of the PMMA phantom used for the CivaDot DRC analog measurement using nine TLD microcubes in a $3 \times 3 \times 1$ mm^3 slot centered on the source cylindrical axis at 1 cm away from the source. A smaller figure on the side (Top view @ 1cm) is provided as an illustration of the top view of the TLD microcubes placed side-by-side in the relevant PMMA insert at 1 cm plane. Note that the illustrations are not to scale.

$20 \times 20 \times 12$ cm^3. The TLD microcubes used were TLD-100 model (LiF:Mg,Ti) manufactured by Thermo Fisher Scientific Inc. (Waltham, MA). The source was placed in the center of the phantom, and nine TLD microcubes were irradiated along its central axis at a distance of 1 cm on the hot side of the source. The nine TLD microcubes were placed side-by-side in a $3 \times 3 \times 1$ mm^3 slot in the phantom, which was centered on the source long axis. For conventional brachytherapy sources, this measurement is usually performed on the source transverse axis.

TLDs were annealed using the standard University of Wisconsin-Madison Medical Radiation Research Center (UWMRRC) protocol. They were read out using a a Harshaw 5500

automated reader (Thermo Fisher Scientific, Inc., Waltham, MA). Additional details about TLD annealing and readout are provided by Nunn et al. and Reed et al. (Nunn et al. 2008, Reed et al. 2014a) The dose-rate constant analog for the CivaDot using TLD measurements in a PMMA phantom can be determined with the application of Equation 4.6:

$$\frac{(\dot{D}_{\text{water}})^{\text{CivaDot}}_{\text{water}}}{S_{\text{K}}} = \frac{\lambda}{S_{\text{K}}.(e^{-\lambda t_1} - e^{-\lambda t_2})} \cdot (M_{\text{TLD}})^{\text{CivaDot}}_{\text{phantom}} \cdot CR \cdot IEC \cdot PDC \tag{4.5}$$

where the notation is $(X_{\text{material}})^{\text{Source}}_{\text{Medium}}$, D is dose, M is charge reading, λ is ^{103}Pd decay constant, t_1, t_2 are start and stop irradiation times respectively, CR is the calibration ratio, IEC is the the intrinsic-energy correction, and PDC refers to the phantom/detector correction. The dose and the charge reading components of this equation can be described as:

1. $(M_{\text{TLD}})^{\text{CivaDot}}_{\text{phantom}}$ refers to the in-phantom measurement.
2. CR = $\frac{(D_{\text{water}})^{\text{Co-60}}_{\text{Cal}}}{(M_{\text{TLD}})^{\text{Co-60}}_{\text{Cal}}}$ is the calibration ratio.
3. IEC = $(\frac{(D_{\text{TLD}})^{\text{CivaDot}}_{\text{phantom}}}{(M_{\text{TLD}})^{\text{CivaDot}}_{\text{phantom}}} \cdot \frac{(M_{\text{TLD}})^{\text{Co-60}}_{\text{Cal}}}{(D_{\text{TLD}})^{\text{Co-60}}_{\text{Cal}}})$ refers to the intrinsic-energy correction.
4. PDC = $(\frac{(D_{\text{water}})^{\text{CivaDot}}_{\text{water}}}{(D_{\text{TLD}})^{\text{CivaDot}}_{\text{phantom}}} \cdot \frac{(D_{\text{TLD}})^{\text{Co-60}}_{\text{Cal}}}{(D_{\text{water}})^{\text{Co-60}}_{\text{Cal}}})$ is the phantom/detector correction.

Various correction factors have to be calculated to determine the CivaDot DRC analog. The phantom/detector corrections were calculated using MCNP6 simulations of the measurement geometry and a water phantom. For the TLD measurements, additional TLD microcubes were irradiated using a ^{60}Co beam to relevant dose-to-water values for calculating the TLD calibration coefficient (cGy/nC). Since there is no consensus DRC analog value for the CivaDot, the most appropriate intrinsic-energy correction values for the TLD measurements are the NIST-matched x-ray beam UW40-M (effective energy: 19.2 keV, 40 kVp) value reported by Nunn et al. (Nunn et al. 2008) and the ^{103}Pd Best LDR seed Model

2335 value reported by Reed et al. (Reed et al. 2014a) An average of the valued reported by Nunn et al. and Reed et al. was used. The assumption using Reed et al.'s correction factor is:

$$\frac{(D_{\mathrm{TLD}})^{\mathrm{CivaDot}}_{\mathrm{phantom}}}{(M_{\mathrm{TLD}})^{\mathrm{CivaDot}}_{\mathrm{phantom}}} = \frac{(D_{\mathrm{TLD}})^{\mathrm{Pd\text{-}103}}_{\mathrm{VAFAC}}}{(M_{\mathrm{TLD}})^{\mathrm{Pd\text{-}103}}_{\mathrm{VAFAC}}}$$

The assumption using Nunn et al.'s correction factor is:

$$\frac{(D_{\mathrm{TLD}})^{\mathrm{CivaDot}}_{\mathrm{phantom}}}{(M_{\mathrm{TLD}})^{\mathrm{CivaDot}}_{\mathrm{phantom}}} = \frac{(D_{\mathrm{TLD}})^{\mathrm{M\text{-}40}}_{\mathrm{calibration}}}{(M_{\mathrm{TLD}})^{\mathrm{M\text{-}40}}_{\mathrm{calibration}}}$$

The DRC analog was determined for eight CivaDot sources using TLDs in phantom.

4.3.2 EBT3 film

Dose-to-water measurements were also performed using Gafchromic EBT3 films manufactured by Ashland Inc. (Convington, KY) for eight CivaDot sources in the PMMA phantom using a different insert. The EBT3 film was placed on top of a PMMA slab and the film edges were secured using kapton tape. The setup was similar to the TLD measurements, with a 3×3 cm^2 segment of EBT3 film placed at 1 cm away from the source along its central axis. The CivaDot dose-rate constant analog was also measured using EBT3 film. The next section describes the calibration procedure and other associated details for the EBT3 film measurement.

Equation 4.6 was adapted for the EBT3 film measurements, and the related correction factors were determined using MCNP6 simulations of the CivaDot source in the measurement setup and in a water phantom. The DRC analog was estimated using the film measurements by evaluating a region-of-interest (ROI) of the same size as the TLD-microcube setup slot, 3×3 mm^2. A comparison of the two dosimeters was performed to evaluate the accuracy of an individual dosimeter and to also demonstrate the applicability of using

EBT3 film for further characterization of the CivaDot dose distribution. The DRC analog for the CivaDot was then determined for eight sources using EBT3 film.

4.3.2.1 EBT3 film calibration and readout

The EBT3 film dosimeters were read out using an EPSON (Nagano, Japan) 10000XL flatbed scanner. Two days prior to each in-phantom measurement, the required EBT3 films were cut from the same batch. The cropped films were pre-scanned six hours before an exposure along with a set of NIST-traceable optical density (OD) filters (Kodak Wratten^{TM} No. 96 polyester neutral density filters). The measured OD values of the NIST-traceable OD filters [individual pixels converted to optical density using a -log(pixel value/65535) function] were compared to their actual OD values for every film readout performed. A linear fit function was calculated by fitting the observed and the actual OD values of these filters. The observed individual pixel OD values of the film dosimeters read out were then mapped back to their traceable OD values using the linear fit obtained with the filters. This process mitigates some of the instrument variability between scans as the actual optical density of the filters can be assumed to vary negligibly during the course of the measurements. The films were then read out along with the filters a week after a CivaDot irradiation was performed. Two background films were also used for each measurement, and their net optical density was subtracted from the measured optical density. Figure 4.5 is the raw image acquired with the EPSON 10000XL scanner of an EBT3 film irradiated with a CivaDot source and scanned along with the NIST-traceable optical density (OD) filters.

A calibration curve was determined for the film measurements by irradiating additional films using a NIST-matched UW40-M x-ray beam (effective energy:19.2 keV, 40 kVp). A total of sixty-two dose-to-water values were used for the calibration curve, with four films irradiated for each dose. The relevant exposure times for the UW40-M x-ray beam were calculated using a NIST-traceable ionization chamber measurement of the beam air-

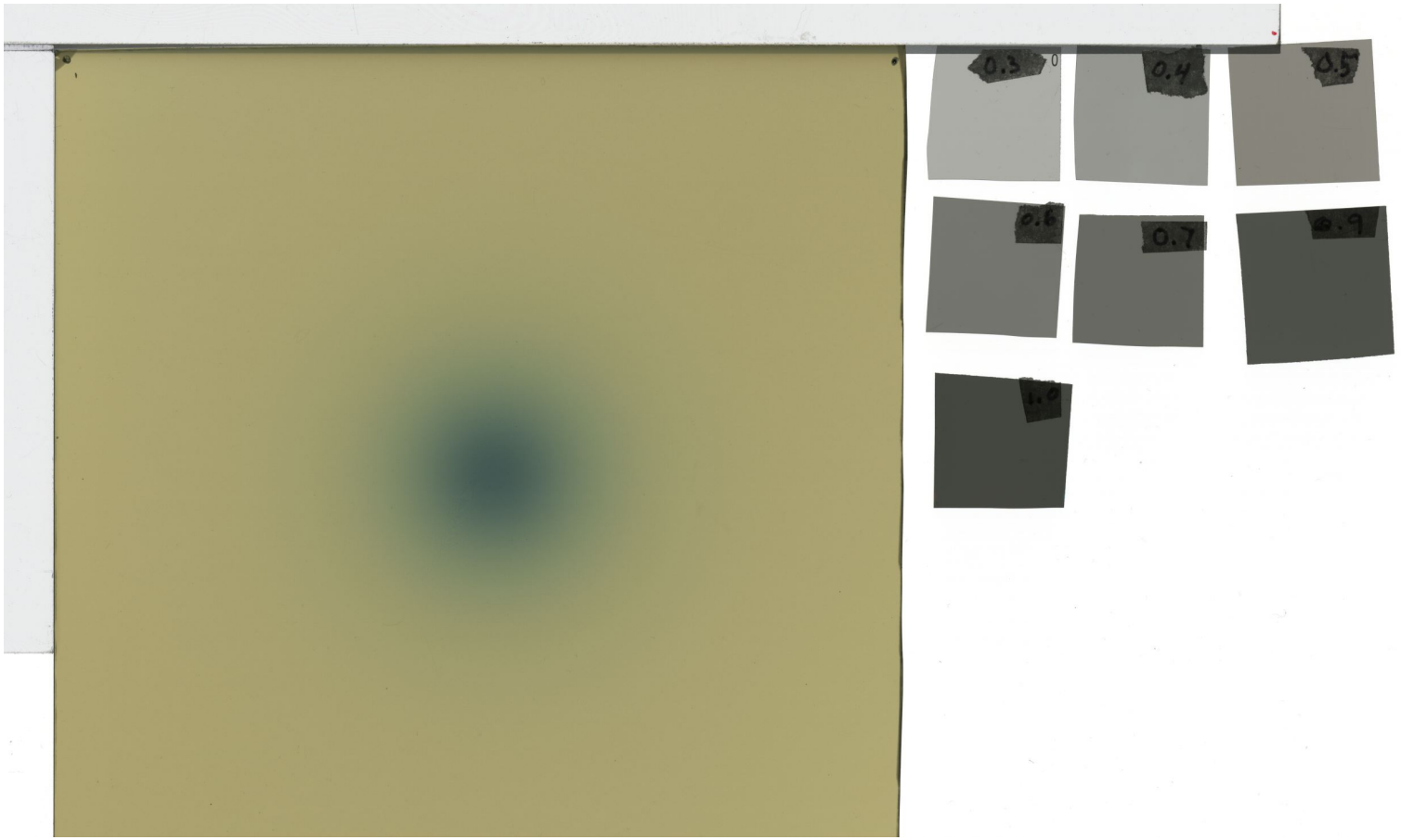

Figure 4.5: An image acquired with the EPSON 10000XL scanner of an EBT3 film irradiated with a CivaDot source. A set of NIST-traceable optical density (OD) filters (Kodak Wratten™ No. 96 polyester neutral density filters) were scanned with each film to lessen the impact of scanner inconsistency.

kerma, and then using a Monte Carlo estimated air-kerma to dose-to-water conversion ratio. Methods outlined by Hammer et al. were followed for the calibration irradiation procedure. (Hammer et al.) Figure 4.6 shows the results of the calibration. A cubic polynomial fit was used to assess the calibration dose value and the measured net optical density relationship. The CivaDot source and the phantom setup were modeled using the MCNP6 code. The phantom/detector corrections were calculated using MCNP6. The intrinsic-energy correction value for this measurement was assumed to be unity based on the findings of Morrison et al. and Chiu-Tsao et al. (H.Morrison et al. 2014, Chiu-Tsao et al. 2014) The assumption is:

$$\left(\frac{f\left(D_{\mathrm{EBT3}}, netOD_{\mathrm{EBT3}}\right)^{\mathrm{CivaDot}}_{\mathrm{phantom}}}{f\left(D_{\mathrm{EBT3}}, netOD_{\mathrm{EBT3}}\right)^{\mathrm{UW40\text{-}M}}_{cal}} \right) = 1$$

where the notation is $(X_{\mathrm{material}})^{\mathrm{Source}}_{\mathrm{Geometry}}$, D is dose, netOD is the net optical density, f is the calibration curve fit converting netOD to dose.

$(D_{\mathrm{EBT3}})^{\mathrm{CivaDot}}_{\mathrm{phantom}}$ is determined using the $(netOD_{\mathrm{EBT3}})^{\mathrm{CivaDot}}_{\mathrm{phantom}}$ measured with the flatbed scanner for an EBT3 film irradiated with the CivaSheet and applying the calibration function. The dose-rate constant analog can be determined for the CivaDot using the equation:

$$\frac{\left(\dot{D}_{\mathrm{water}}\right)^{\mathrm{CivaDot}}_{\mathrm{water}}}{S_{\mathrm{K}}} = \frac{\lambda}{(e^{-\lambda t_1} - e^{-\lambda t_2}) \times (S_{\mathrm{K}})} \times (D_{\mathrm{EBT3}})^{\mathrm{CivaDot}}_{\mathrm{phantom}} \times \left(\frac{(D_{\mathrm{water}})^{\mathrm{CivaDot}}_{\mathrm{water}}}{(D_{\mathrm{EBT3}})^{\mathrm{CivaDot}}_{\mathrm{phantom}}} \right) \quad (4.6)$$

where the notation is λ is the Pd-103 decay constant, and t_1, t_2 are irradiation start and stop times respectively. $\left(\frac{(D_{\mathrm{water}})^{\mathrm{CivaDot}}_{\mathrm{water}}}{(D_{\mathrm{EBT3}})^{\mathrm{CivaDot}}_{\mathrm{phantom}}} \right)$ was determined using Monte Carlo simulations.

4.3.2.2 Film analysis

The post-scanning analysis was performed using MATLAB software version R2016a developed by Mathworks Inc. (Natick, MA). The red-channel values were used for all analysis, as the red channel is most sensitive to doses in the range of interest. (Borca et al. 2013)

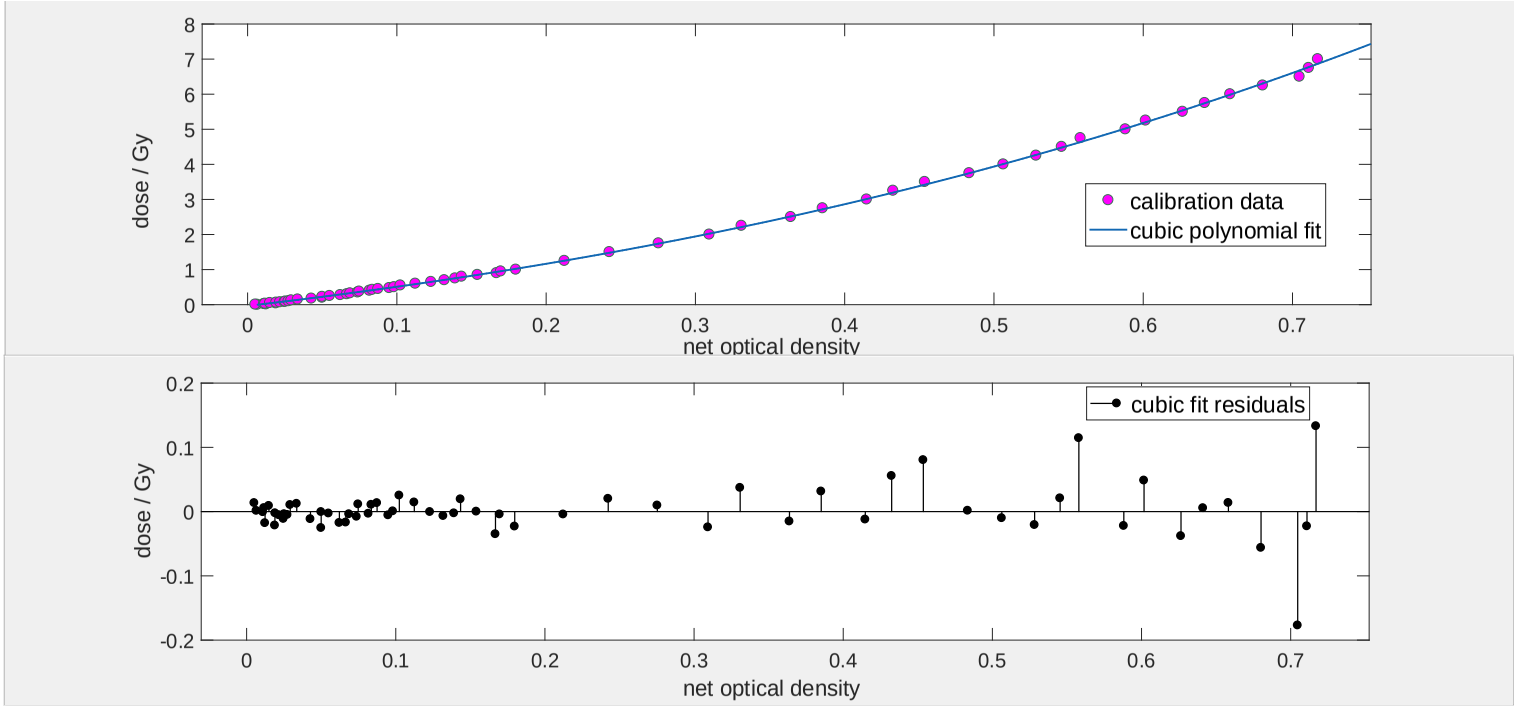

Figure 4.6: EBT3 film calibration curve using sixty-two dose-to-water values incorporating different dose levels in a CivaDot in-phantom irradiation. The dose-to-water values ranged from 10 mGy to 7 Gy. A cubic polynomial fit was used to assess the dose and net optical density relationship. A plot of the residuals of the data from the calibration function is also provided in the figure.

Once a film was scanned, the individual pixel values were converted to traceable OD filter values and finally, the net OD values for a given film were calculated by subtracting its pre-exposure OD value and the background film OD change from the post-exposure OD value. The net OD values were then converted to absolute dose-to-water values using the calibration curve.

4.3.3 DRC analog results

Table 4.1 presents the results of the dose-rate constant analog determined for the CivaDot with TLD microcubes and EBT3 film using eight sources each. The values reported in columns 2 and 3 of the table present the average measured DRC analog determined with TLD microcubes and EBT3 film respectively. The agreement between the TLD measured DRC analog values and MCNP6 predicted DRC analog (0.558 cGy h^{-1} U^{-1}) was within 5% with an average difference of -2.6%. For EBT3 film, all measured values agreed with the MC calculations to within 4% with an average difference of 0.6%. The measured and Monte Carlo weighted DRC analog was determined to be 0.555±0.013 cGy h^{-1} U^{-1}.

4.4 CivaDot dose distribution measurements using a film stack phantom

A PMMA phantom was designed to perform dose measurements of the CivaDot using Gafchromic EBT3 films at multiple depths. Figure 5.1 is an illustration of the PMMA phantom, $20 \times 20 \times 12$ cm^3, used for these measurements. The CivaDot source was placed in the center of the phantom and six EBT3 films with dimensions, 12×12 cm^2, were irradiated simultaneously along its central axis at various depths. Five EBT3 films were placed on the hot side of the source at distances of 1 cm, 2 cm, 3 cm, 4 cm, 5 cm and one on the cold side of the source at a distance of 0.5 cm. For conventional brachytherapy sources,

Table 4.1: The average dose-rate constant analog measured using TLD microcubes applying the average of Reed et al.'s and Nunn et al.'s intrinsic energy correction factor and Gafchromic EBT3 film for eight CivaDot sources. A comparison with the DRC analog determined using MCNP6 is also provided

Source ID #	Av. Measured DRC analog using TLDs (cGy h^{-1} U^{-1})	Av. Measured DRC analog using EBT3 film (cGy h^{-1} U^{-1})
Sep2015-CivaDot1	0.552	0.555
Sep2015-CivaDot2	0.544	0.553
Sep2015-CivaDot3	—	0.564
CSH-010-13	0.544	0.574
CSH-010-14	0.559	0.543
Dec2015-CivaDot2	0.533	—
Dec2015-CivaDot3	0.531	—
Dec2015-CivaDot4	0.543	—
Dec2015-CivaDot5	0.546	—
May2016-CivaDot1	—	0.580
Aug2016-CivaDot1	—	0.572
Nov2016-CivaDot1	—	0.552
Average DRC analog value	0.544	0.561
Standard deviation	1.7%	2.3%
Average difference from MCNP6 DRC analog	-2.6%	0.6%

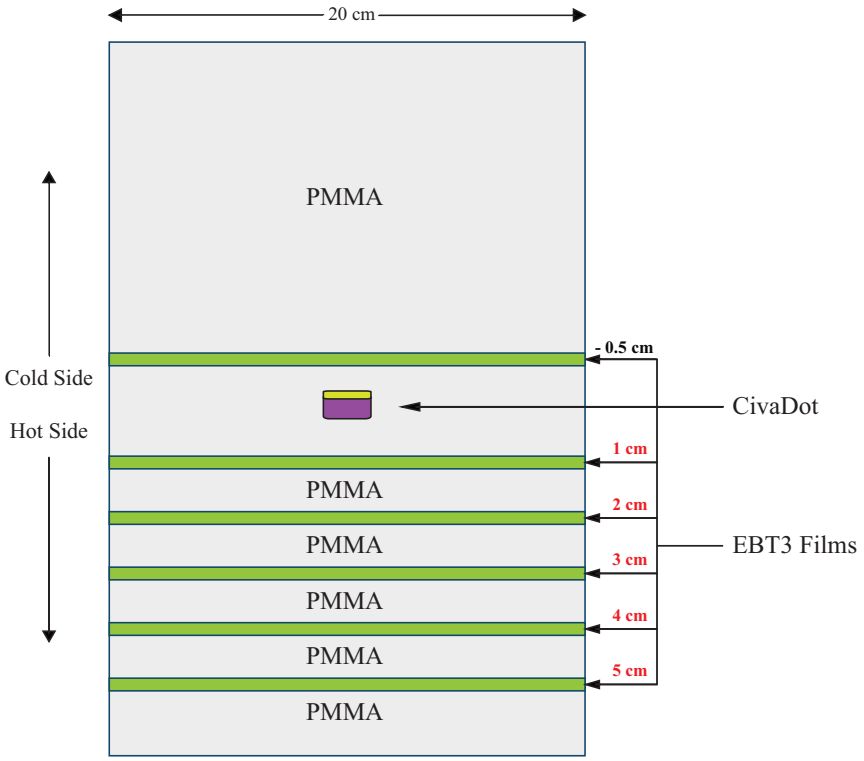

Figure 4.7: An illustration of the PMMA film stack phantom setup for the CivaDot dose distribution measurements, using six EBT3 films placed at different depths on the source cylindrical axis. Please note that the illustration is not to scale.

this measurement is usually performed on the source transverse axis. Measurements were performed for three CivaDot sources using the EBT3 film stack setup.

The measurement setup was simulated using MCNP6. Phantom and detector correction factors to a water medium were calculated using MC methods. The measured dose distribution values obtained for a given film in phantom were converted to dose-rate to water values. The measured values at different depths were compared to the MC predicted dose distributions at those depths. This comparison was performed using a dose difference map, whereby each pixel of the simulated CivaDot dose distribution was subtracted from the measured CivaDot dose distribution. TG-43 analog dosimetric parameters such as radial dose function analog and 2D anisotropy function analog were also assessed for the measured

and the simulated dose distributions. For analysis, an ROI of ±0.25 mm was set around the relevant dose distribution to calculate a dosimetric parameter.

4.5 Film stack measurement and MCNP6 calculated results

4.5.1 Dose difference maps

The dose rate-to-water distribution normalized to air-kerma strength of a CivaDot measured at a distance of 1 cm (hot side) from the source is shown in Figure 4.8. For analysis, the dose-rate distributions normalized to S_{K} of all three CivaDot sources measured in-phantom using EBT3 film were compared to the MCNP6 predicted dose-rate distribution normalized to S_{K} at all the six depths.

Figures 4.9 and 4.10 present the results of the x-profile and the y-profile for the three CivaDot sources measured in-phantom at the 1 cm plane (hot side) as well as the MCNP6 prediction.

Figure 4.11 shows the results of the pixel-by-pixel difference map of the measured and predicted dose distribution of the source at 1 cm depth. As observed in the figure, most differences were within 2% to 3%, with maximum differences up to 5%. On the cold side of the source, the EBT3 measured dose distribution at 0.5 cm agreed with the MC predicted distribution to within 3.5% of the prescribed dose at 1 cm depth. Note that a slight ring artifact is noticeable in Figure 4.11 at very low dose levels, which has a negligible impact on the observed dose distribution results. This scanner artifact was caused due to a firmware/software issue, whereby the scanner reported lower than measured values for a very small set of bins of the red channel. The issue was later resolved with a firmware/software upgrade of the scanner.

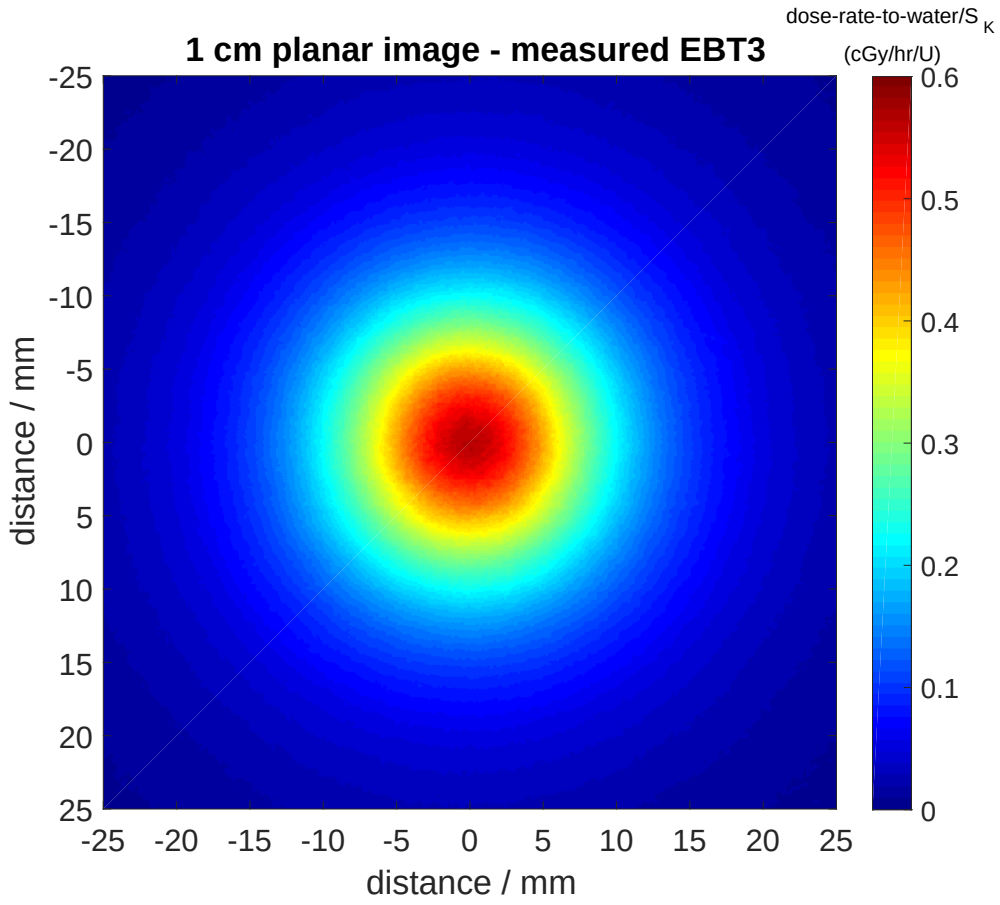

Figure 4.8: The results of the CivaDot planar dose-rate distribution measurement using EBT3 film at 1 cm (hot side) from the source along its cylindrical axis normalized to the source air-kerma strength.

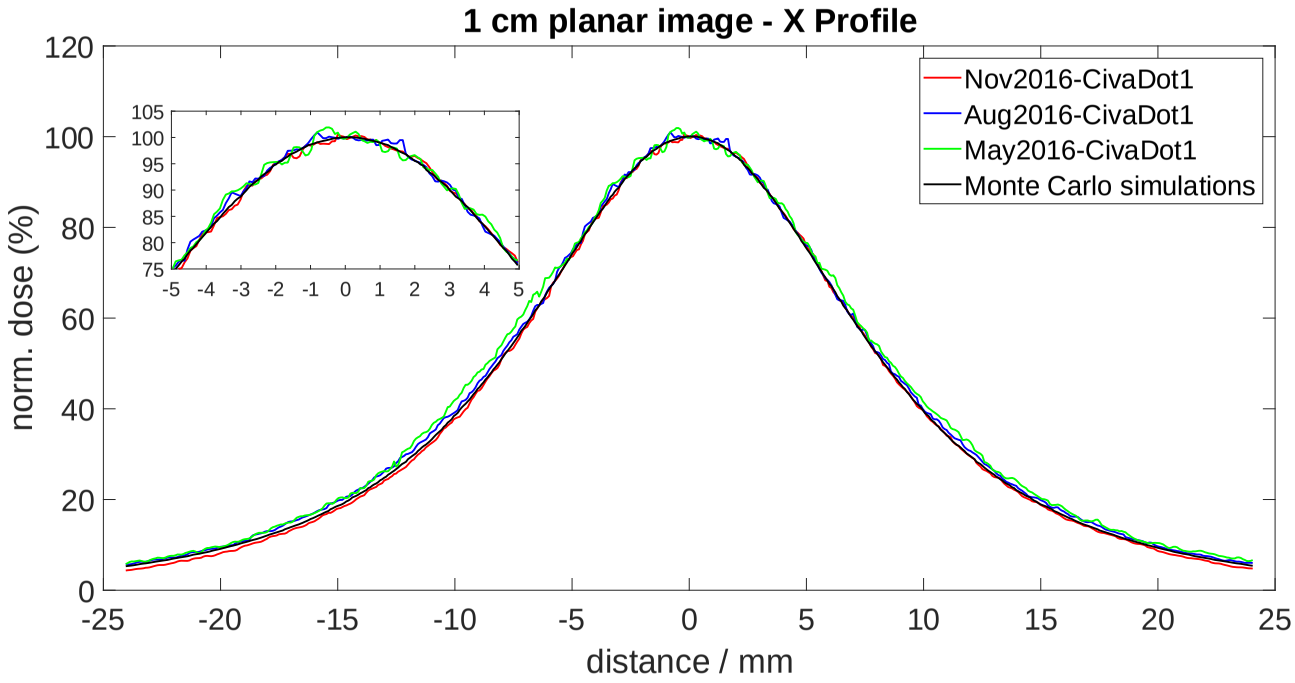

Figure 4.9: The results of the measured profiles for three CivaDot sources as well as Monte Carlo simulated profiles at 1 cm plane (hot side) for x-axis. Each curve has been normalized to their respective central-axis dose-rate/S_{K} value.

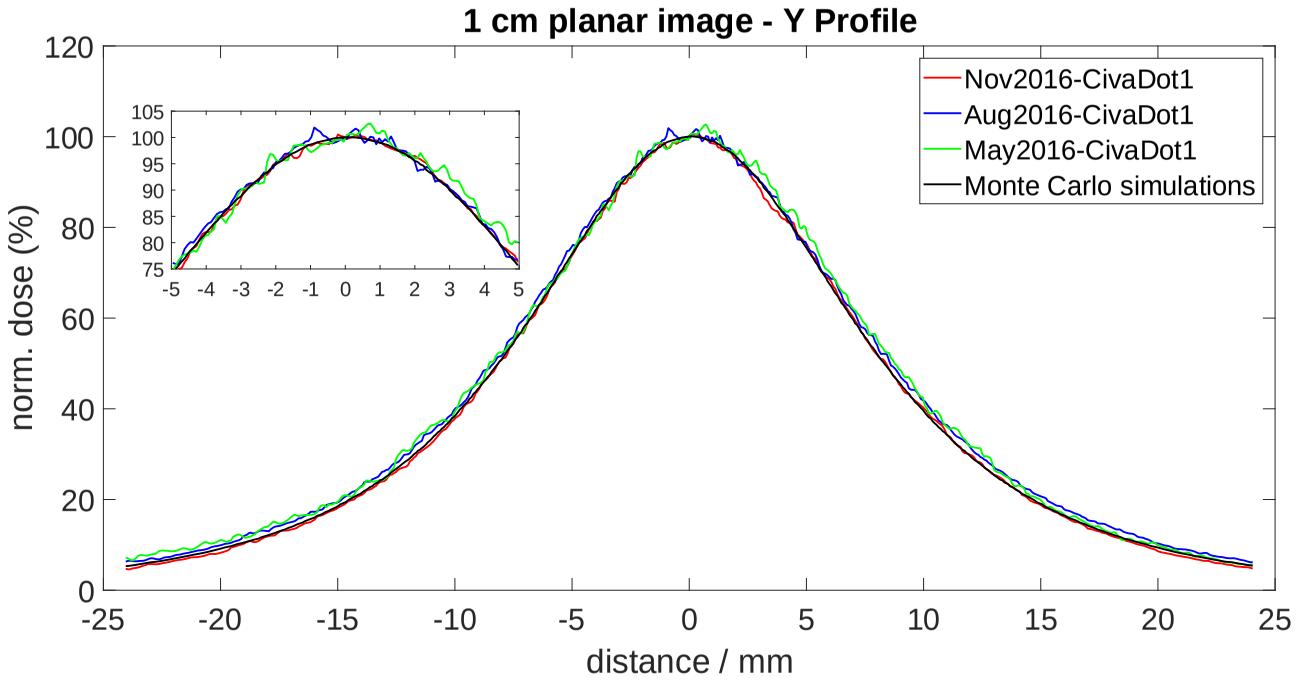

Figure 4.10: The results of the measured profiles for three CivaDot sources as well as Monte Carlo simulated profiles at 1 cm plane (hot side) for y-axis. Each curve has been normalized to their respective central-axis dose-rate/S_{K} value.

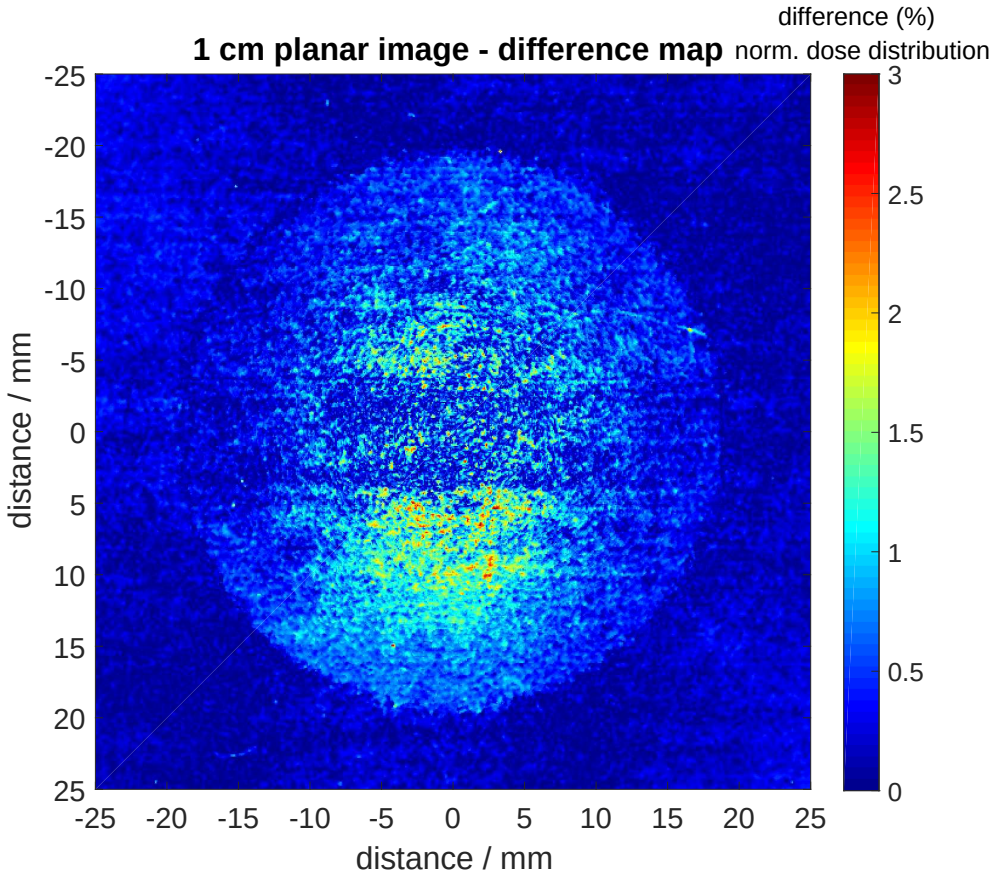

Figure 4.11: The difference in the measured dose distribution and the predicted dose distribution at 1 cm. Both dose distributions were normalized to the MC maximum dose value.

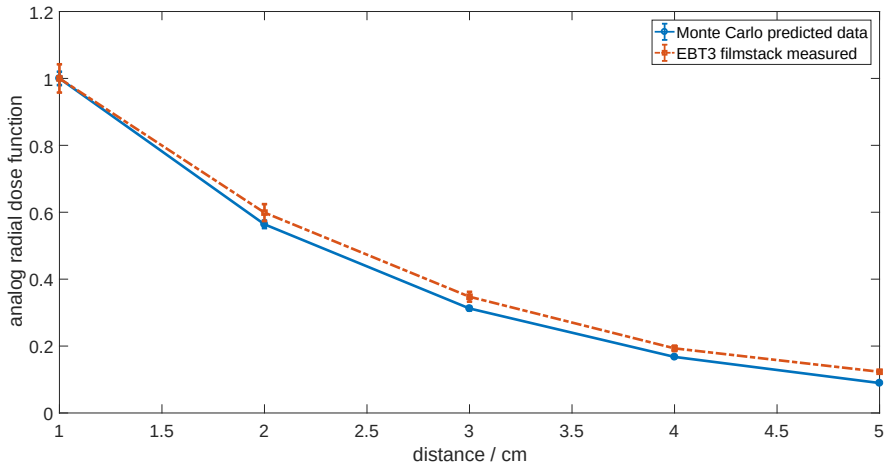

Figure 4.12: The radial dose function analog determined for the CivaDot using the EBT3 film stack setup and MCNP6 Monte Carlo simulations.

4.5.2 TG 43 analog dosimetric parameters

4.5.2.1 CivaDot radial dose function analog results

The radial dose function (RDF) analog was determined for the source based on TG-43 protocol definition adapted to an on-axis definition considering the directionality of the CivaDot. Figure 4.12 and Table 4.2 present the results of the measured RDF analog and the Monte Carlo predicted RDF analog. Good agreement was observed at 2 cm depth (within 6.3%), with a divergence at deeper depths. On the cold side of the source, the EBT3 measured RDF analog at the depth of 0.5 cm was 0.0462 and the Monte Carlo predicted RDF analog was 0.0394.

4.5.2.2 CivaDot 2D anisotropy function analog results

Since the measurement setup utilized a stacked geometry, the cylindrical nature of the 2D anisotropy function limits the number of measured data points that can be used for a comparison with Monte Carlo simulations. An ROI of 0.5 mm was set around the intersection of a given polar angle with the film stack planes at set radii. Table 4.3 presents the results

Table 4.2: Comparison of the average RDF analog measured using EBT3 filmstack (three CivaDot sources) and Monte Carlo simulations.

r (cm)	EBT3 measured g_p(r)	MCNP6 predicted g_p (r)	Ratio Measured/Predicted	Rivard (Rivard 2017) g_L (r)
0.5	—	1.310±0.026	—	1.344
1	1.000±0.042	1.000±0.020	1.000	1.000
2	0.599±0.025	0.564±0.011	1.062	0.558
3	0.348±0.015	0.312±0.006	1.112	0.305
4	0.193±0.008	0.168±0.003	1.152	0.164
5	0.123±0.005	0.090±0.002	1.376	0.088

of this comparison. Good agreement was observed between the measured and predicted $F(r,\theta)$ ($\leq$6.5%) for distances up to 3 cm.

4.5.3 Discussion

Dose distribution measurements of the CivaDot were performed using TLD microcubes and EBT3 film in a PMMA phantom for eight CivaDot sources to determine the dose rate constant analog. The source dose distribution was also predicted by using Monte Carlo simulations. Good agreement was observed between the two dosimeters and Monte Carlo predicted dose distribution. The average agreement of EBT3 measured DRC analog is within 3.5% of the TLD measured DRC analog for all CivaDot sources measured. This agreement is within the overall uncertainty of the measurements using the two dosimeters. This demonstrates the suitability of using EBT3 film as a dosimeter for absolute dose measurements of LDR brachytherapy sources as TLDs are the standard dosimeter of choice for such measurements.

Rivard reported a DRC analog value of 0.579 cGy h^{-1} U^{-1} which is 4.2% different from the DRC analog value determined by this work (0.555 cGy h^{-1} U^{-1}). (Rivard 2017) Potential reasons for disagreement may include differences in the choice of origin and the amount of palladium loading. Rivard used the center of the gold shield on the CivaDot cylindrical axis as the source origin. (Rivard 2017)

A subsequent CivaDot dose distribution measurement was performed using a film stack in a PMMA phantom. EBT3 films were placed at multiple depths in phantom, and measurements were performed for three CivaDot sources. Overall good agreement was observed between EBT3 measured and MC predicted distributions using dose difference maps. The results presented in Figures 4.9, 4.10 demonstrate symmetry in source emission across the two axes compared to conventional LDR sources, which may have pronounced anisotropy. Radial dose function analog and 2D anisotropy function analog were also investigated. At

Table 4.3: Results of 2D Anisotropy function analog measured using the EBT3 film stack phantom and MCNP6

Radial distance (cm)	Polar angle (°)	EBT3 film $F(r,\theta)$	MCNP6 $F(r,\theta)$	Ratio Film/MC
1	0.0	1.001	1.000	1.002
1	120.0	0.074	0.070	1.058
2	0.0	0.999	0.999	0.999
2	60.0	0.932	0.943	0.989
2	104.5	0.141	0.133	1.063
3	0.0	0.996	0.999	0.997
3	48.2	0.954	0.963	0.991
3	70.5	0.844	0.895	0.943
3	99.6	0.198	0.186	1.064
4	0.0	0.988	1.000	0.987
4	41.4	0.818	0.979	0.836
4	60.0	0.750	0.935	0.802
4	75.5	0.632	0.870	0.727
4	97.2	0.168	0.231	0.725
5	0.0	0.995	1.000	0.996
5	36.9	0.828	0.980	0.845

depths of 1 cm, 2 cm, 3 cm good agreement was observed for the radial dose function with a slight divergence at deeper depths (4 cm and 5 cm). The absolute dose delivered at depths (4 cm and 5 cm) for a measurement is very small ($\leq$1.5%) compared to the dose prescribed at 1 cm depth, and thus the measurement uncertainty is much larger. Similar results were seen by Reed et al. when measuring the RDF for a conventional ^{103}Pd brachytherapy seed and comparing measurements to Monte Carlo data. (Reed et al. 2014b) Rivard's reported RDF analog were in good agreement with the MC RDF analog predicted values. (Rivard 2017) The measured 2D anisotropy function analog agreed to within 6.5% of the MC predicted values for distances up to 3 cm and within 28% for distances of 4 cm and 5 cm. Potential reasons for increased divergence at deeper depths may include the fact that absolute doses were very small at these depths and variation due to palladium loading for the 2D anisotropy function determined by MC can vary as much as 25% at these depths. A point to consider while using the dosimetric data for clinical purposes is that only the gold shield present in a given CivaDot is visible under computer tomography (CT) imaging, hence it is up to the user to plan accordingly for the post-implant dosimetry, and if possible, apply a shift (0.125 mm is the distance from the center of the gold shield to the source origin) to calculate dose more accurately in a treatment planning system. Cohen et al. performed an in-phantom measurement using EBT3 film to evaluate the appropriateness of Rivard's results for clinical commissioning of the CivaSheet using relative dosimetry. (Cohen et al. 2017)

4.6 Uncertainty

The combined (Types A and B) relative standard uncertainty associated with UW VAFAC CivaDot measurements of ^{103}Pd sources was provided in detail by Aima et al. (Aima et al. 2015) Taking the palladium loading into account, the relative standard uncertainty for the UW VAFAC S_{K} measurement with CivaDots is estimated to be $\sqrt{\sigma_{\mathrm{rep}}^2 + 0.75^2 + 1.62^2}$%,

where σ_{rep} is the reproducibility of the free-air chamber measurements as defined by Culberson et al. (Culberson et al. 2006)

The Monte Carlo simulation uncertainty budget is presented in Table 4.4 for CivaDot DRC analog and RDF analog determination. The Type B uncertainty associated with the simulations were based on the works of Reed et al., Rivard, Aima et al. (Reed et al. 2014b, Rivard 2017, Aima et al. 2015) The Type A tally statistics were within 1% for all simulations. An additional component of palladium loading was added as an uncertainty in Monte Carlo predicted values. Dose to water and air-kerma strength simulations were performed with palladium loading of 20% and 80% and a rectangular distribution was assumed for the purposes of uncertainty determination. For the Monte Carlo predicted anisotropy data, uncertainties similar to the RDF analog were observed expect for the palladium loading component. The variation due to palladium loading for the 2D anisotropy function can vary as much as 25% at deeper depths.

The uncertainty associated with measurements performed in phantom using TLD microcubes for CivaDot DRC analog determination is presented in Table 4.5. Typical University of Wisconsin Radiation Calibration Laboratory (UWRCL) uncertainties were assumed for this budget. For EBT3 film measurements, an uncertainty estimation is provided in Table 4.6. The Type A standard deviation of various regions of interest during data analysis was within 1.5%. The source positioning uncertainty for the measurements was estimated to be within ± 50 μm. The positioning uncertainty for the EBT3 film and TLD measurements was estimated to be within ± 100 μm. The associated uncertainties were calculated using relevant Monte Carlo simulations of the measurement setup and reported in the uncertainty budget of the respective measurements.

Table 4.4: Uncertainty budget for Monte Carlo predicted CivaDot TG-43 analog parameters.

	Dose rate constant analog		Radial dose function analog	
Uncertainty parameter	Type A	Type B	Type A	Type B
Palladium loading		2.93%		0.51%
Photon spectrum		0.01%		0.01%
MCNP6 code physics		0.10%		0.14%
μ_{en} / ρ for dose determination		0.87%		1.23%
μ / ρ for photon attenuation		0.31%		0.44%
Tally statistics	1.00%		1.41%	
Quadratic sum	1.00%	3.07%	1.41%	1.41%
Total standard uncertainty	3.23%		2.00%	

Table 4.5: Uncertainty budget for CivaDot dose rate constant analog measurement using TLD microcubes.

Uncertainty parameter	Type A	Type B
TLD reproducibility	2.00%	
TLD positioning		1.5%
Source positioning		1.00%
Cobalt-60 air kerma rate		0.73%
CivaDot UW S_{K}	0.5%	1.78%
TLD intrinsic energy correction		2.90%
TLD calibration		2.00%
μ_{en}/ρ for corrections		1.23%
μ/ρ for corrections		0.44%
Quadratic sum	2.06%	4.59%
Total standard uncertainty	5.03%	

Table 4.6: Uncertainty budget for CivaDot EBT3 film measurements.

Uncertainty parameter	Type A	Type B
Film ROI scanner standard deviation	1.50%	
Scanner and film uniformity		0.60%
Source positioning		1.00%
UW40-M x-ray air kerma rate		0.45%
CivaDot UW S_{K}	0.5%	1.78%
Film positioning		1.20%
Film intrinsic energy correction		2.30%
Film calibration		1.90%
μ_{en}/ρ for corrections		1.23%
μ/ρ for corrections		0.44%
Quadratic sum	1.58%	4.10%
Total standard uncertainty	4.39%	

4.7 Conclusions

Dose distribution measurements of the CivaDot performed using TLD microcubes and EBT3 films in a PMMA phantom demonstrated good overall agreement with Monte Carlo predicted dose distributions, given the uncertainties. The presence of gold shield x-ray fluorescence was observed in the source energy spectrum and its impact on various aspects of this investigation was evaluated. EBT3 film (expiration dates — 2015, 2016, 2017) was demonstrated as a viable dosimeter for the characterization of a low-energy photon-emitting brachytherapy source.

Chapter 5

Dosimetric characterization of a directional brachytherapy source array

5.1 Introduction

The dosimetry of conventional LDR (^{125}I, ^{103}Pd, and ^{131}Cs) source arrays is performed by the calibration and characterization of the individual elements of the array (Colonias et al. 2011, Yang and Rivard 2011), according to the methods prescribed by the AAPM TG-43 report. (Nath et al. 1995, Rivard et al. 2004; 2007) Source strength for an element can be determined individually using a NIST-traceable well-type ionization chamber. Dose to water calculations can then be performed by using published TG-43U1 data for the source. Dosimetric superposition of all the elements in the array is performed and a dose lookup table is formulated. (Johnson et al. 2007) This work follows a similar element-based (CivaDot) approach for dosimetric characterization for the CivaSheet array. In the previous chapter, the dosimetric characterization of an element (CivaDot) was detailed. This chapter

focuses on the determination of the dose distribution of an entire array (CivaSheet) and verification of the element-based approach.

The dose distribution of the CivaSheet was determined using measurements and Monte Carlo calculations. Measurements of two 6×6 CivaSheet arrays was performed in-phantom using a stack of EBT3 films. The suitability of EBT3 films as a dosimeter for this work was demonstrated in the previous chapter. Monte Carlo simulations of the measurement setup were performed using the MCNP6 code. An investigation into the variability of the CivaDots present in a CivaSheet array was also conducted.

5.2 Methodology

Dose distribution measurements of a CivaSheet (6×6 array of CivaDots) were performed in a custom PMMA phantom. An EBT3 film stack was used for this in-phantom measurement. EBT3 films were placed at multiple depths — 0.5 cm, 1 cm, 2 cm, 3 cm, 4 cm, 5 cm from the hot side of the source, and 1 cm from the cold side of the source. Three film measurements each were performed at the 0.5 cm and 1 cm depth (hot side), and two measurements were performed for all the other depths. Figure 5.1 is an illustration of the measurement setup using seven EBT3 films placed at different depths. The CivaSheet source was secured in additional pieces of EBT3 film (used only as a holder not for measurement) with holes laser cut to accommodate the individual CivaDots. The films were read out using an EPSON 10000XL flatbed scanner. A calibration curve was determined for the film measurements by irradiating additional films using the NIST-matched UW40-M x-ray beam (effective energy: 19.2 keV, 40 kVp) and following the procedure reported in the previous chapter. Based on the findings of Morrison et al. and Chiu-Tsao et al., the intrinsic-energy correction value for these measurements was assumed to be unity. (H.Morrison et al. 2014, Chiu-Tsao et al. 2014) The post-scanning analysis was performed using the MATLAB software.

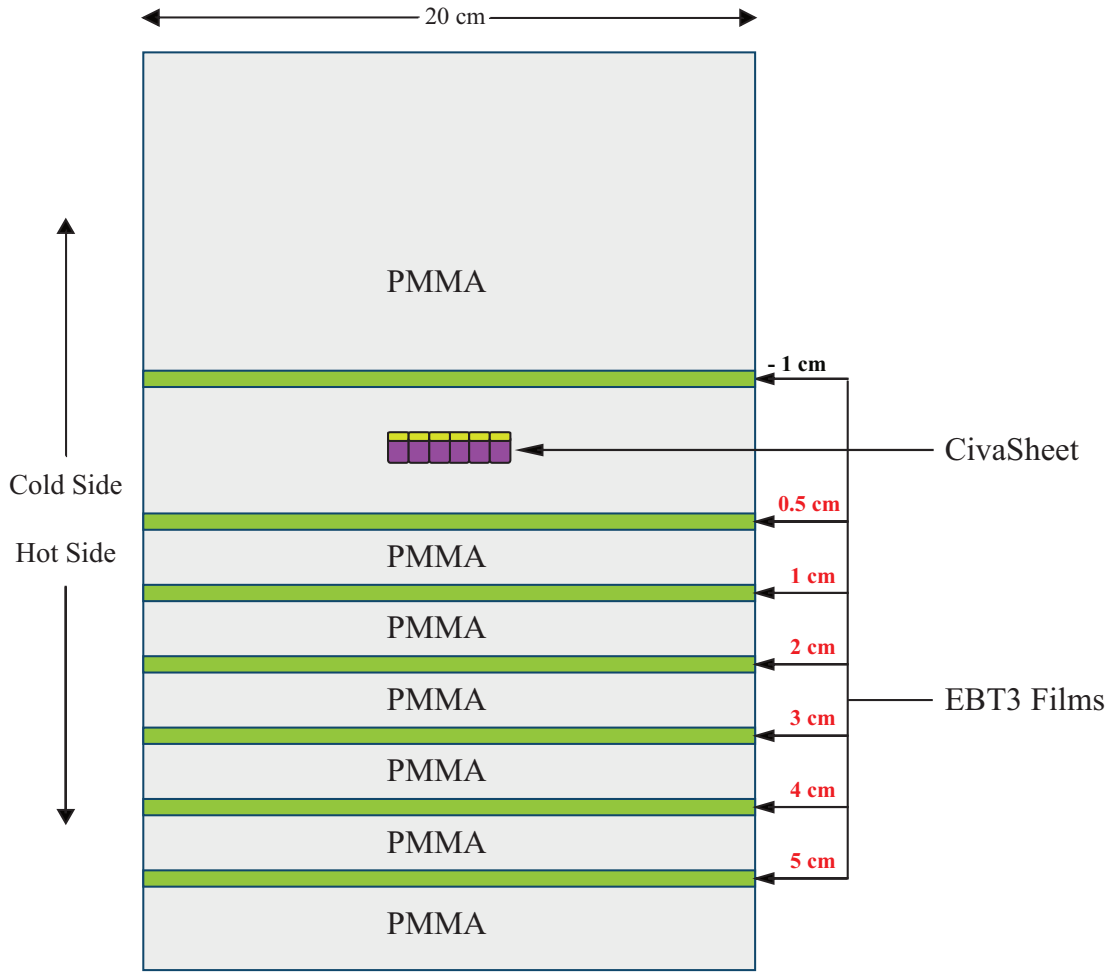

Figure 5.1: An illustration of the PMMA film stack phantom setup for the CivaDot dose distribution measurements using seven EBT3 films placed at different depths on the source cylindrical axis.

Individual CivaDots were cropped from the CivaSheet array following the completion of the dose measurements. Each CivaDot was measured in a Standard Imaging HDR1000 Plus well-type ionization chamber calibrated at the UWADCL, traceable to the NIST air-kerma strength standard for the CivaDot. Two additional CivaDot sources (from the same batch as the CivaSheet source) provided by CivaTech Oncology were also measured using the well chamber. Primary air-kerma strength of these two sources was measured using the UW VAFAC for comparison to the well chamber measurement results. The consistency of the CivaDot source strength for the batch was also assessed.

5.2.1 Monte Carlo simulations

A 6×6 CivaSheet was modeled using MCNP6 code based on the specifications provided by CivaTech Oncology, Inc. The details of the CivaSheet structure and individual CivaDot geometry are provided in Chapter 2. The updated low-energy photon cross section data library (mcplib12) was used for the MC simulations. The *f4 tally was used for absorbed-dose calculations, with energy fluence modified by μ_{en}/ρ values. A modified *fmesh4 tally was used for calculating the planar dose distribution. A minimum of 10^9 histories were used for each simulation. Photon mass-energy absorption cross-sections of various materials were used from the NIST XCOM database. (Berger et al. 2005) The photon transport cut off was set to 100 eV. No electron transport was simulated. All Monte Carlo simulations for this work assumed a palladium loading of 50%. The following geometries were simulated:

1. A CivaSheet consisting of a 6×6 array of CivaDots in a water phantom
2. A CivaSheet consisting of a 6×6 array of CivaDots in the PMMA phantom with an EBT3 film stack setup
3. A single CivaDot in a water phantom

The individual CivaDot source strength for the CivaSheet MC simulations were scaled in accordance with the results of the well chamber measurements. This involved scaling the probability of a particle starting in a given CivaDot source in the CivaSheet MC simulations to its measured source strength relative to the batch average. The CivaSheet simulations were first used to generate phantom and detector correction factors to convert the measured dose in-phantom to dose to water values. The absolute measured doses at different depths were compared to the MC predicted dose distributions at the corresponding depths. This comparison was performed using a dose difference map, whereby each pixel of the simulated CivaSheet dose distribution was subtracted from the measured CivaSheet dose distribution. The CivaDot water phantom MC simulation was used to generate a MC predicted dose superposition distribution. This was performed by the superposition of the MC-calculated dose distributions of the individual CivaDots, scaled to their relative measured source strengths for different depths.

5.3 Results

5.3.1 CivaSheet dose distribution measurements and comparison to Monte Carlo simulations

Figure 5.2 presents the CivaSheet (6×6 array) dose distribution at 0.5 cm depth (hot side) predicted using MC simulations. The 2-D dose distribution measured using the EBT3 film-stack phantom at this depth is presented in Figure 5.3. A total of three sets of measurements were performed at this depth. Each set of measurement was an independent in-phantom irradiation of the EBT3 film. Both the dose distributions were normalized to the value of a square region-of-interest of 0.5 mm set around the center of the CivaSheet MC distribution. The normalization point lies in a valley, i.e., there is no CivaDot sources directly above it. Hot spots are observed at the lateral positions directly underneath a source in

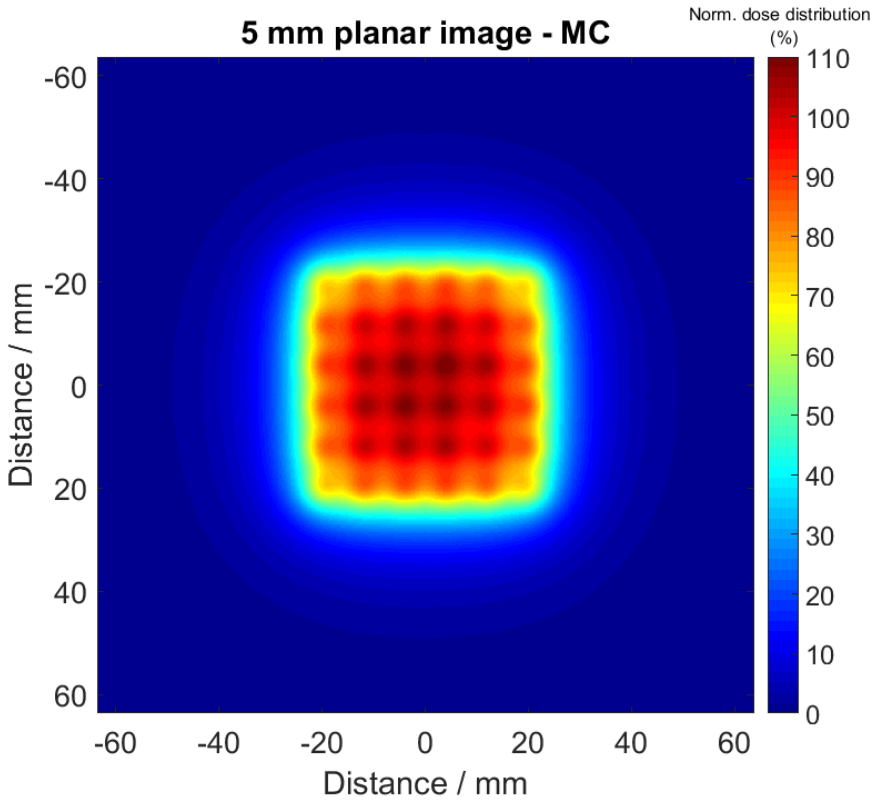

Figure 5.2: Normalized dose distributions of the CivaSheet (6×6 array) at 0.5 cm depth (hot side) using MCNP6 simulations.

both the measured and simulated distributions. The hot spots are further validated by the profiles provided in Figures 5.4, 5.5. These figures present the x-axis and the y-axis profiles of the MC predicted dose distribution, the dose distribution measured using three sets of measurements and the superimposed MC CivaDot dose distributions. Good agreement was observed between the profiles of the various distributions. The dose fall-off to 80% was observed around ±2 cm from the source cylindrical axis at the 0.5 cm depth.

The dose difference map (pixel-by-pixel subtraction) of the average measured dose distribution and the CivaSheet MC simulations is shown in Figure 5.6a. The differences observed between the distributions were generally within ±3% with maximum differences up to 6%. Similar results were observed for the dose difference map of the measured dose distribution

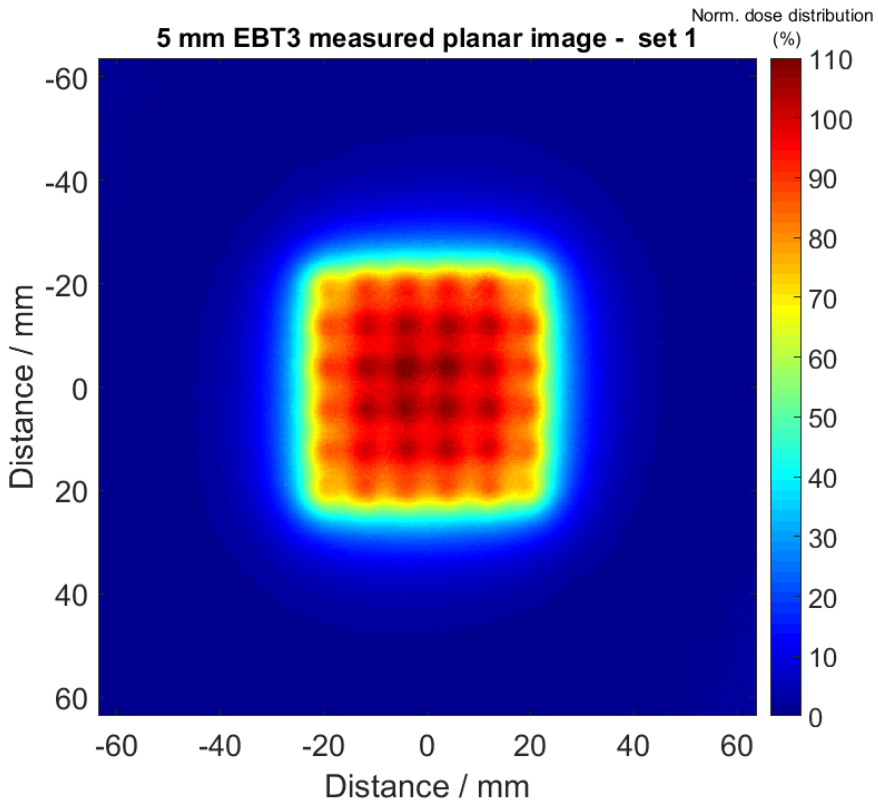

Figure 5.3: Normalized dose distributions of the CivaSheet (6×6 array) at 0.5 cm depth (hot side) measured using the EBT3 film stack setup.

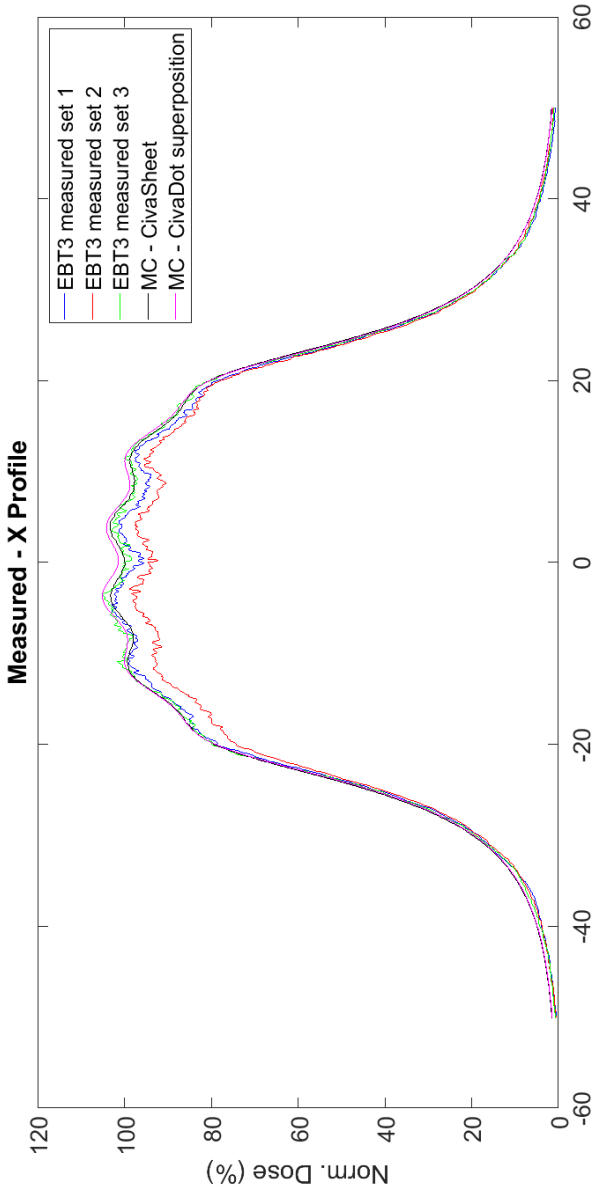

Figure 5.4: Measured and simulated profiles of the CivaSheet (6×6 array) at 0.5 cm depth (hot side) on the x-axis.

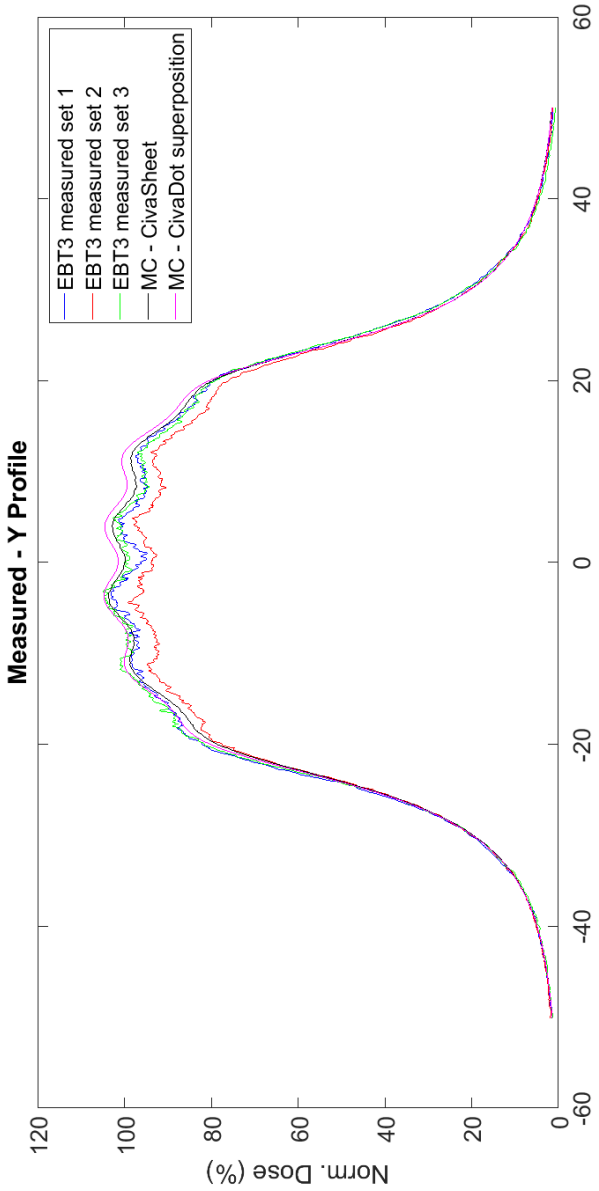

Figure 5.5: Measured and simulated profiles of the CivaSheet (6×6 array) at 0.5 cm depth (hot side) on the y-axis.

and the CivaDot MC superposition dose distribution as seen in Figure 5.6b, with some additional hot spots present. Figure 5.6c presents the results of the difference between the CivaDot MC dose superposition distribution scaled according to the respective CivaDot source strength measured with the well chamber and no scaling (all sources have equal strength). Maximum differences up to +1.4% and -1.6% were observed between the scaling and no scaling distributions. This provides an estimate of the error associated with assuming that CivaDots had equal source strength.

A similar analysis was performed for the 1 cm depth (hot side), the results of which are presented in Figures 5.7a, 5.7b, 5.8a, and 5.8b. A total of three sets of measurement were performed at this depth. Figures 5.7a, 5.7b show the MC predicted and the measured CivaSheet dose distribution, both normalized to the MC central ROI at 1 cm depth. As seen in the figures, there are no hot spots corresponding to the sources as observed in the 0.5 cm depth distributions. The source field-of-view widens and the contribution of scatter increases at this depth. This is also evident in the profiles provided in Figures 5.8a and 5.8b. Good agreement was observed between the profiles of the various distributions. The dose fall-off to 80% was observed around ±2 cm from the source cylindrical axis at the 1 cm depth. The dose difference map of the average measured dose distribution and the CivaSheet MC simulations is shown in Figure 5.9a. The differences observed between the distributions were generally within ±2% with maximum differences up to 4%. Similar results were observed for the dose difference map of the measured dose distribution and the CivaDot MC superposition dose distribution as seen in Figure 5.9b.

Table 5.1 presents the results of the percent depth dose (PDD) determined at various depths using the EBT3 film stack setup measurements, the CivaSheet MC simulations, and the CivaDot MC superposition. PDDs were evaluated on the CivaSheet cylindrical axis (valley). The measured PDD agreed to within 2.2% of the CivaSheet MC calculated PDD and to within 2.3% of the CivaDot MC superposition calculated PDD at the 1 cm depth

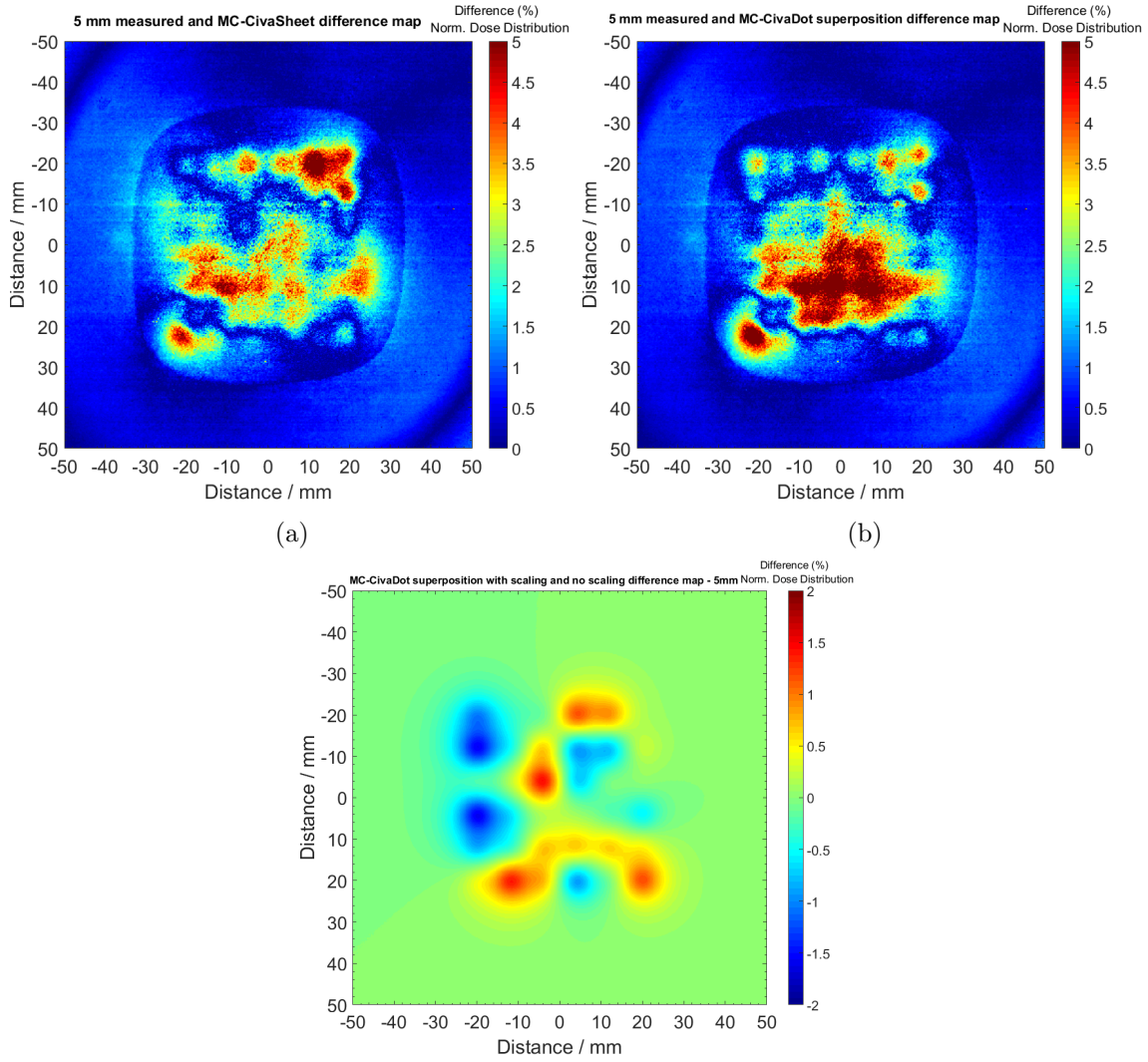

Figure 5.6: Dose difference maps of the CivaSheet (6×6 array) measured dose distribution at 0.5 cm depth (hot side) and: a. MC predicted, b. CivaDot MC dose superposition. c. Dose difference maps of the scaled CivaDot MC dose superposition distribution and the no scaling CivaDot MC dose superposition distribution.

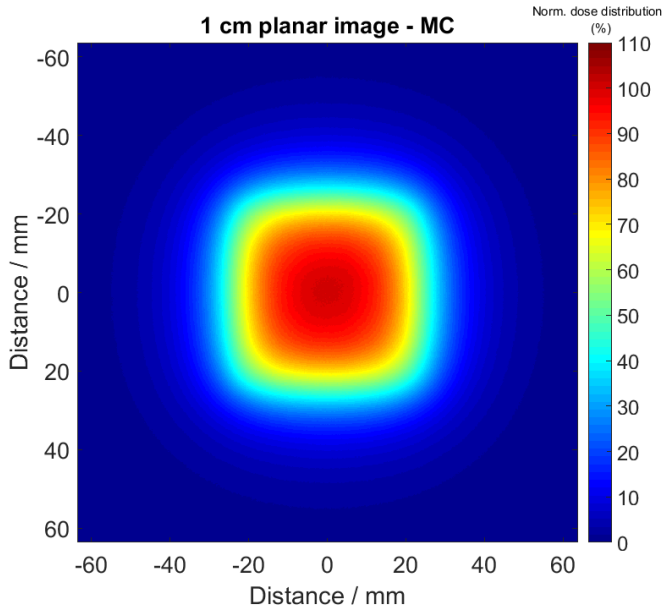

(a)

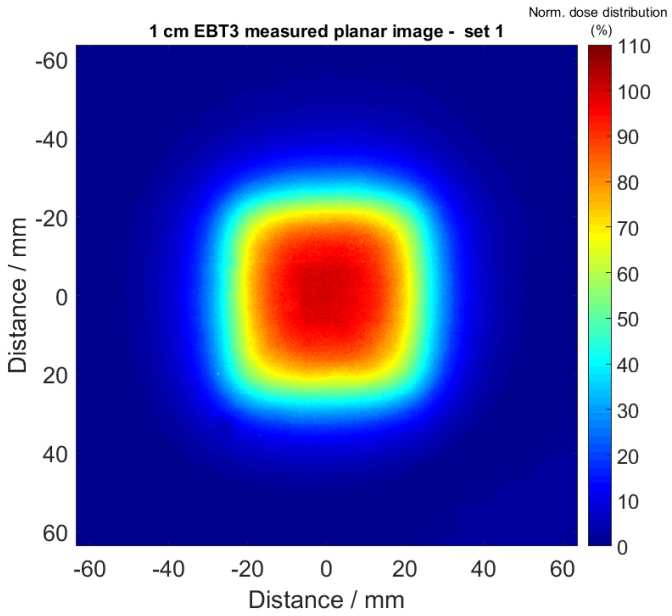

(b)

Figure 5.7: Normalized dose distributions of the CivaSheet (6×6 array) at 1 cm depth (hot side): a. MC predicted, b. Measured using EBT3 film stack setup.

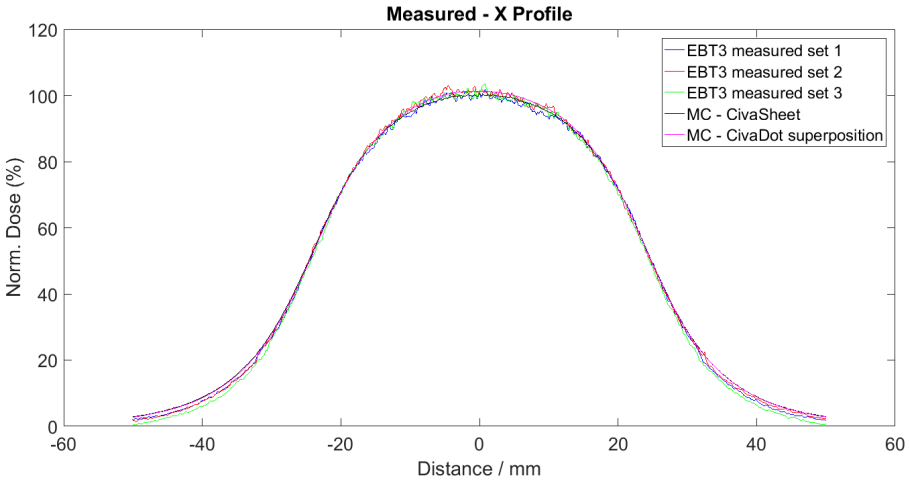

(a)

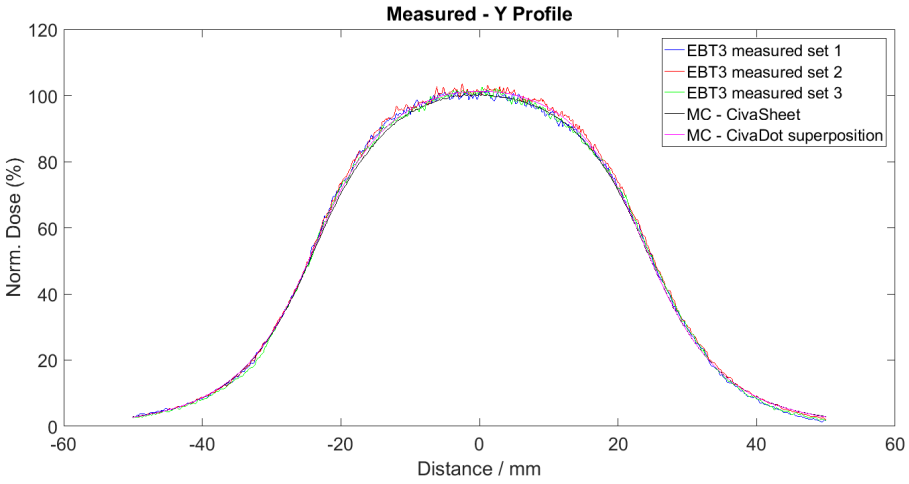

(b)

Figure 5.8: Measured and simulated profiles of the CivaSheet (6×6 array) at 1 cm depth (hot side): a. x-axis, b.y-axis..

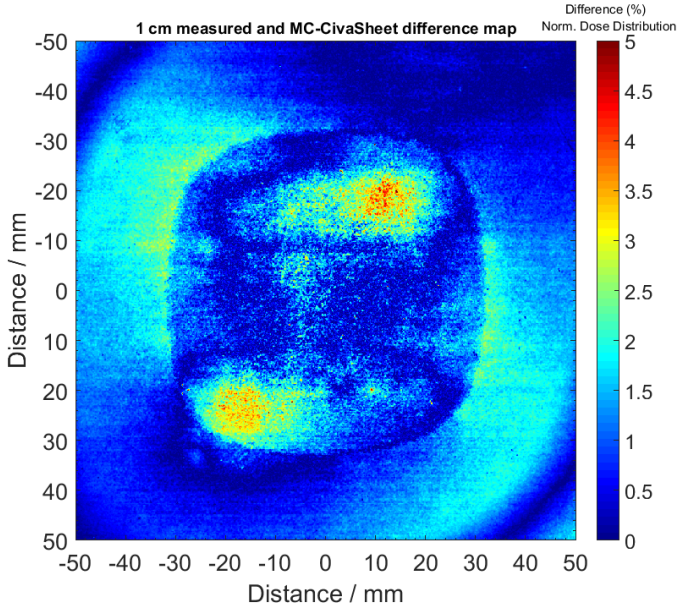

(a)

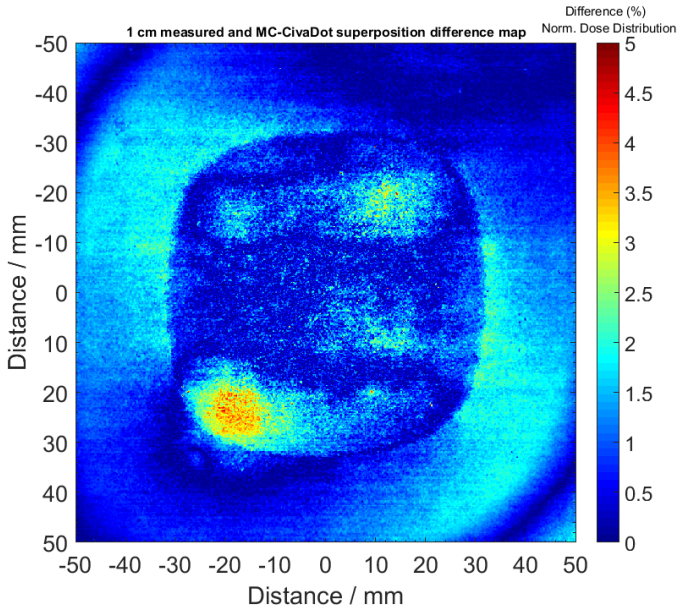

(b)

Figure 5.9: Dose difference maps of the measured CivaSheet (6×6 array) dose distribution at 1 cm depth (hot side) and: a. MC predicted, b. CivaDot MC dose superposition.

(hot side) and within 0.8% for all the other depths. The relative ratio of doses at shallow depths (0.5, 1, 2 cm) and 5 cm was within 5%. At 3, 4 cm (hot side) depths and the 1 cm (cold side) depth slightly large differences were observed, all of which were within 20% relative difference.

Figure 5.10 presents the MCNP6 calculated in-phantom PDD profiles of a 6×6 CivaSheet array assessed under the central valley, a central CivaDot source, and a peripheral CivaDot source. The individual PDDs were normalized to the 0.5 cm value on the source central axis (valley). As seen in the figure, PDD directly underneath a central CivaDot source and the valley is in good agreement after a depth of 0.7 cm on the hot side of the device. At shallower depths, both the peripheral source and central source have a higher dose since the contribution of scatter is minimal. As the source field-of-view widens and the contribution of scatter increases, the dose directly underneath the peripheral source significantly decreases compared to the other two PDD distributions.

5.3.2 Well chamber measurements

After the completion of the dose measurements of the CivaSheet, individual CivaDots were cropped from the array. The CivaDots were then measured using a NIST-traceable Standard Imaging HDR1000 Plus well-type ionization chamber. Figure 5.11 shows the distribution of the well chamber ionization measurements of the individual CivaDots normalized to the CivaSheet batch average. As observed in the figure, the source strength of most of the CivaDots were within ±3% of the batch average with maximum differences up to 4.3%.

The variation of the ionization current for a given CivaDot as a function of angle within the well chamber is presented in Figure 5.12 for all CivaDot sources. A majority of the sources demonstrated variations to within ±1.5% with maximum differences of about ±2%. A comparison of the average CivaDot source strength measured using the well chamber was performed with the CivaTech Oncology provided calibration report for the CivaSheet source.

Table 5.1: Comparison of the average percent depth dose measured using EBT3 film stack, CivaSheet MC simulations and CivaDot MC superposition. The PDDs were calculated on the source central axis (valley) and normalized to their respective 0.5 cm depth value

r (cm)	EBT3 measured %	CivaSheet MC calculated %	CivaDot MC superposition %	Measured and CS MC difference %	Measured and CivaDot MC difference %
0.5	100.0%	100.0%	100.0%	–	–
1	52.4%	50.3%	50.1%	2.2%	2.3%
2	15.5%	14.9%	14.8%	0.6%	0.7%
3	5.7%	5.0%	5.0%	0.7%	0.8%
4	2.1%	1.8%	1.8%	0.3%	0.4%
5	0.7%	0.7%	0.7%	0.0%	0.0%
-1.0 (cold)	4.3%	3.7%	3.8%	0.6%	0.5%

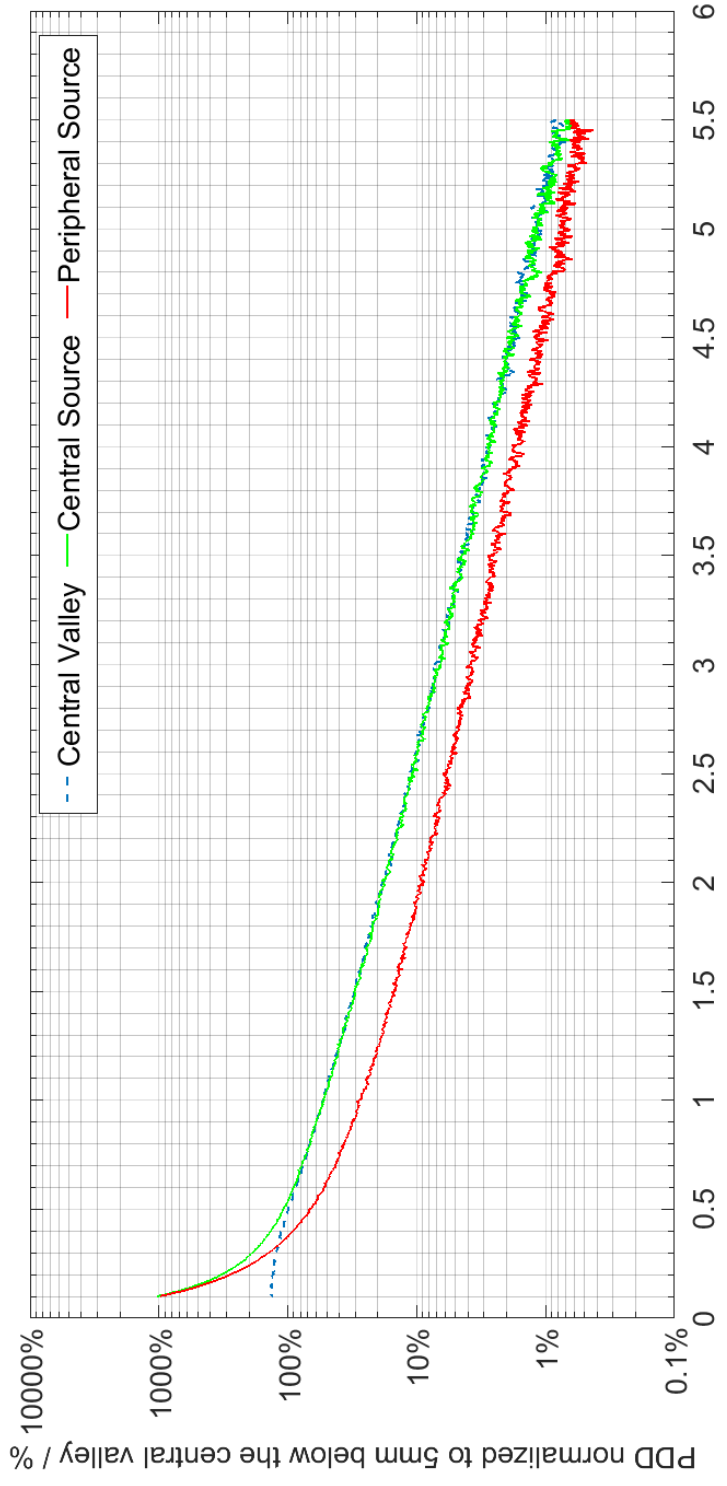

Figure 5.10: PDD profiles of a 6×6 CivaSheet array in-phantom predicted using MCNP6 simulations assessed under the central valley, a central CivaDot source, and a peripheral CivaDot source. All PDDs were normalized to the 0.5 cm value on the source central axis (valley).

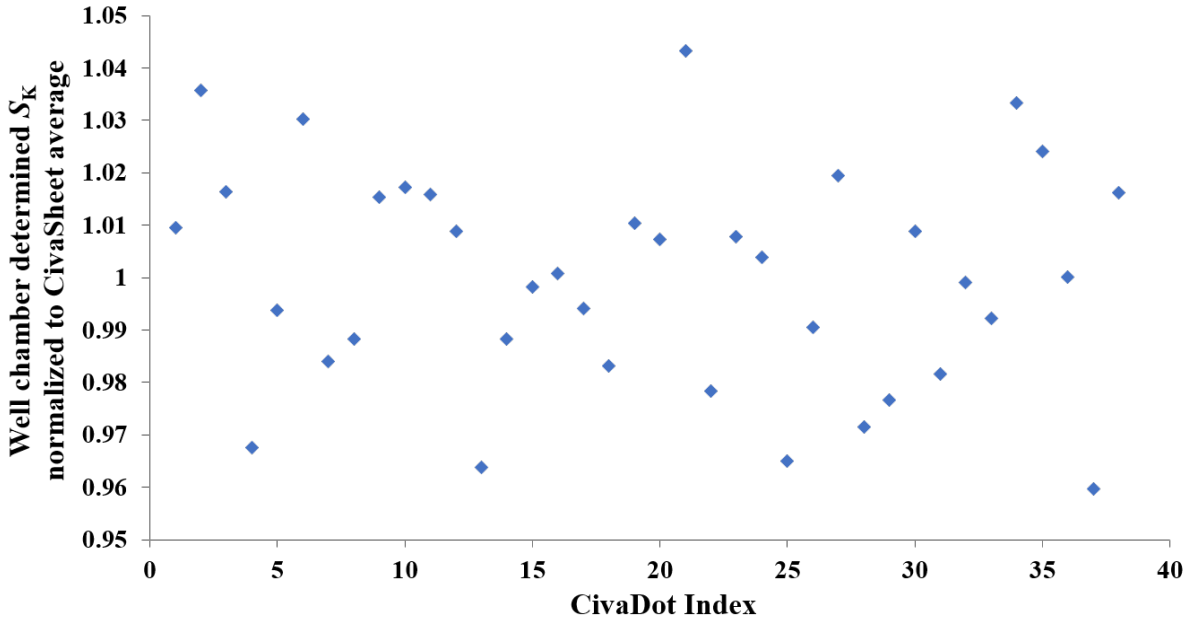

Figure 5.11: Results of the variation of the air-kerma strength determined for a CivaDot of the CivaSheet array using the HDR1000 Plus well chamber. The values for a given source were normalized to the batch average air-kerma strength value. The CivaDots constituting the CivaSheet are indexed one through 36, and the additional sources are labeled as 37 and 38.

CivaTech reported a batch average source strength of 4.598 U with a maximum of 4.764 U and a minimum of 4.410 U. The measured average air-kerma strength of the CivaDots using the well chamber was 4.661 U with a maximum of 4.862 U and a minimum of 4.473 U. The difference in the CivaTech reported and average measured air-kerma strength was -1.3%. A primary air-kerma strength measurement of the two additional CivaDot sources provided by CivaTech yielded values of 4.583 U and 4.844 U, which were +2.2% and +2.3% different from their well chamber determined air-kerma strength values, and -4.0%, +1.6% different from the CivaSheet batch average measured with the well chamber. This provides an estimate of the error associated with assuming the source strength of an element of an array is equal to the additional assayed source.

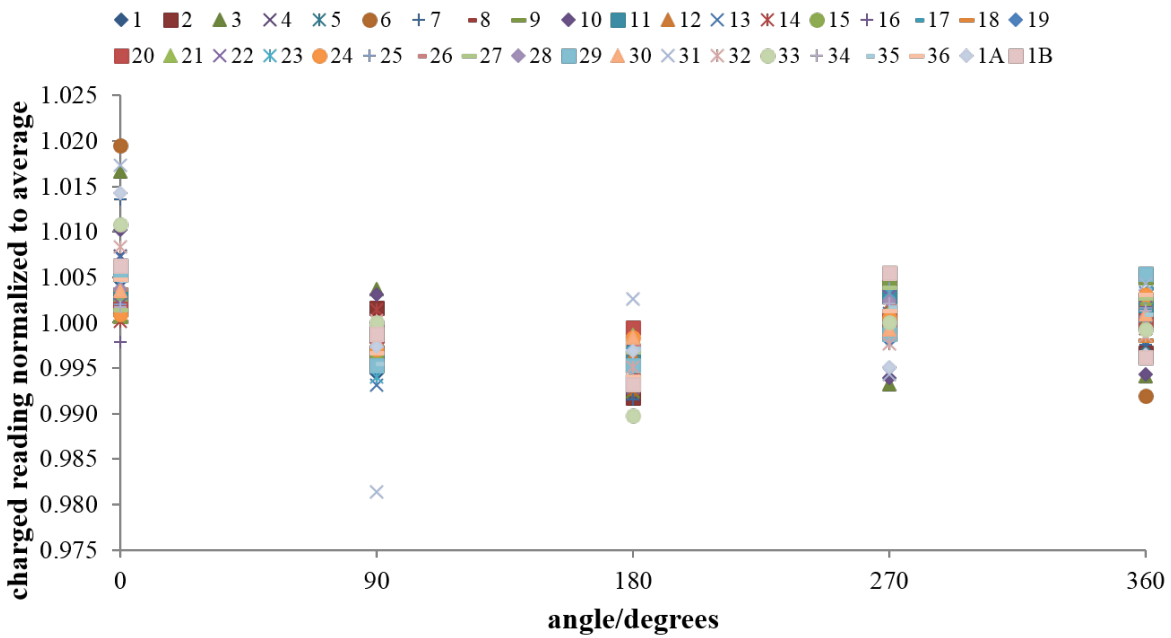

Figure 5.12: Results of the change in ionization current of a CivaDot within the HDR1000 Plus well chamber as a function of angle. The values for a given source were normalized to their respective average charge reading. The CivaDots constituting the CivaSheet array are indexed 1 through 36, and the additional sources are labeled as 1A and 1B.

5.4 Curvature of the CivaSheet

5.4.1 Introduction

The CivaSheet could potentially be used for the treatment of different malignancies, such as early stage non-small-cell lung cancer, head and neck cancer, ocular melanoma, soft tissue sarcoma among other sites. There are ongoing clinical trials for investigating its efficacy for pancreatic, abdomino-pelvic, and colorectal cancer treatments (trials NCT03109041, NCT02843945, NCT02902107). The pliable bioabsorbable membrane base provides the CivaSheet device with a degree of flexibility during clinical use. A need thus arises to investigate the impact of the curvature of the CivaSheet when used for a clinical treatment, especially for a permanent implant.

Figure 5.13 shows a computed tomography acquired scan of a patient implanted with the CivaSheet. As seen in the figure, the implanted CivaSheet device is curved significantly. The radius of curvature for the patient implant was estimated using Solidworks.^{TM} Taking into account the scaling factor of the CT image, a value of 48 mm was calculated for the radius of curvature.

Based on the premise of studying the impact of a curvature on the CivaSheet source, an investigation was performed using in-phantom EBT3 film measurements and Monte Carlo simulations.

5.4.2 Methodology

Dose distribution measurements of a second CivaSheet (6×6 array of CivaDots) were performed at the UWMRRC in a custom Virtual water^{TM} phantom. Figures 5.14 and 5.15 are the photographs of the second 6×6 CivaSheet source received from CivaTech Oncology. As seen in Figure 5.14, the gold shields of the CivaDot are clearly visible. Fenestrations are also seen in the photograph, which are present in the source for surgical implantation purposes. A mark was made on the CivaSheet source using an ink marker to keep the orientation

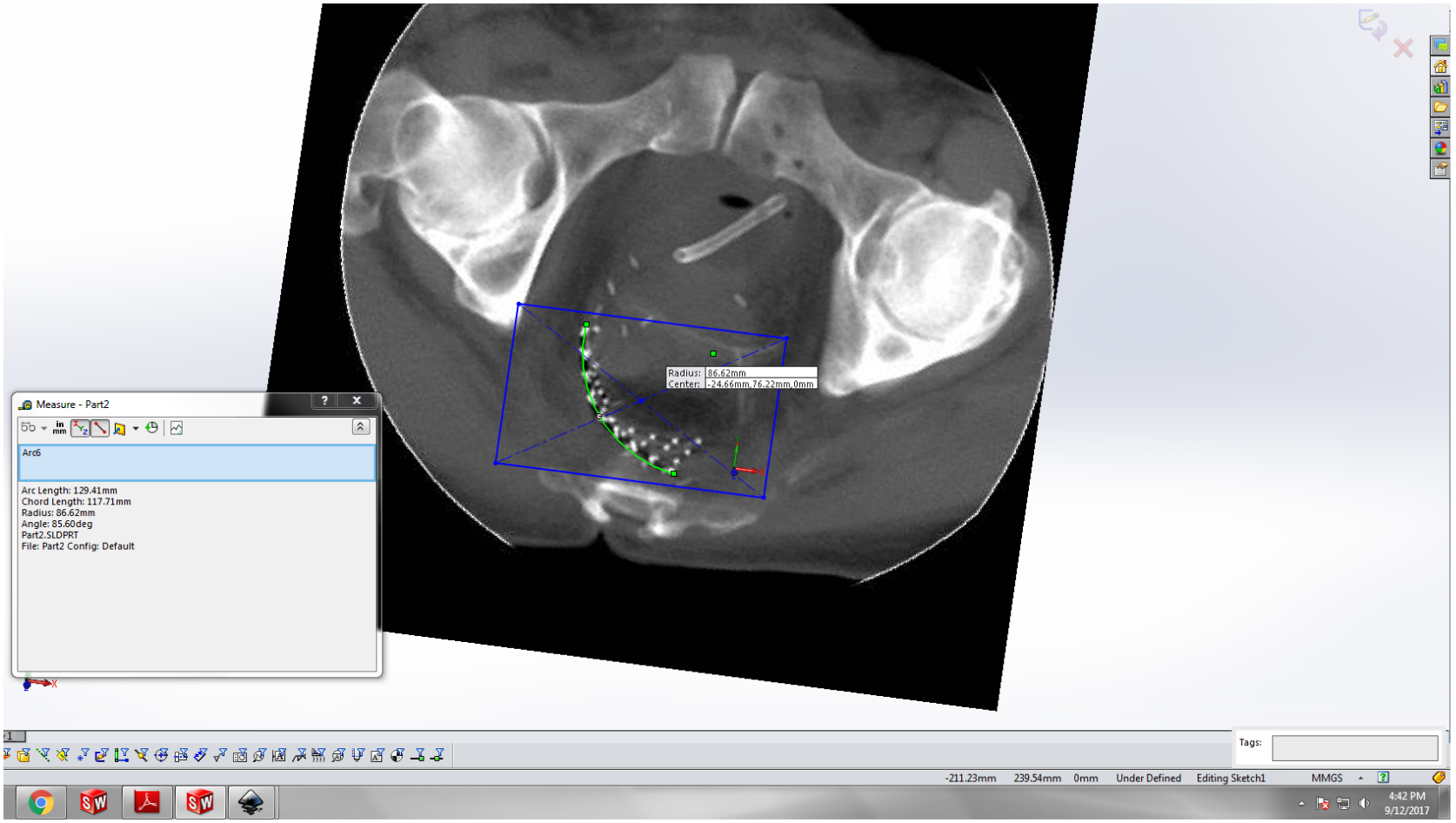

Figure 5.13: An acquired computed tomography image of a CivaSheet patient implant. Taking into account the scaling factor for the CT image, the radius of CivaSheet curvature for this implant was estimated to be 48 mm. [Imaged reproduced from personal communication, CivaTech Oncology Inc.]

of the source consistent throughout the investigation. Figure 5.15 is a photograph of the source with the hot side of the device facing outwards.

A new phantom was fabricated to accommodate a curved CivaSheet measurement for this source. Virtual water was used as the material of choice for the phantom. The complexity of the phantom design doesn't allow the use of a brittle plastic such as PMMA. Measurements were performed in-phantom using an EBT3 film stack. Films were placed at multiple depths ranging from 0.3 cm to 5 cm on the CivaSheet hot side, and 0.5 cm, 1 cm on the cold side of the source. Three film measurements were performed at the 0.3 cm to 1 cm depths and one measurement was performed for all the other depths.

An illustration of the measurement setup using thirteen EBT3 films placed at different depths is provided in Figure 5.16. The dimensions of the phantom are $20\times20\times20$ cm^3. Based on the information received from CivaTech Oncology about patient implants, the radius of curvature was set at 4 cm for the phantom. This is slightly smaller than the radius of curvature estimated for the patient implant as seen in Figure 5.13. Figure 5.17 is an illustration of the cross-sectional view of the curved virtual phantom slab. This component of the virtual water phantom was fabricated by slicing out a 4 cm radius cylinder from a slab and then using additional thin virtual water slabs that can be stacked in the cavity along with EBT3 films.

Three CivaSheet configurations were investigated with the virtual water phantom setup. The first was the CivaSheet in a flat configuration, i.e., no curvature is applied to the CivaSheet source. Secondly, the CivaSheet in a concave configuration, wherein the device is placed in the cavity of the curved component of the phantom with the hot side of the source pointing inwards to the curve. Finally, the CivaSheet in a convex configuration, wherein the device is placed in the cavity of the curved component of the phantom with the hot side of the source pointing outwards to the curve. Figures 5.18 and 5.19 are photographs of the curved component of the phantom. As seen in Figure 5.18, the CivaSheet is secured within

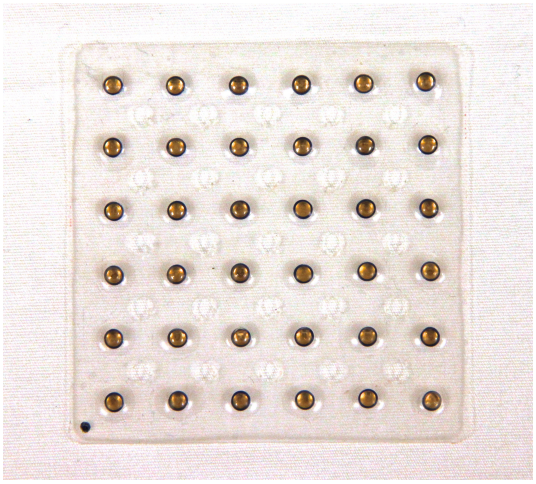

Figure 5.14: A photograph of the CivaSheet source used in this investigation comprising of 36 CivaDots. The cold side of the device is shown here with the CivaDot gold shields facing outwards.

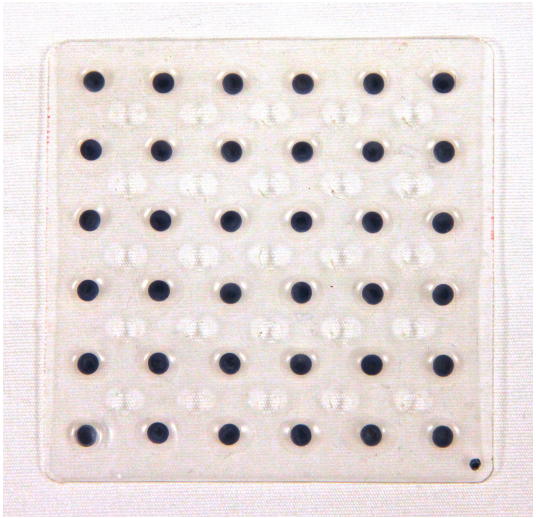

Figure 5.15: A photograph of the CivaSheet source used in this investigation comprising of 36 CivaDots. The hot side of the device is shown here.

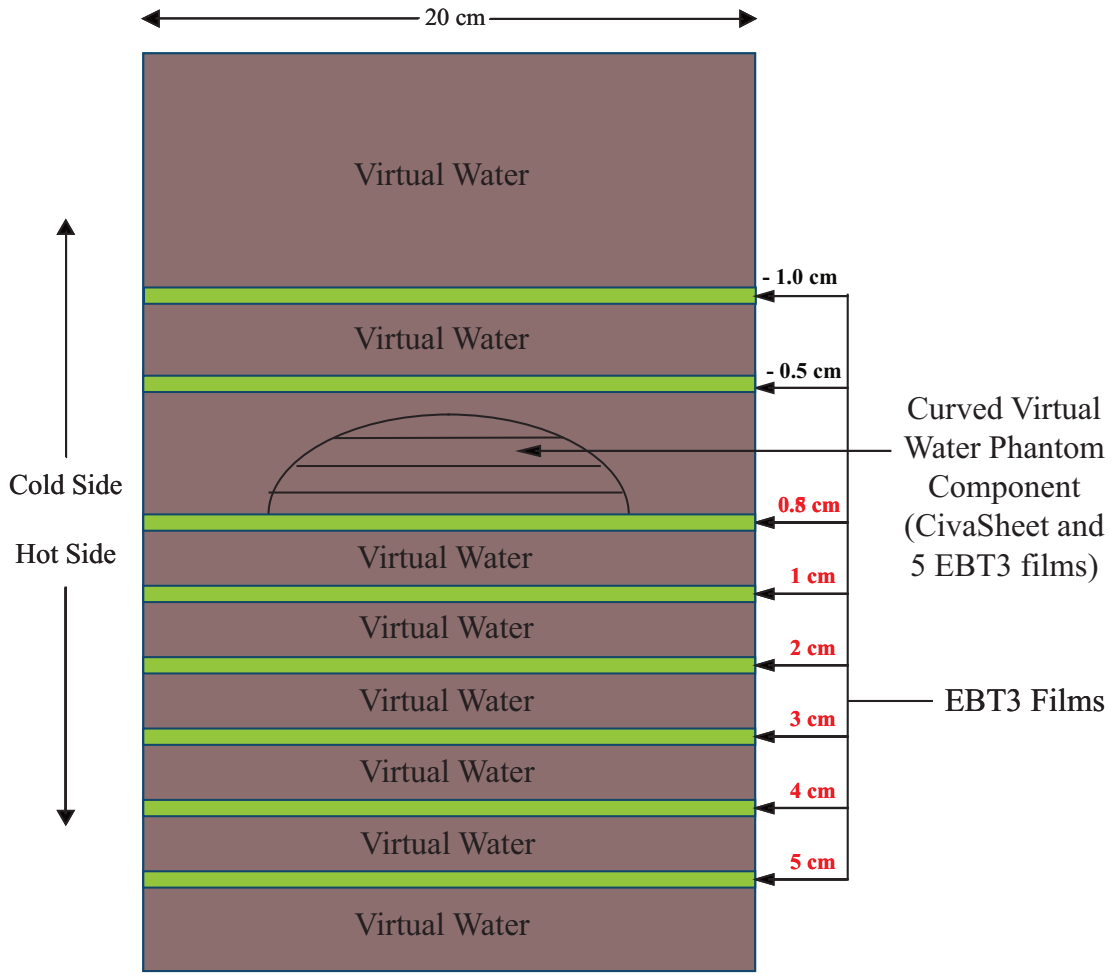

Figure 5.16: An illustration of the virtual water phantom used to measure the CivaSheet dose distribution with EBT3 films. This is a cross-sectional view of the phantom with the CivaSheet placed in the curved part of the phantom for convex and concave configurations.

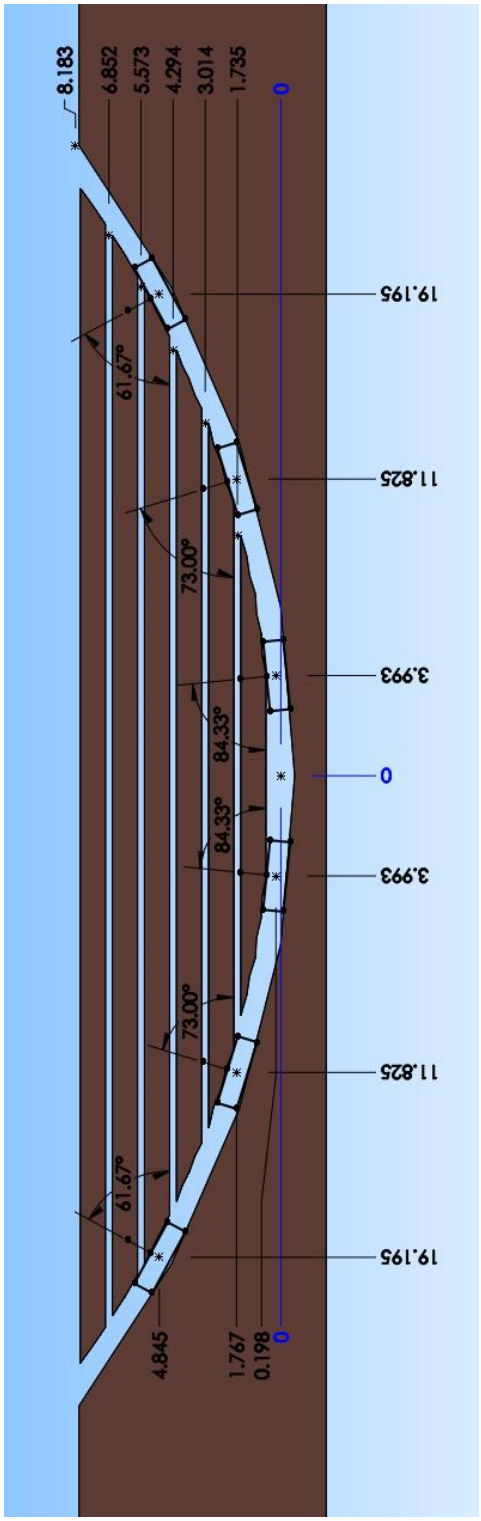

Figure 5.17: An illustration of the curved component of the virtual water phantom using Solidworks.™ This is a cross-sectional view of the phantom, with the CivaDots modeled (black boxes). All dimensions are in mm.

a teflon sheet holder with holes provided to accommodate the CivaDot sources. The hot side of the CivaSheet is pointing outwards from the curve, and hence corresponds to the convex configuration for the measurements. Figure 5.19 is a photograph of the CivaSheet in the curved phantom without the additional teflon sheet holder.

The films irradiated in-phantom were read out using an EPSON 10000XL flatbed scanner. A new calibration curve was determined for the film measurements by irradiating additional films using the NIST-matched UW40-M x-ray beam. The post-scan analysis was performed using the MATLAB software. Individual CivaDots were cropped from the CivaSheet array following the completion of the dose measurements. Each CivaDot was measured in a NIST-traceable well chamber, to assess the variability of the individual CivaDot source strength compared to the batch. A Monte Carlo calculated correction factor was applied to the measured data to round off the depth of measurement (to the nearest mm depth) for all three configurations.

5.4.2.1 Monte Carlo simulations

A 6×6 CivaSheet was modeled using the MCNP6 code. The updated low-energy photon cross section data library (mcplib12) was used for the MC simulations. The *f4 tally was used for absorbed-dose calculations, with energy fluence modified by μ_{en}/ρ values. A modified *fmesh4 tally was used for calculating the planar dose distribution. A minimum of 10^9 histories were used for each simulation. The photon transport cut off was set to 100 eV. No electron transport was simulated. All Monte Carlo simulations for this work assumed a palladium loading of 50%. The following geometries were simulated:

1. A CivaSheet array consisting of 6×6 CivaDots in a water phantom in a flat configuration

2. A CivaSheet array consisting of 6×6 CivaDots in a water phantom in a concave configuration

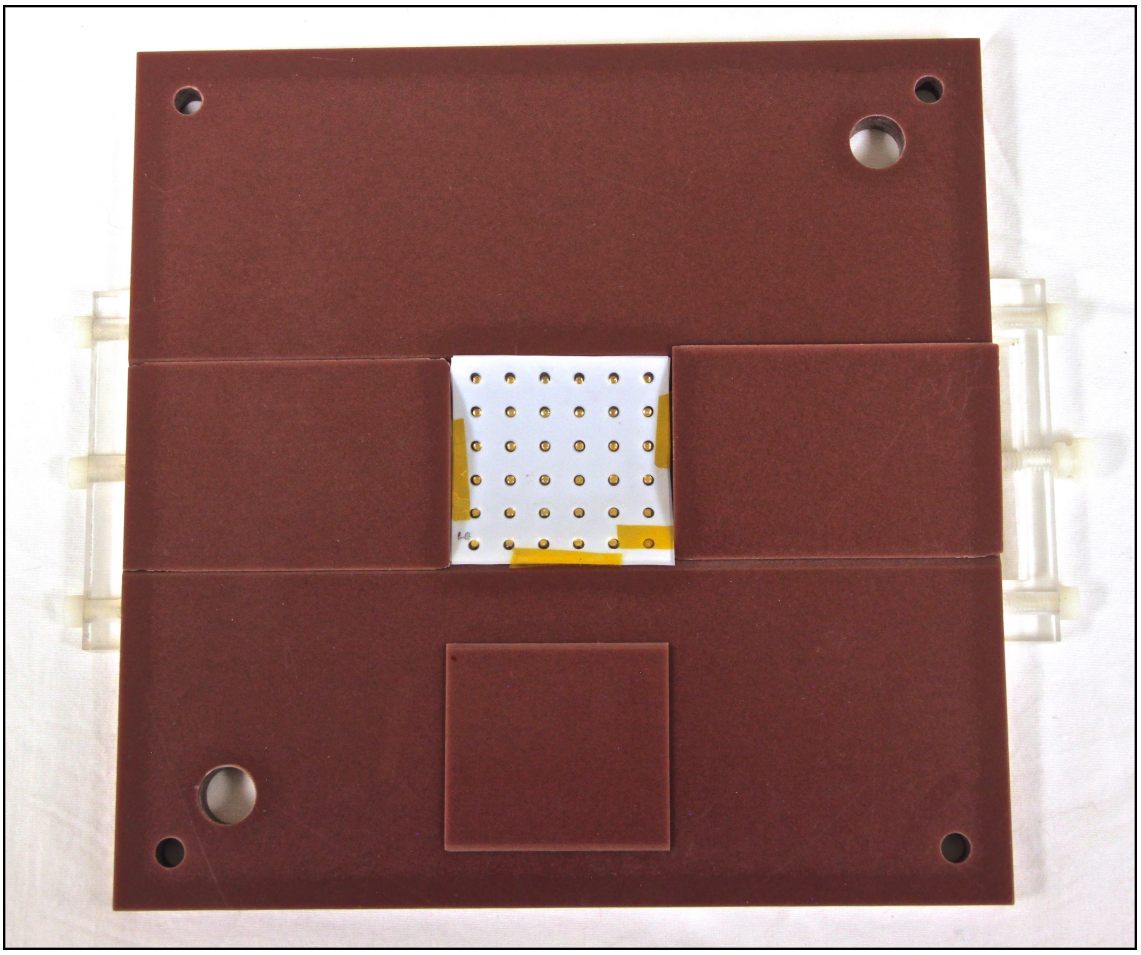

Figure 5.18: A photograph of the CivaSheet source in the curved virtual water phantom holder. The source was held within a teflon sheet (white) holder. This CivaSheet positioning configuration corresponds to the convex configuration of this investigation. The radius of curvature of the phantom was 4 cm.

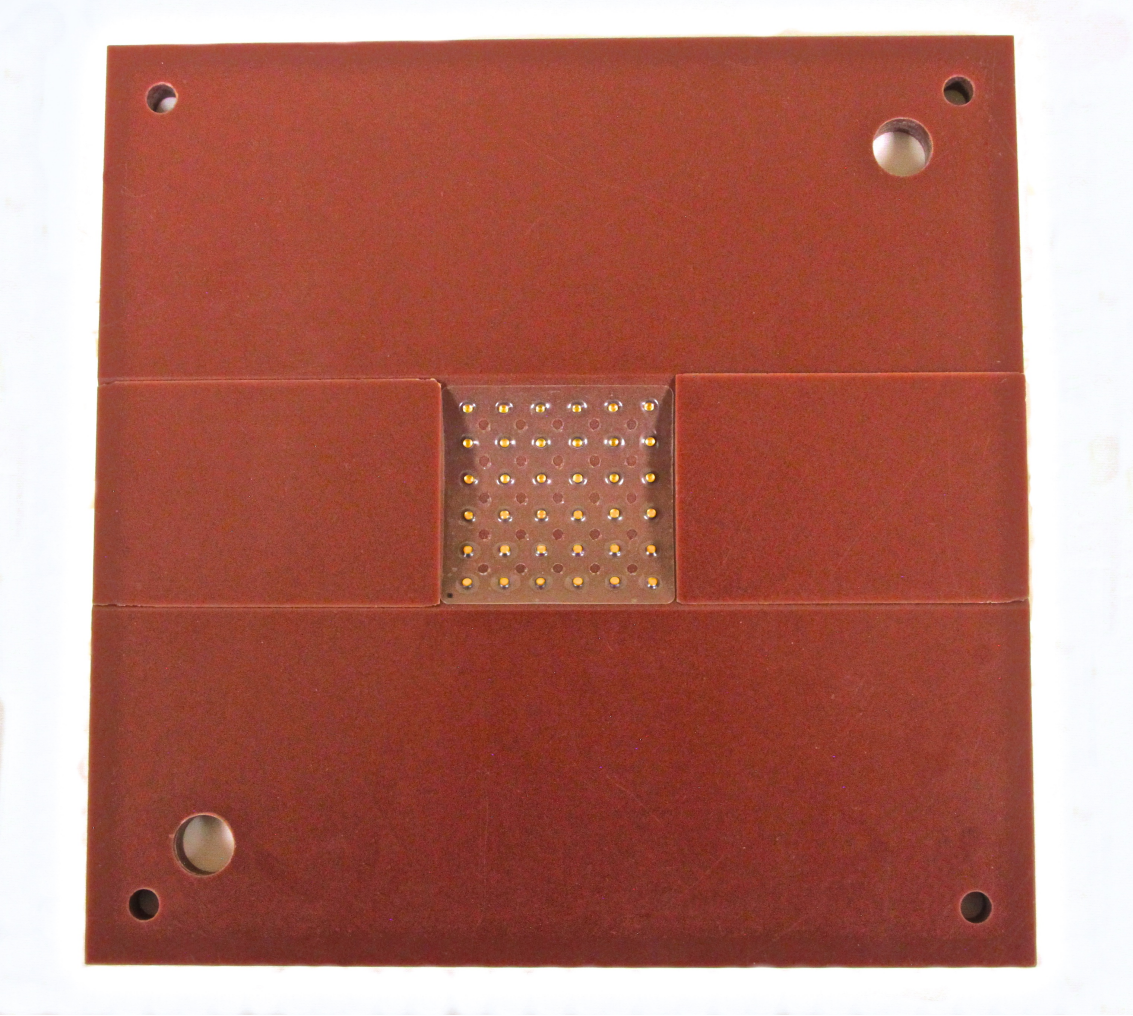

Figure 5.19: A photograph of the CivaSheet source in the curved virtual water phantom holder. The CivaSheet source is seen here without the teflon sheet holder.

3. A CivaSheet array consisting of 6×6 CivaDots in a water phantom in a convex configuration

4. A CivaSheet array consisting of 6×6 CivaDots in the virtual water phantom with an EBT3 film stack setup in a flat configuration

5. A CivaSheet array consisting of 6×6 CivaDots in the virtual water phantom with an EBT3 film stack setup in a concave configuration

6. A CivaSheet array consisting of 6×6 CivaDots in the virtual water phantom with an EBT3 film stack setup in a convex configuration

For the curved concave and convex CivaSheet configuration simulations, the CivaDot sources were rotated and translated according to the radius of CivaSheet curvature and phantom specifications. The individual CivaDot source strength for the CivaSheet MC simulations was scaled in accordance with the results of the well chamber measurements. The phantom and detector correction factors were generated using the MC simulations to convert the dose measured in-phantom to dose-to-water values. The absolute measured doses at different depths were compared to the MC predicted dose distributions at the corresponding depths.

Samples of the teflon sheet source holder and the virtual water phantom slabs were sent to ALS (Tucson, AZ) for chemical analysis. The chemical composition of these materials is taken into account in the MC simulations and can impact the phantom and detector correction factors. The results of the analysis are presented in Table 5.2.

5.4.3 Results

Figure 5.20 presents the PDD profiles of a 6×6 CivaSheet array predicted in water using MCNP6 simulations assessed under the CivaSheet central axis (valley), a central CivaDot source, and a peripheral CivaDot source for the flat source configuration. All PDDs were

Table 5.2: Results of the chemical analysis of the virtual water slab and teflon samples.

Material	Sample ID	Fluorine wt (%)	Carbon wt (%)	Hydrogen wt (%)	Nitrogen wt (%)	Oxygen wt (%)	Silicon wt (%)	Calcium wt (%)	Sodium wt (%)	Magnesium wt (%)
Virtual water sample 1	T1800403-001	-	67.79	8.51	2.28	17.70		2.28	0.14	0.02
Virtual water sample 2	T1800403-002	-	67.97	8.52	2.17	17.55		2.34	0.12	0.02
Teflon	T1800403-003	62.57	24.02	0.33	0.21	6.95	0.15	-	-	-

normalized to the 0.5 cm dose value on the source central axis (valley). Figures 5.21 and 5.22 present the PDD profiles for the concave and convex configuration respectively. When comparing the concave configuration to the flat configuration, there is a noticeable increase in the initial depth dose curve of the peripheral CivaDot distribution. This is expected as the peripheral CivaDot sources curve towards the hot side in the CivaSheet concave configuration. Similarly, there is a noticeable decrease initially when comparing the convex configuration to the flat configuration as the peripheral CivaDot sources curve away from the hot side of the CivaSheet in this configuration. The central CivaDot and Valley PDDs look similar for all three configurations. To evaluate this further, the CivaSheet central axis (valley) dose distribution of the three configurations was compared. All three distributions were normalized to the 0.5 cm valley value of the flat configuration. The results are shown in Figure 5.23. The concave configuration PDD is larger than the flat configuration and the convex PDD is smaller. This is expected as the impact of scatter contribution from the peripheral CivaDot sources on the dose distribution is increased for the concave configuration as the peripheral CivaDot sources curve towards the hot side of the device. The converse is true for the convex configuration. The scatter contribution to the dose distribution diminishes for this configuration as the peripheral CivaDot sources curve away from the hot side of the CivaSheet. The Monte Carlo calculated ratio of the tally dose value at the 0.5 cm depth on the source cylindrical axis (valley) of the concave configuration to the flat configuration is 1.08. For the convex configuration, this ratio is 0.93.

The 2-D dose distribution measured using the EBT3 filmstack phantom in the flat configuration at the 0.5 cm hot side depth of the device is presented in Figure 5.24. Hot spots corresponding to the CivaDot source location are observed. The dose distribution is similar to Figure 5.3. The measured dose distribution for the concave configuration at 0.5 cm depth hot side of the source is presented in Figure 5.25. There is a noticeable presence of the hot spots directly underneath the peripheral sources, as in this configuration, the

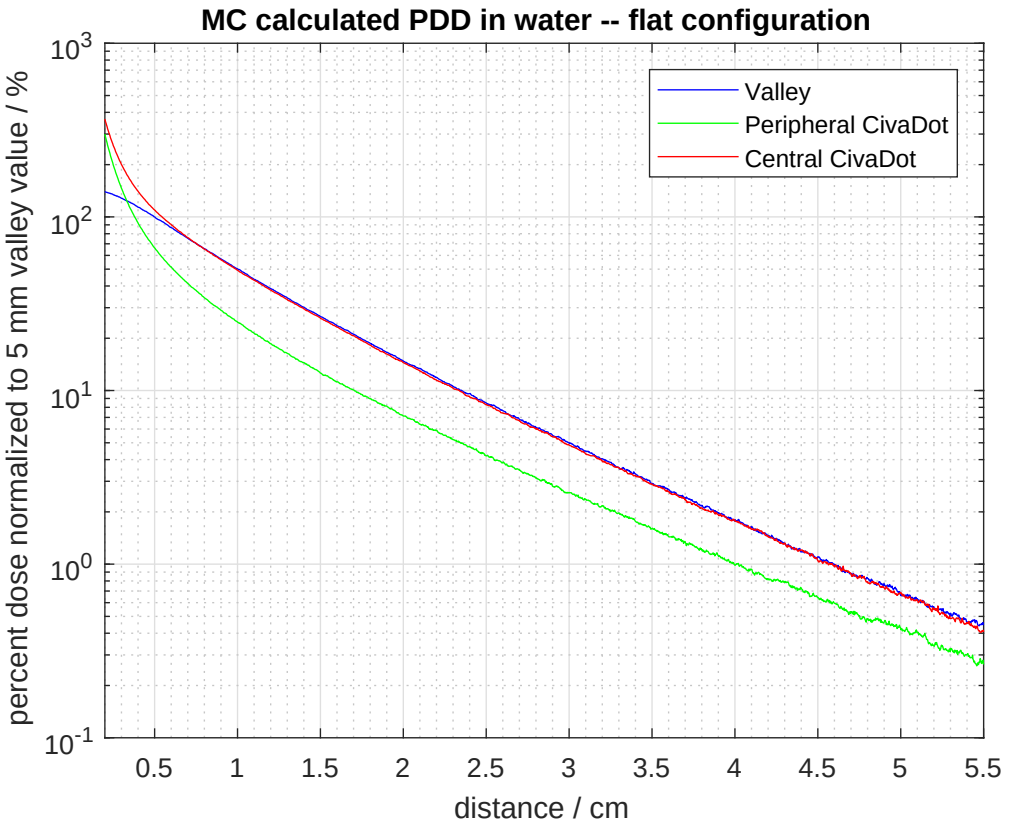

Figure 5.20: PDD profiles of a 6×6 CivaSheet array in water predicted using MCNP6 simulations assessed under the central valley, a central CivaDot source, and a peripheral CivaDot source for the flat source configuration. All PDDs were normalized to the 0.5 cm value on the source central axis (valley).

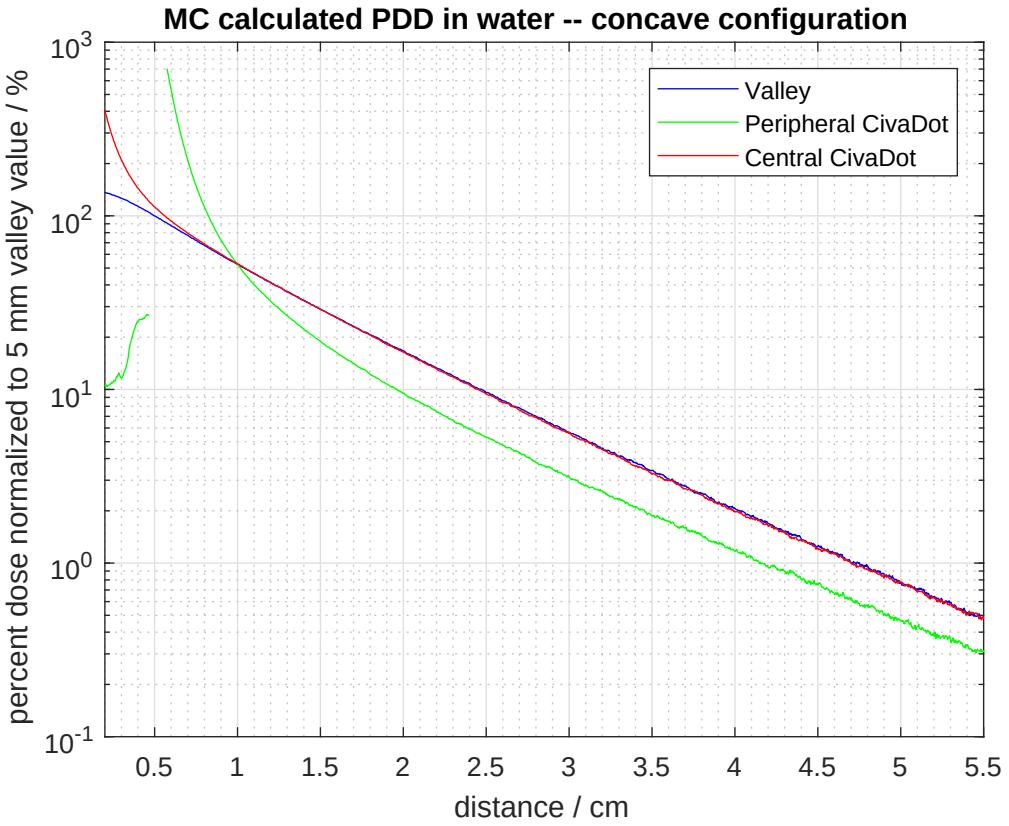

Figure 5.21: PDD profiles of a 6×6 CivaSheet array in water predicted using MCNP6 simulations assessed under the central valley, a central CivaDot source, and a peripheral CivaDot source for the concave source configuration. All PDDs were normalized to the 0.5 cm value on the source central axis (valley). The data where a CivaDot source was present (due to curvature) is omitted from the peripheral CivaDot PDD distribution.

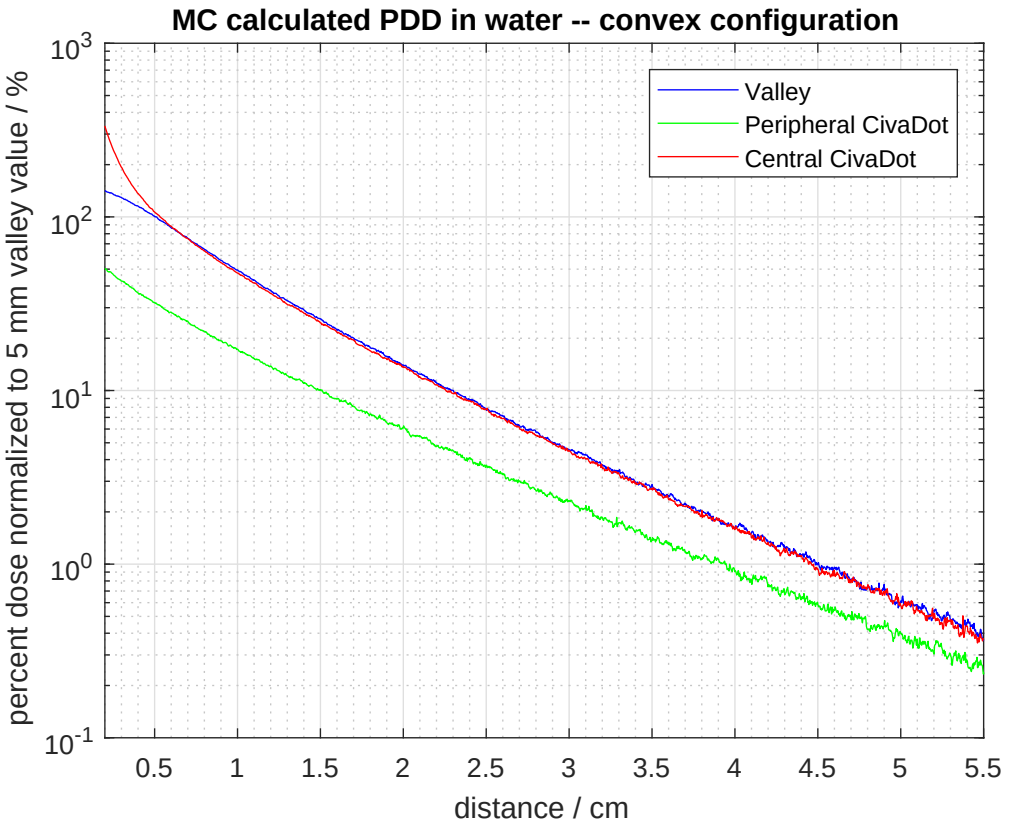

Figure 5.22: PDD profiles of a 6×6 CivaSheet array in water predicted using MCNP6 simulations assessed under the central valley, a central CivaDot source, and a peripheral CivaDot source for the convex source configuration. All PDDs were normalized to the 0.5 cm value on the source central axis (valley).

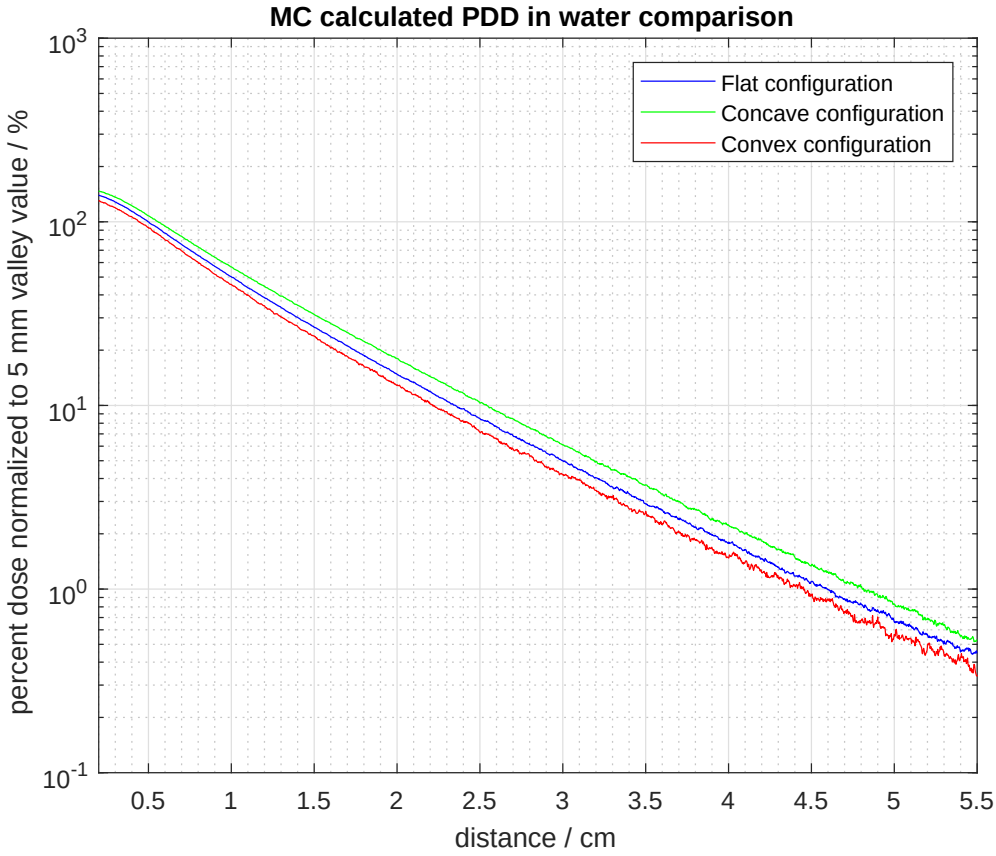

Figure 5.23: PDD profiles of a 6×6 CivaSheet array in water predicted using MCNP6 simulations assessed under the central valley for all three source configurations. All PDDs were normalized to the 0.5 cm value on the source central axis (valley) for the flat configuration.

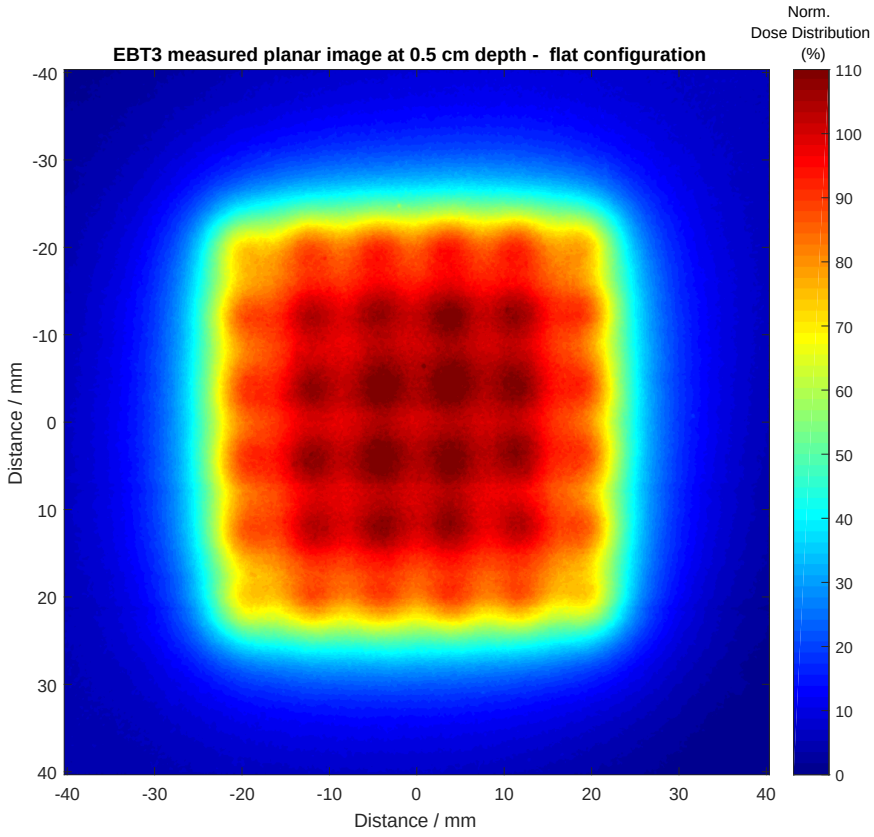

Figure 5.24: The measured dose distribution of a CivaSheet source in the flat configuration at 0.5 cm depth. The dose distribution has been normalized to the central ROI value.

source curve towards the hot side of the device, hence leading to increased dose at the edges at shallow depths. Figure 5.26 presents the results of the measured dose distribution for the convex configuration at 0.5 cm depth. The measured dose distribution fall-off is steeper in this configuration due to decreased dose contribution of the peripheral sources. Hot spots corresponding to the central CivaDot locations are observed.

The 2D-measured dose distribution at each depth was compared to the corresponding Monte Carlo predicted dose distribution for all three configurations. Table 5.3 presents the results of the PDD measured using the EBT3 film stack setup compared to Monte Carlo calculated PDDs. The results were normalized to the 0.5 cm depth on the hot side of the

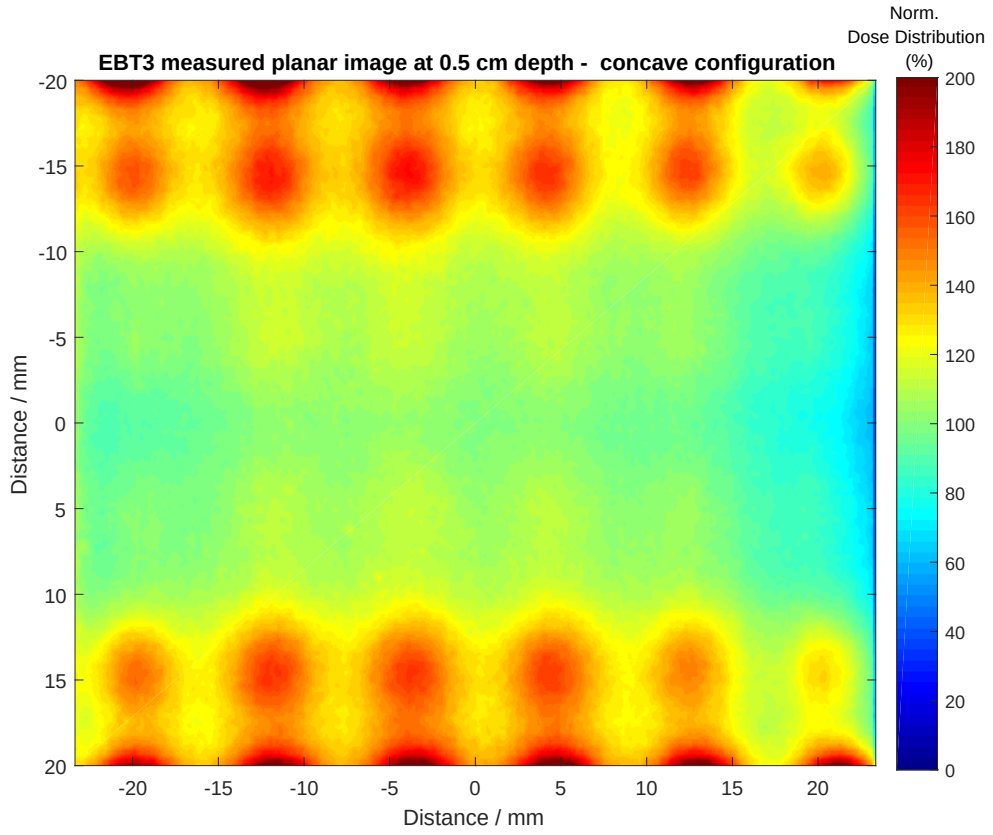

Figure 5.25: The measured dose distribution of a CivaSheet source in the concave configuration at 0.5 cm depth. The dose distribution has been normalized to the central ROI value.

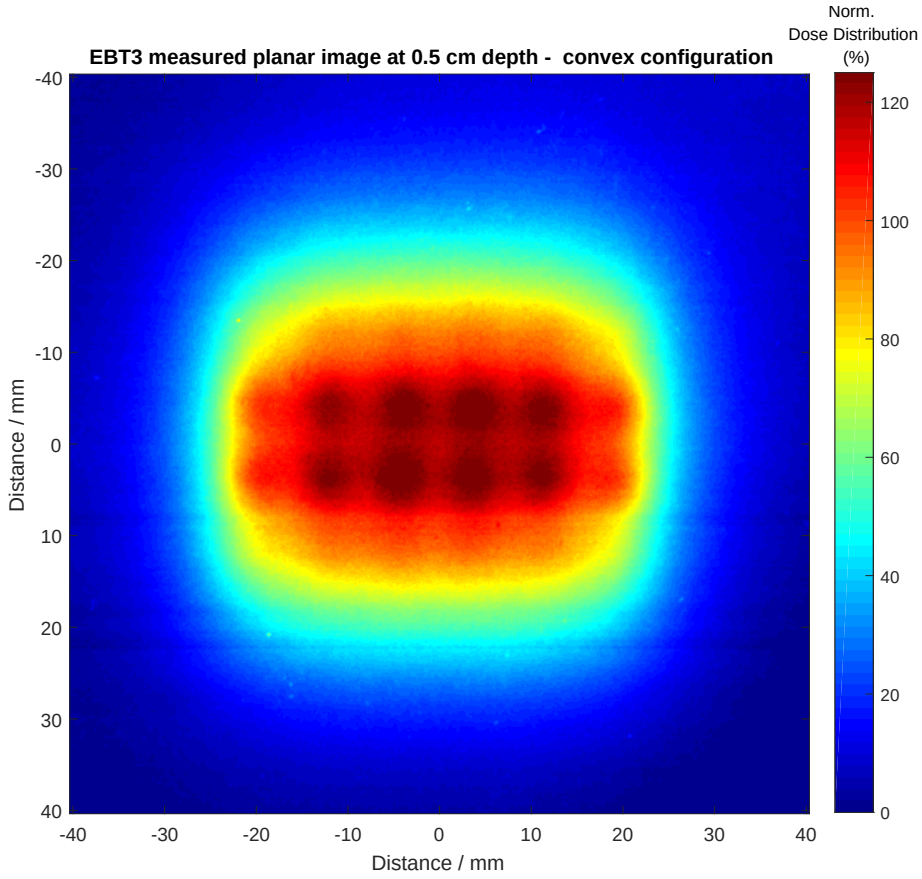

Figure 5.26: The measured dose distribution of a CivaSheet source in the convex configuration at 0.5 cm depth. The dose distribution has been normalized to the central ROI value.

CivaSheet. All measured PDD values are within 4.1% of the Monte Carlo predicted PDD values, with most values within 2.0%. Table 5.4 presents the results of the comparison between the measured and the MC calculated PDDs for the concave source configuration. The measured PDD value was within 3.0% of the MC calculated PDD value for all depths, with most values within 1.5%. The result of the convex configuration PDD distribution comparison is presented in Table 5.5. The measured PDD values for all depths agreed to within 1.2% of the MC calculated PDD values for this configuration. Similar results were observed when comparing the measured PDDs with the PDDs calculated using superposition of CivaDot MC dose distributions at all depths for the three configurations. The agreement between the measured PDD and the CivaDot MC superposition calculated PDD was within 4.0% for the flat configuration, 2.8% for the concave configuration and 1.6% for the convex configuration for all depths.

After the CivaSheet dose distribution measurements were performed, individual source elements (CivaDots) were cropped from the CivaSheet array. The CivaDot sources were measured using a NIST-traceable Standard Imaging HDR1000 Plus well-type ionization chamber. Figure 5.27 presents the distribution of the individual CivaDot source strength normalized to the batch average. The source strength of most of the CivaDots were within $\pm 3\%$ of the batch average, a few sources had differences up to 6.5%. All Monte Carlo simulations performed for this investigation were scaled according to the results of the well chamber measurements.

Table 5.3: Comparison of the average percent depth dose measured using EBT3 film stack and calculated using CivaSheet MC simulations for the flat source configuration. The PDDs were calculated on the source central axis (valley) and normalized to the respective 0.5 cm value.

r (cm)	EBT3 measured %	CivaSheet MC calculated %	Measured and CS MC difference %	CivaDot MC superposition %	Measured and CivaDot MC difference %
0.3	128.8%	128.6%	0.2%	128.8%	0.0%
0.4	114.7%	114.2%	0.5%	114.1%	0.6%
0.5	100.0%	100.0%	-	100.0%	-
0.6	88.2%	87.0%	1.2%	87.0%	1.2%
0.8	69.8%	65.7%	4.1%	65.8%	4.0%
1.0	52.5%	50.2%	2.3%	50.2%	2.3%
2.0	14.5%	14.8%	-0.3%	14.8%	-0.3%
3.0	6.1%	5.0%	1.1%	5.0%	1.1%
4.0	2.3%	1.8%	0.5%	1.8%	0.5%
5.0	1.7%	0.7%	1.0%	0.7%	1.0%
-0.5(cold)	7.1%	4.3%	2.8%	5.1%	2.0%
-1.5(cold)	2.5%	1.9%	0.5%	1.9%	0.6%

Table 5.4: Comparison of the average percent depth dose measured using EBT3 film stack and calculated using CivaSheet MC simulations for the concave source configuration. The PDDs were calculated on the source central axis (valley) and normalized to the respective 0.5 cm value.

r (cm)	EBT3 measured %	CivaSheet MC calculated %	Measured and CS MC difference %	CivaDot MC superposition %	Measured and CivaDot MC difference %
0.3	129.1%	126.4%	2.7%	126.3%	2.8%
0.4	114.3%	113.3%	0.9%	113.9%	0.4%
0.5	100.0%	100.0%	-	100.0%	-
0.6	89.1%	87.7%	1.4%	88.2%	0.9%
0.8	66.3%	67.5%	-1.2%	67.6%	-1.3%
1.0	54.0%	52.5%	1.5%	52.7%	1.3%
2.0	16.8%	16.5%	0.2%	16.6%	0.2%
3.0	6.3%	5.7%	0.6%	5.6%	0.7%
4.0	3.0%	2.1%	0.9%	2.1%	0.9%
5.0	2.1%	0.8%	1.4%	0.8%	1.3%
-0.5(cold)	14.3%	11.4%	3.0%	11.5%	2.8%
-1.5(cold)	2.3%	1.8%	0.5%	1.8%	0.5%

Table 5.5: Comparison of the average percent depth dose measured using EBT3 film stack and calculated using CivaSheet MC simulations for the convex source configuration. The PDDs were calculated on the source central axis (valley) and normalized to the respective 0.5 cm value.

r (cm)	EBT3 measured %	CivaSheet MC calculated %	Measured and CS MC difference %	CivaDot MC superposition %	Measured and CivaDot MC difference %
0.4	114.1%	114.1%	0.0%	113.3%	0.8%
0.5	100.0%	100.0%	-	100.0%	-
0.6	87.4%	86.4%	0.9%	86.2%	1.2%
0.8	64.3%	64.6%	-0.3%	64.0%	0.3%
0.9	54.8%	56.0%	-1.1%	55.8%	-1.0%
1.0	49.9%	48.8%	1.0%	48.3%	1.6%
2.0	14.2%	13.9%	0.3%	13.8%	0.4%
3.0	4.6%	4.6%	0.1%	4.5%	0.1%
4.0	1.8%	1.6%	0.2%	1.6%	0.2%
5.0	1.6%	0.6%	1.0%	0.6%	1.0%
-0.5(cold)	8.8%	8.3%	0.5%	8.5%	0.3%
-1.0(cold)	4.6%	4.1%	0.5%	3.3%	1.3%

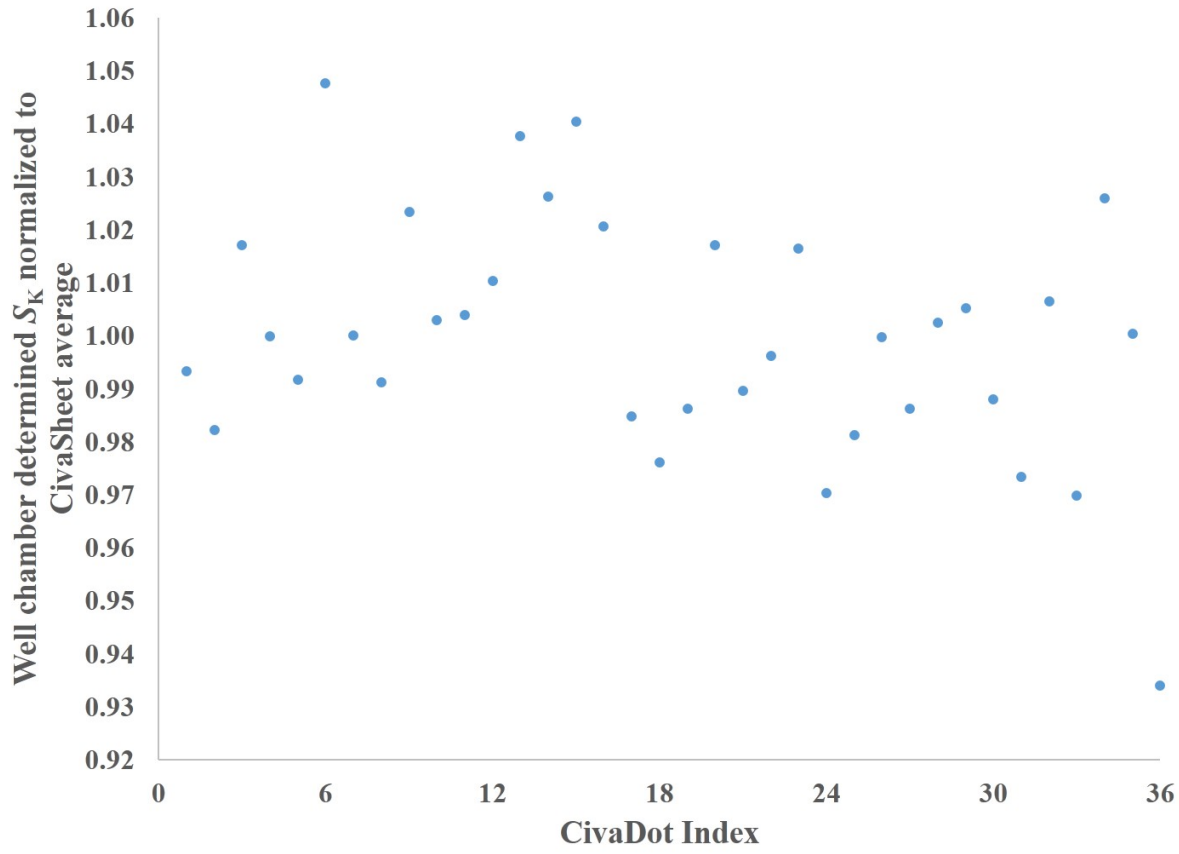

Figure 5.27: Results of the variation of the air-kerma strength determined for a CivaDot of the CivaSheet array using the HDR1000 Plus well chamber. The values for a given source were normalized to the batch average air-kerma strength value. The individual CivaDots are indexed 1 through 36.

5.5 Conclusions

Dose distribution measurements of the CivaSheet performed using EBT3 films in a PMMA phantom and a virtual water phantom demonstrated good overall agreement with Monte Carlo predicted dose distributions. CivaSheet dose distribution was investigated in three configurations including two curved configurations. The impact of the curvature of the source on the dose distribution was investigated and should be taken into account when using the CivaSheet for a treatment.

Chapter 6

Conclusions and Future Work

6.1 Conclusions

6.1.1 CivaDot source strength determination

Primary air-kerma strength measurements of the CivaDot performed using the UW VAFAC instrument indicated that air-kerma strength is a good source strength metric for this source. To determine air-kerma strength for a novel source such as the CivaDot, additional investigations were performed. Appropriate determination of the energy spectrum of a source is necessary for the calculation of the free-air chamber measurement correction factors. The CivaDot energy spectrum was measured, and calculated using Monte Carlo methods. The presence of gold shield x-ray fluorescence was observed in both the measured and calculated energy spectrum, the impact of which was evaluated throughout the body of this work. An inter-comparison of the CivaDot primary air-kerma strength measurements using the UW VAFAC and the national primary standard for low-energy photon-emitting LDR sources, the NIST WAFAC resulted in good agreement between the two instruments. The results illustrated the good repeatability of the UW VAFAC and NIST WAFAC measurements and comparable reproducibility of the UW VAFAC measurement to the U.S. national standard.

The result was a good validation of the methods and measurement protocols used in this work to determine the CivaDot source strength, and assisted in the establishment of the primary source strength standard for the CivaDot at NIST. The transfer of the CivaDot primary air-kerma strength to a well-type ionization chamber was found to be feasible for dissemination to clinical users through an AAPM accredited ADCL calibration procedure.

6.1.2 CivaDot dose distribution

The dosimetric characterization of the CivaDot source was performed using measurements of the dose distributions of multiple sources with thermoluminescent dosimeters and EBT3 film, and subsequent comparison to Monte Carlo predicted dose distributions. Good agreement was observed between the dose distributions measured using the two dosimeters and the calculated CivaDot dose distribution. EBT3 film (expiration dates — 2015, 2016, 2017) was demonstrated as a viable dosimeter for the dosimetric characterization of a low-energy photon-emitting brachytherapy source. This work explored the use of an adapted TG-43 formalism for the CivaDot source and calculated the relevant analogous dosimetric parameters. The dosimetric characterization of the CivaDot as performed in this work led to a viable dosimetric framework for the CivaSheet array.

6.1.3 CivaSheet dose distribution

The feasibility of an element-based dosimetric characterization of the CivaSheet array was assessed successfully. CivaSheet dose distribution was determined using an EBT3 film stack measurement setup and CivaSheet Monte Carlo simulations, and compared to superposition of individual CivaDot dose distributions. Good agreement was observed between the measured and the predicted dose distributions. The impact of the curvature of the CivaSheet was assessed using a curved phantom measurement and calculations. The results observed

in the comparison of the three configurations necessitate that appropriate care should be taken when the CivaSheet is used clinically in a curved orientation.

6.2 Future work

6.2.1 Customized CivaDot loading

As the clinical implementation of the CivaSheet device matures further, there might arise a need to customize CivaDot loading to achieve extremely conformal dose distributions. Given that the CivaSheet is an array of relatively small sized sources, it would be interesting to explore the feasibility of customized non-uniform source strength loading of individual CivaDot sources. Such an investigation would require further characterization of the CivaDot source as well as implementation of plan optimization techniques. Although the manufacturer is currently not equipped for this process, this could be an option in the future.

6.2.2 A study of different CivaSheet curvatures

Patient implants with different curvatures or non-cylindrical curvatures of the source might be required as the CivaSheet device is used more frequently in the clinic. An investigation into different sets of radii of curvature (cylindrical) or curvature shapes for a CivaSheet implant could thus be performed, to evaluate the changes in the dose distribution of the device for clinical use.

6.3 Closing remarks

This work focused on outlining the methods to characterize a novel brachytherapy source. It aimed to improve and adapt current brachytherapy dosimetry methods to help facilitate the clinical implementation of a directional planar LDR brachytherapy source array. Rigorous emphasis was placed on assuring quality dose measurement and computational data, which

should be necessary prior to the clinical use of any therapeutic device. Future advancements in this field could bring forth the advent of dose painting using brachytherapy devices with highly conformal dose distributions.

Bibliography

F. Abboud, M. Hollows, P. Scalliet, and S. Vynckier. Experimental and theoretical dosimetry of a new polymer encapsulated iodine-125 source - *SmartSeed*: dosimetric impact of fluorescence x rays. *Med. Phys.*, 37(5):2054–2062, 2010.

M. Aima, J.L. Reed, L.A. DeWerd, and W.S. Culberson. Air-kerma strength determination of a new directional ^{103}Pd source. *Med. Phys.*, 42(12):7144–7152, 2015.

M. J. Berger, J. H. Hubbell, S. M. Seltzer, J. Chang, J. S. Coursey, R. Sukumar, and D. S. Zucker. XCOM: Photon cross section database (Version 1.3). [Online] Available: http://physics.nist.gov/xcom (last accessed 16 Nov 2010), National Institute of Standards and Technology, Gaithersburg, MD, 2005.

S. Bernard and S. Vynckier. Dosimetric study of a new polymer encapsulated palladium-103 seed. *Phys. Med. Biol.*, 50(7):1493–1504, 2005.

Valeria Casanova Borca, Massimo Pasquino, Giuliana Russo, Pierangelo Grosso, Domenico Cante, Piera Sciacero, Giuseppe Girelli, Maria Rosa La Porta, and Santi Tofani. Dosimetric characterization and use of gafchromic ebt3 film for imrt dose verification. *Journal of Applied Clinical Medical Physics*, 14(2):158–171, 2013. ISSN 1526-9914.

M. Boutillon and A. M. Perroche-Roux. Re-evaluation of the W value for electrons in dry air. *Phys. Med. Biol.*, 32:213, 1987.

National Nuclear Data Center Brookhaven National Laboratory. Nuclear structure & decay data, technical report. www.nndc.bnl.gov/nudat2/, last accessed on 09/07/2014.

W. M. Butler, W. S. Bice, Jr., L. A. DeWerd, J. M. Hevezi, M. S. Huq, G. S. Ibbott, J. R. Palta, M. J. Rivard, J. P. Seuntjens, and B. R. Thomadsen. Third-party brachytherapy source calibrations and physicist responsibilities: Report of the AAPM Low Energy Brachytherapy Source Calibration Working Group. *Med. Phys.*, 35(9):3860–3865, 2008.

V. Chaswal, B. R. Thomadsen, and D. L. Henderson. Development of an adjoint sensitivity field-based treatment-planning technique for the use of newly designed directional LDR sources in brachytherapy. *Phys. Med. Biol.*, 57(4):963–982, 2012.

S.T. Chiu-Tsao, J.J. Napoli, S.D. Davis, J. Hanley, and M.J. Rivard. Dosimetry for ^{131}Cs and ^{125}I seeds in solid water phantom using radiochromic EBT film. *Appl Rad Isot*, 92: 102 – 114, 2014. ISSN 0969-8043.

Gil'ad N. Cohen, Karen Episcopia, Seng-Boh Lim, Thomas J. LoSasso, Mark J. Rivard, Amandeep S. Taggar, Neil K. Taunk, Abraham J. Wu, and Antonio L. Damato. Intraoperative implantation of a mesh of directional palladium sources (civasheet): Dosimetry verification, clinical commissioning, dose specification, and preliminary experience. *Brachytherapy*, 16(6):1257 – 1264, 2017. ISSN 1538-4721.

A. Colonias, J. Betler, M. Trombetta, G. Bigdeli, O. Gayou, R. Keenan, E. D. Werts, and D. S. Parda. Mature Follow-Up For High-Risk Stage I Non-Small-Cell Lung Carcinoma Treated with Sublobar Resection and Intraoperative Iodine-125 Brachytherapy. *Int. J. Radiat. Oncol. Biol. Phys.*, 79(1):105–109, 2011.

W.S. Culberson, L.A. DeWerd, D.R. Anderson, and J.A. Micka. Large-volume ionization chamber with variable apertures for air-kerma measurements of low-energy radiation sources. *Rev. Sci. Instrum.*, 77:015105, 2006.

L.A. DeWerd, J.A. Micka, S.M. Holmes, and T.D. Bohm. Calibration of multiple LDR brachytherapy sources. *Med. Phys.*, 33(10):3804–3813, 2006.

J.T. Goorley. Initial mcnp6 release overview - mcnp6 version 1.0. http://permalink.lanl.gov/object/tr?what=info:lanl-repo/lareport/LA-UR-13-22934, last accessed 01/01/2015.

S. L. Griffin, L. A. DeWerd, J. A. Micka, and T. D. Bohm. The effect of ambient pressure on well chamber response: Experimental results with empirical correction factors. *Med. Phys.*, 32(3):700–709, 2005.

Cliff Hammer, Benjamin Rosen, Jessica Fagerstrom, Wesley Culberson, and Larry DeWerd. Experimental investigation of gafchromic ebt3 intrinsic energy dependence with kilovoltage x rays, ^{137}Cs, and ^{60}Co. *Medical Physics*, 45(1):448–459.

H.Morrison, G.Menon, and R.S. Sloboda. Radiochromic film calibration for low-energy seed brachytherapy dose measurement. *Med. Phys.*, 41(7):072101, 2014.

M. Johnson, A. Colonias, D. Parda, M. Trombetta, O. Gayou, B. Reitz, and M. Miften. Dosimetric and technical aspects of intraoperative I-125 brachytherapy for stage I non-small cell lung cancer. *Phys. Med. Biol.*, 52(5):1237–1245, 2007.

L. Y. Lin, R. R. Patel, B. R. Thomadsen, and D. L. Henderson. The use of directional interstitial sources to improve dosimetry in breast brachytherapy. *Med. Phys.*, 35(1): 240–247, 2008.

A. S. Meigooni, H. Zhang, J. R. Clark, V. Rachabatthula, and R. A. Koona. Dosimetric characteristics of the new RadioCoil$^{\text{TM}}$ ^{103}Pd wire line source for use in permanent brachytherapy implants. *Med. Phys.*, 31(11):3095–3105, 2004.

M. K. Murphy, R. K. Piper, L. R. Greenwood, M. G. Mitch, P. J. Lamperti, S. M. Seltzer, M. J. Bales, and M. H. Phillips. Evaluation of the new Cesium-131 seed for use in low-energy x-ray brachytherapy. *Med. Phys.*, 31(6):1529–1538, 2004.

R. Nath, L. L. Anderson, G. Luxton, K. A. Weaver, J. F. Williamson, and A. S. Megooni. Dosimetry of interstitial brachytherapy sources: Recommendations of the AAPM Radiation Therapy Committee Task Group No. 43. *Med. Phys.*, 22(2):209–234, 1995.

R. Nath, L.L. Anderson, J.A. Meli, A.J. Olch, J.A. Stitt, and J.F. Williamson. Code of practice for brachytherapy physics: Report of the AAPM Radiation Therapy Committee Task Group No. 56. *Med. Phys.*, 24(10):1557–1598, 1997.

A. A. Nunn, S. D. Davis, J. A. Micka, and L. A. DeWerd. LiF:Mg,Ti TLD response as a function of photon energy for moderately filtered x-ray spectra in the range of 20 to 250 kVp relative to ^{60}Co. *Med. Phys.*, 35(5):1859–1869, 2008.

A.B. Paxton, W.S. Culberson, L.A. DeWerd, and J.A. Micka. Primary calibration of coiled ^{103}Pd brachytherapy sources. *Med. Phys.*, 35(1):32–38, 2008.

J. L. Reed, B. E. Rasmussen, S. D. Davis, J. A. Micka, W. S. Culberson, and L. A. DeWerd. Determination of the intrinsic energy dependence of LiF:Mg,Ti thermoluminescent dosimeters for ^{125}I and ^{103}Pd brachytherapy sources relative to ^{60}Co. *Med. Phys.*, 41(12): 122103, 2014a.

J. L. Reed, M. J. Rivard, J. A. Micka, W. S. Culberson, and L. A. DeWerd. Experimental and Monte Carlo dosimetric characterization of a 1 cm ^{103}Pd brachytherapy source. *Brachytherapy*, 13(6):657–67, 2014b.

M. J. Rivard, B. M. Coursey, L. A. DeWerd, W. F. Hanson, M. S. Huq, G. S. Ibbott, M. G. Mitch, R. Nath, and J. F. Williamson. Update of AAPM Task Group No. 43 report: A revised AAPM protocol for brachytherapy dose calculations. *Med. Phys.*, 31(3):633–674, 2004.

M. J. Rivard, W.M. Butler, L.A. DeWerd, M. S.Huq, G.S. Ibbott, A.S. Meigooni, C.S. Melhus, M.G. Mitch, R.Nath, and J.F. Williamson. Supplement to the 2004 update of the AAPM Task Group No. 43 Report. *Med. Phys.*, 34 (6):2187–2205, 2007.

Mark J. Rivard. A directional 103pd brachytherapy device: Dosimetric characterization and practical aspects for clinical use. *Brachytherapy*, 16(2):421 – 432, 2017. ISSN 1538-4721.

R. Santos, A. Colonias, D. Parda, M. Trombetta, R. H. Maley, R. Macherey, S. Bartley, T. Santucci, R. J. Keenan, and R. J. Landreneau. Comparison between sublobar resection and ^{125}I brachytherapy after sublobar resection in high-risk patients with Stage I non-small cell lung cancer. *Surgery*, 134(4):691–697, 2003.

S. M. Seltzer, P. J. Lamperti, R. Loevinger, M. G. Mitch, J. T. Weaver, and B. M. Coursey. New national air-kerma-strength standards for ^{125}I and ^{103}Pd brachytherapy seeds. *J. Res. Natl. Inst. Stand. Technol.*, 108:337–357, 2003.

B. N. Taylor and C. E. Kuyatt. Guidelines for evaluating and expressing the uncertainty of NIST measurement results. Technical Note 1297, National Institute of Standards and Technology, 1994.

G. Voynov, D. E. Heron, C. J. Lin, S. Burton, A. Chen, A. Quinn, R. Santos, A. Solonias, and R. J. Landreneau. Intraoperative ^{125}I Vicryl mesh brachytherapy after sublobar resection for high-risk stage I nonsmall cell lung cancer. *Brachytherapy*, 4(4):278–285, 2005.

Z. Wang and N.E. Hertel. Determination of dosimetric characteristics of $OptiSeed^{TM}$ a plastic brachytherapy ^{103}Pd source. *Appl. Radiat. Isot.*, 63(3):311–321, 2005.

Y. Yang and M. J. Rivard. Evaluation of brachytherapy lung implant dose distributions from photon-emitting sources due to tissue heterogeneities. *Med. Phys.*, 38(11):5857–62, 2011.